Peter Ranacher, BSc

Magnetization behavior of submicrocrystalline nickel prepared by extreme plastic deformation

MASTER THESIS

For obtaining the academic degree
Diplom-Ingenieur

Master Program of
Technical Physics

Graz University of Technology

Supervisor:

Univ.-Prof. Dipl.-Phys. Dr.rer.nat. Roland Würschum

Co-supervisor:

Dipl.-Ing. Dr.techn. Stefan Topolovec

Institute of Materials Physics

Graz, November 2016

Statutory Declaration

I declare that I have authored this thesis independently, that I have not used other than the declared sources/resources, and that I have explicitly marked all material which has been quoted either literally or by content from the used sources.

Graz, _____ _____

Date Signature

Eidesstattliche Erklärung[1]

Ich erkläre an Eides statt, dass ich die vorliegende Arbeit selbstständig verfasst, andere als die angegebenen Quellen/Hilfsmittel nicht benutzt, und die den benutzten Quellen wörtlich und inhaltlich entnommenen Stellen als solche kenntlich gemacht habe.

Graz, am _____ _____

Datum Unterschrift

[1] Beschluss der Curricula-Kommission für Bachelor-, Master- und Diplomstudien vom 10.11.2008; Genehmigung des Senates am 1.12.2008

Abstract

Magnetization behavior of submicrocrystalline nickel prepared by extreme plastic deformation

This master thesis deals with studies of the magnetic hysteresis of severely deformed nickel samples in a SQUID-magnetometer with the aim to obtain information about the microstructure and the crystal defects of the samples. The nickel samples were deformed using HPT (high pressure torsion) and ECAP (equal channel angular pressing).

HPT- and ECAP-deformed samples exhibit enhanced coercivities. Upon recrystallization the coercivity decreases, i.e., the samples become magnetically softer. By analyzing the virgin curves three magnetic field areas are identified in which different effects dominate. In the low-field area Bloch-wall movement dominates. For the HPT samples the initial permeability increases upon recrystallization. This is viewed as additional evidence that the samples get magnetically softer upon recrystallization. The medium-field area is governed by the rotation of domains. Analyses of the M-H-behavior in this range by two different methods show that the deformed samples approach saturation more sluggishly than the recrystallized samples and the reference samples. The approach to saturation magnetization at high fields is dominated by the alignment of magnetic moments adjacent to defects. For this area a model of Kronmüller was used which describes the saturation behavior by a power series, where the respective power terms are assigned to different crystal defects. According to this model, non-magnetic spherical defects dominant. It is assumed that these defects are nanovoids in the sample.

Kurzfassung

Magnetisierungsverhalten von submikrokristallinen Nickel hergestellt durch extreme plastische Verformung

Diese Masterarbeit befasst sich mit Untersuchungen der magnetischen Hysterese von stark verformten Nickelproben in einem SQUID-Magnetometer mit der Zielsetzung, daraus Informationen über die Mikrostruktur und Kristalldefekte zu gewinnen. Die Nickelproben wurden mittels der Verfahren HPT (high pressure torsion) und ECAP (equal channel angular pressing) verformt.

Für die HPT- und ECAP-verformten Proben wurden erhöhte Koerzitivfeldstärken beobachtet. Durch Rekristallisation verringerte sich die Koerzitivfeldstärke, d.h., die Proben wurden magnetisch weicher. Durch Analyse der Neukurve konnten drei magnetische Feldbereiche identifiziert werden, in welchen unterschiedliche Effekte dominieren. Im Niederfeldbereich dominiert die Bewegung von Bloch-Wänden. Die HPT Proben zeigten eine erhöhte Anfangspermeabilität nach der Rekristallisation. Dies wird als weiterer Beweis für das magnetische Aufweichen der Proben nach der Rekristallisation angesehen. Im Mittelfeldbereich rotieren die Weissschen Bezirke in Richtung des angelegten Magnetfeldes. Die Analysen des M-H-Verhaltens nach zwei unterschiedlichen Methoden zeigen, dass in verformten Proben die Annäherung an die Sättigungsmagnetisierung schwerfälliger verläuft als in rekristallisierten Proben und in Referenzproben. Das Einmündungsverhalten in die Sättigung bei hohen Feldern wird durch die Ausrichtung magnetischer Momente bestimmt, die sich in der Umgebung von Defekten befinden. Für diesen Bereich wurde ein Modell von Kronmüller angewandt, welches die Annäherung an die Sättigungsmagnetisierung mittels Potenzreihenentwicklung beschreibt und die jeweiligen Potenzen unterschiedlichen Kristalldefekten zuordnet. Es stellte sich dabei heraus, dass nicht-magnetische sphärische Kristalldefekte dominieren. Es wird davon ausgegangen, dass es sich dabei um nanoskalige Poren in der Probe handelt.

Contents

1. Introduction

The properties of metals can be strongly influenced by mechanical processing. Ultra-fine grained (UFG) metals can be produced by means of extreme deformation. The most importent of such routes are High Pressure Torsion (HPT) and Equal-Channel Angular Pressing (ECAP). The grain size of UFG materials is in the range of 100-1000 nm. As deformation induces grain boundaries, which act as barriers to dislocation motions, the materials get harder to deform.

The Institute of Materials Physics at the TU Graz has conducted several projects to measure the changes that occur during temperature annealing of UFG metals, particularly of Ni. Oberdorfer [1] noticed that the measured differential curve of the length change goes through three different temperature annealing stages. At each stage the length of the severely deformed sample changes due to different effects.
In the first area ($<160\,^{\circ}$C) a slow but continuous length contraction can be observed. The lattice vacancies annealed out via diffusion to grain boundaries (GB). Additionally, GB relaxation occurs in this area. According to scanning electron microscopy no grain growth occurred in this regime.
In the second area (160 °C-220 °C) recrystallization occurs upon which the relaxed GB anneal out, reducing the free volume in the material.
The processes in the third area ($>220\,^{\circ}$C) are not fully understood yet. It is speculated that further grain growth and annealing of voids occurs in this stage. [1]

The goal of this thesis is to obtain more information about the microstructure and the defects by means of magnetic measurements. This thesis uses nickel samples, which are ferromagnetic at room temperature. Due to magnetoelastic coupling, the magnetization is susceptible to defects since the magnetic moments adjacent or within the defect cores are restricted with respect to alignment in an external magnetic field. Based on a theory of W. Brown, H. Kronmüller developed a model for the approach

to ferromagnetic saturation using a series of powers H^{-x}. The dominant power gives information about the dominant defect type in the ferromagnetic material.[2] In the present work the measurements were not restricted to the approach to ferromagnetic saturation, but the entire H-field range of magnetization was studied including initial permeability and coercivity.

2. Basics

In the following chapters a short introduction into the physics necessary to understand this master thesis is given. In section 2.1 the different deformation processes used to prepare the nickel samples are explained. In section 2.2 an introduction into ferromagnetism is given. Additionally in this section the theory behind the law of approach to saturation will be outlined.

2.1. Deformation processes

For the experiments several samples were cut out of deformed nickel forms. Compared to undeformed nickel samples, these samples contain additional deformation-induced defects owing to the treatment. Three different methods of deformation were applied: High Pressure Torsion (HPT), Equal-Channel Angular Pressing (ECAP), which are both severe deformation methods, and Cold Rolling (CR).

2.1.1. High Pressure Torsion (HPT)

In this process nickel was subjected to a compressive force and concurrent torsional straining. This metal forming process provides an opportunity for achieving exceptional grain refinement into the range of hundred nanometers and exceptionally high strength. [3] The produced grain size is usually smaller than the grain sizes produced by ECAP but the size of the disc is limited. [4] In figure 2.1(a) a sketch of the procedure is shown.

2.1.2. Equal-Channel Angular Pressing (ECAP)

This process is also used for the fabrication of ultra-fine grained metals and alloys. The defining factors of ECAP processing are the strain imposed, the slip systems and shearing patterns, as well as the die geometry (angle) and pressing regimes. All these play an essential role in microstructural refinement during the pressing operation. [5] In figure 2.1(b) a rough draft of the procedure is pictured.

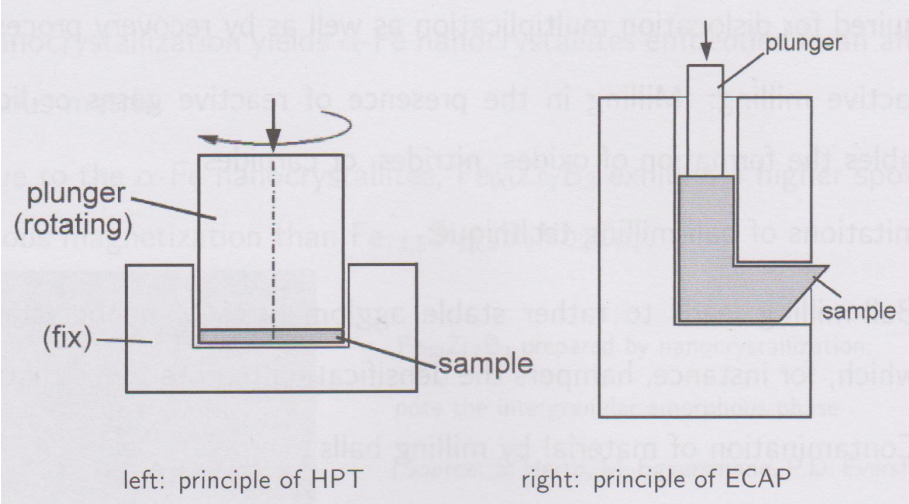

Figure 2.1.: left: High-pressure torsion: a sample is held between the plunger and the fix part and strained in torsion under applied pressure by the plunger. right: Equal channel angular pressing: a work-piece is repeatedly pressed through a special die by the plunger. [6]

2.1.3. Cold Rolling (CR)

Rolling is a conventional metal forming process in which the metal is passed through rolls to reduce the thickness and to make the thickness uniform. Depending on the temperature of the metal the process is either hot rolling (above recrystallization temperature) or cold rolling (below recrystallization temperature).

2.2. Ferromagnetism

Out of all pure transition metals only iron, nickel and cobalt are ferromagnetic at room temperature (20 °C). In our case the samples are of highly pure nickel. Ferromagnetism

is characterized by a high magnetization, which usually exhibits a hysteresis curve as seen in figure 2.2.

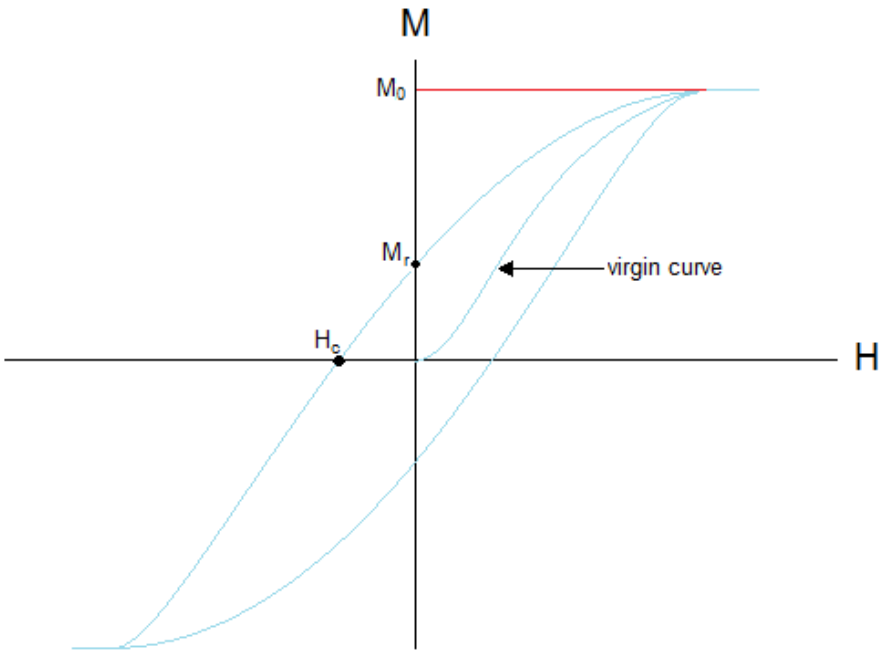

Figure 2.2.: Magnetization as a function of field. M: magnetization, H: magnetic field, M_0: saturation magnetization, M_{rem}: remanent magnetization, H_c: coercivity

The key feature is, that the curve is nonlinear and not reversible, showing the magnetic hysteresis seen in figure 2.2. The virgin curve is observed when the magnetic material gets magnetized for the first time (from being in a nonmagnetic state). The magnetization gradually reaches a maximum value called the saturation magnetization M_s. After reducing the field H to zero, a remanent magnetization M_{rem} remains. If it is high, the material is a hard magnetic material and can be used for permanent magnets, like Al-Ni-Co, Sm-Co or Nd-Fe-B [7]. On the other hand, materials with small remanent magnetization are called soft ferromagnets, like nickel. In order to get rid of the net magnetization of a ferromagnet, a coercive field H_C in the opposite direction is required. After reaching the negative -M_0, which should be the same absolute value as the positive one, the field can be increased again and should have the same absolute values for M_r and H_C as in the positive half. After reaching the positive M_0 again the characteristic hysteresis is completed as seen in the path taken in figure 2.2. [8]

Ferromagnetic materials are only ferromagnetic below the Curie Temperature T_C. Above this temperature they become paramagnetic and exhibit a Curie-Weiss behavior. For our experiments the annealing temperature for nickel is higher than the Curie

temperature ($T_C = 354°C$). Our measurements with the SQUID measured at room temperature are far below T_C. As seen in figure 2.3 the saturation magnetization is a function of the temperature, however we measure at constant temperature.

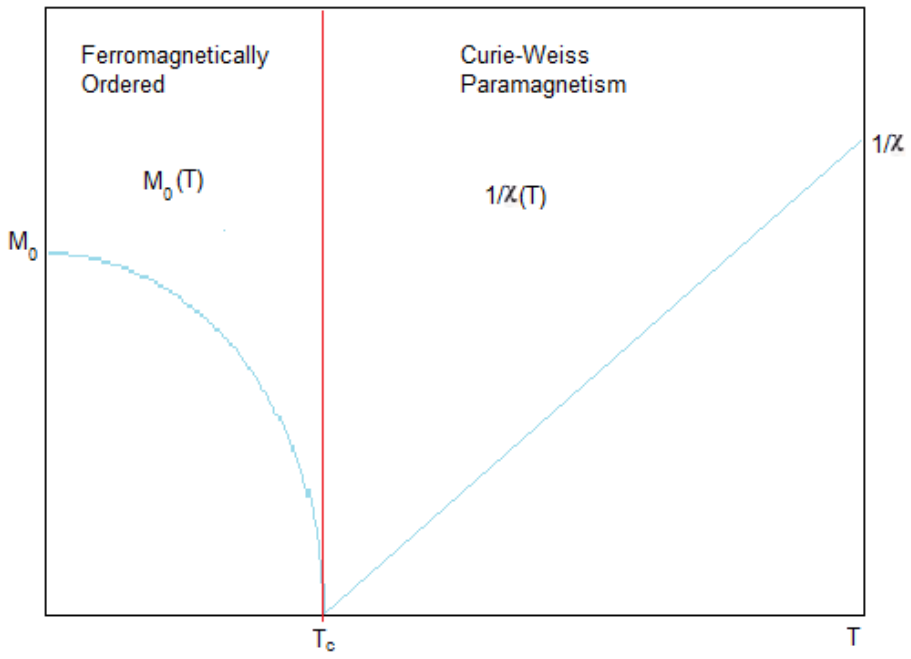

Figure 2.3.: Saturation magnetization as a function of temperature. M_0: saturation magnetization, T_c: Curie Temperature, χ: magnetic susceptibility

2.2.1. Law of approach to ferromagnetic saturation

W.F. Browns aims to find an explanation to describe the magnetization behavior at high magnetic fields using power law. Kronmüller [2] links the power terms with different types of defects in the sample on the approach to ferromagnetic saturation. These defects prevent the surrounding magnetic moments from rotating, due to pinning of spin orientation, which means that a higher applied magnetic field is necessary to reach saturation magnetization. The saturation magnetization is reduced by defects associated with powers of H^{-x}. They are stress centers such as point defects, dislocations, grain boundaries and nonmagnetic precipitations. Each of them gives rise to a characteristic field dependence (equation (2.1)).

$$M(H) = M_s - \left(\frac{a_{1/2}}{H^{1/2}} + \frac{a_1}{H} + \frac{a_{3/2}}{H^{3/2}} + \frac{a_2}{H^2} + \frac{a_3}{H^3}\right) + \alpha T\sqrt{H} + \chi_P \cdot \mu_0 H \qquad (2.1)$$

The $a_{n/2}$ coefficients depend on the concentration and type of the defects. M_s is the spontaneous magnetic field, α is a constant and χ_P is the paramagnetic susceptibility.

In figure 2.4(a)-(d) point dislocations, straight dislocations, a dislocation dipole and nonmagnetic spherical precipitations (holes) are shown, respectively.

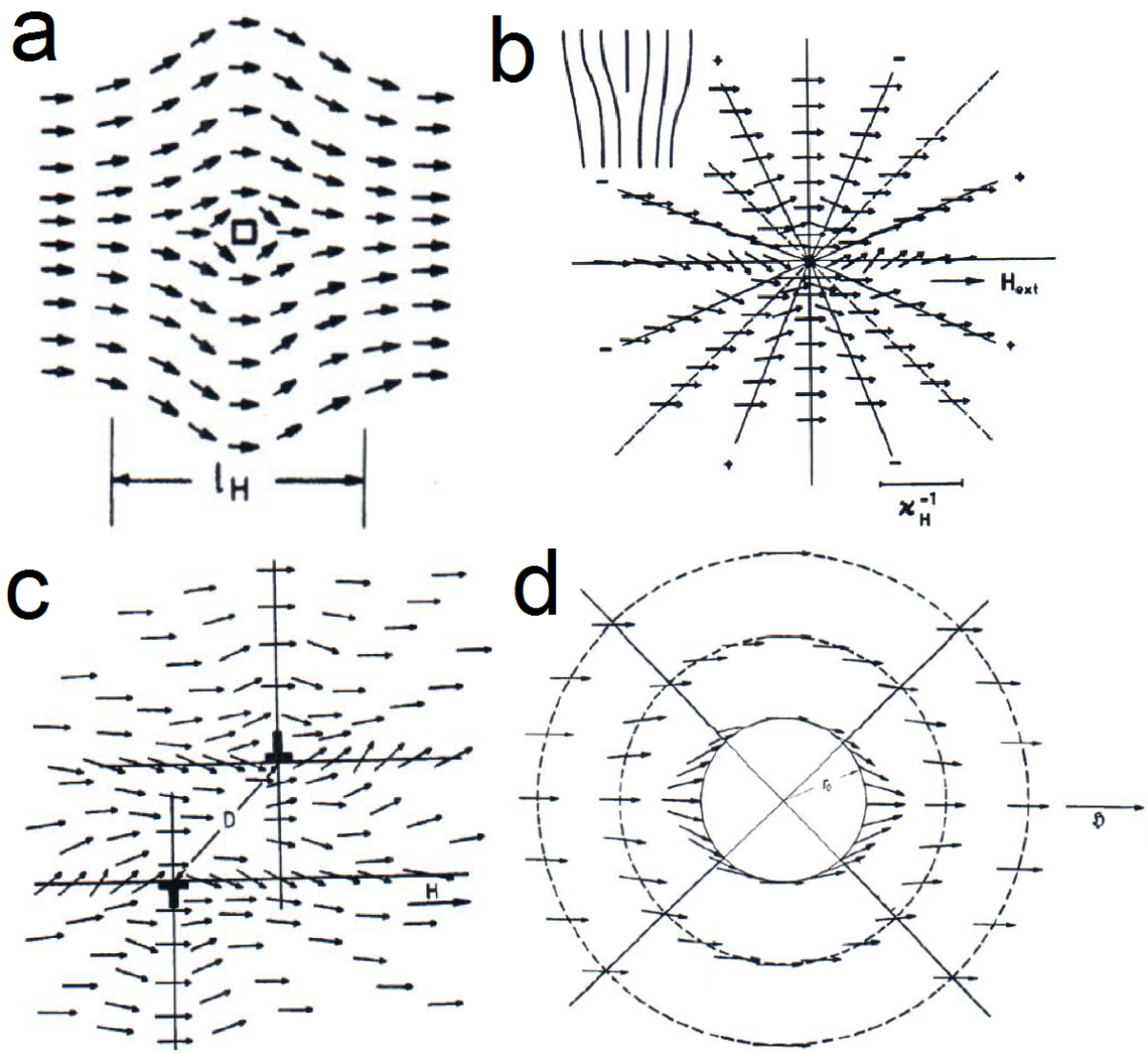

Figure 2.4.: (a) "Spin arrangement around a point-like defect. Integral spin deviation $\propto 1/H^{1/2}$." [2] l_H: exchange lengths of the external field. (b) "Spin arrangement in the stress field of an edge dislocation for $\mu_0 H = 0.1T$ applied parallel to the Burgers vector. The signs $(+)$ and $(-)$ refer to the sign of the shear stress σ_{12}. Integral spin deviation $\propto 1/H^{1/2}$." [2] H_{ext}: external magnetic field, χ_H^{-1}: inverse magnetic susceptibility. (c) "Spin arrangement in the stress field of an edge dislocation dipole. Integral spin deviation $\propto 1/H$." [2] H: external magnetic field, D: distance between the dislocations. (d) Nonmagnetic spherical precipitations of radius r_0. [2] b: magnetic flux density

Depending on their size, the defects are associated with the following power laws of saturation behavior; $\Delta M = M_s - M(H)$ (see figure 2.4) [2]:

Point defects of radius r_0:

$r_0 < l_H, \Delta M = a_{1/2}/H^{1/2}$

$r_0 > l_H, \Delta M = a_2/H^2$

Straight dislocation dipoles of width D:

$D < l_H, \Delta M = a_1/H$

$D > l_H, \Delta M = a_2/H^2$

Circular dislocation dipoles of radius R:

$R < l_H, \Delta M = a_{1/2}/H^{1/2}$

$R > l_H, \Delta M = a_2/H^2$

Individual straight dislocations:

$\Delta M = a_2/H^2$

Nonmagnetic spherical precipitations of radius r_0:

$r_0 < l_H, \Delta M = a_{1/2}/H^{1/2}$

$r_0 > l_H, \Delta M = a_{3/2}/H^{3/2}$

M_s is spontaneous magnetic polarization, $M(H)$ the magnetic polarization dependent of the field, and l_H the exchange length of the external field.

$$l_H = \sqrt{\frac{2A}{M_s H_{ext}}} \tag{2.2}$$

where A is the exchange stiffness constant (an intrinsic magnetic material parameter) and H_{ext} is the external field. For the sake of completeness circular dislocation dipoles are also listed above, however they are unlikely in materials treated by Severe Plastic Deformation (SPD).

The last two terms in equation (2.1) ($\alpha T\sqrt{H} + \chi_P \cdot \mu_0 H$) mainly affect the high field behavior ($>$ 4T). Those terms describe areas where further increase of the applied field only leads to alignment of the misaligned atomic magnets due to thermal fluctuations. As this is similar to the magnetization of a paramagnetic substance, it is named para effect. [9] The a_3/H^3 term is negligible for cubic crystals.

Holger Kisker et al. [10] used a slightly different equation (2.3) for the approach to ferromagnetic saturation. He neglects $H^{-3/2}$ and treats all nonmagnetic agglomerations with $H^{-1/2}$ behavior. Additionally, he has no H^{-3} factor as he only deals with nickel

samples and uses the Holstein-Primakoff-function for the paraeffect. The equation is a combination of terms from [11], [12], [13] and [14].

$$M(T_0, H) = M_s(T_0) - \frac{a_{1/2}}{H^{1/2}} - \frac{a_1}{H} - \frac{a_2}{H^2} + c \cdot T_0 \cdot f_{HP}(M_0, H) \tag{2.3}$$

$$f_{HP} = 3\sqrt{H} + \frac{M_0 + H}{\sqrt{M_0}} \cdot \arcsin\sqrt{\frac{M_0}{M_0 + H}} \tag{2.4}$$

where T_0 the measurement temperature, M_s is the spontaneous magnetization, c is a constant, f_{HP} is the Holstein-Primakoff-function (see equation (2.4)) and M_0 the saturation magnetization. The last term $\Delta M_{para} = c \cdot T_0 \cdot f_{HP}(M_0, H)$ is the para effect. Compared to equation (2.1) the paraeffect has the same field dependence and only the factor f_{HP} is slightly different.

2.2.2. Anisotropy energy

Due to spin–orbit interaction there is a preferred crystal direction for magnetization. When magnetizing in a different direction an additional energy, the anisotropy energy is required. The magnetization behavior, which is based on reorientation, gives information about the anisotropy energy. The anisotropy energy is usually described by the anisotropy constants K_{eff}. Sahar [15] proposes a method to calculate this constant, which is strongly responsible for the curvature of the virgin curve.

The rotation of magnetic domains dominates after Bloch wall movement is finished ($\sim 1000\,\mathrm{Oe}$) until the rotation of domains is completed ($\sim 4000\,\mathrm{Oe}$). For evaluation the following power law equation was used:

$$M(H) = M_s - \left(\frac{a_{1/2}}{H^{1/2}} + \frac{a_1}{H} + \frac{a_{3/2}}{H^{3/2}} + \frac{a_2}{H^2}\right) \tag{2.5}$$

The power terms in the equation were stopped at H^{-2}. The effective anisotropy constant K_{eff} can be calculated with the coefficient a_2.

For our measured nickel samples the crystal structure is face-centered cubic (fcc) and the easiest to magnetize direction is the [111] direction as seen in figure 2.5. [16]

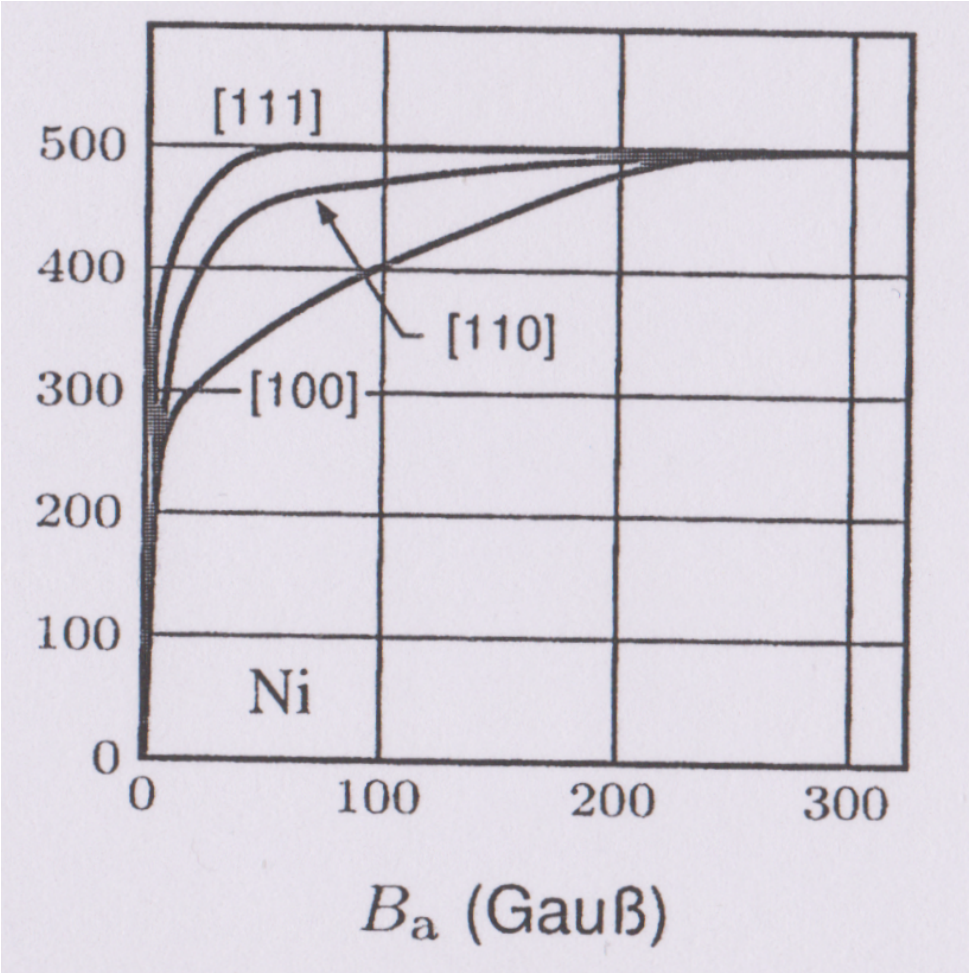

Figure 2.5.: Magnetic hysteresis for single crystal nickel. The curve shows that the [111] direction is the easiest to magnetize and the [100] direction the magnetic hardest direction.[16]

2.2.3. Permeability

The permeability connects the auxiliary magnetic field H and the magnetic field $B = \mu H$. As it is common for the physics of magnetism, all further equations and most units will be in the cgs-system. For a ferromagnetic sample the permeability is not linear, it rises until a maximum and then declines as seen in figure 2.6.

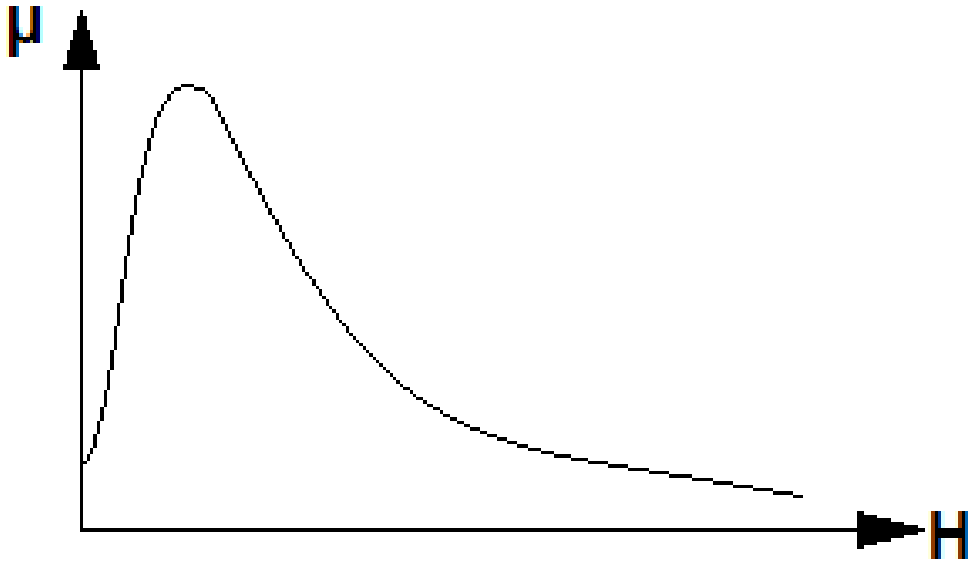

Figure 2.6.: Permeability curve for ferromagnetic material. μ : permeability, H : applied magnetic field

3. Experimental Procedure

This chapter presents the experimental executing of this thesis. Section 3.1 describes the samples processing and structure. In section 3.2 the process of the measurement is explained.

3.1. Sample Preparation

The nickel used for the deformation process was supplied by Goodfellow Cambridge Limited. The chemical composition according to supplies is as follows (table 3.1).

Table 3.1.: Impurities in the nickel

Element	wt. ppm
Antimony	0.5
Carbon	7.5
Cobalt	1.1
Copper	0.3
Iridium	0.3
Osmium	0.4
Rhenium	0.5
Silicon	0.2
Tantalum	< 1
Titanium	0.4
Yttrium	0.1

The used nickel therefore had a purity of ~ 99.9945 wt%. It was deformed using HPT, ECAP and CR.

The HPT disc was turned 5 times with a pressure of 3 GPa at 0.4 rpm. The process was executed under quasi-constrained conditions at liquid N_2 temperature ($-196\,^{\circ}$C).
The cylindrical sample used for ECAP was deformed at room temperature with a die angle of 120° and a curvature of 27.8° with 6 mm/s. No additional lubricant was used. 12 passes with route Bc (billet is rotated 90° clockwise, details in [3], [17]) were carried out leading to a total stress $\epsilon_{total} = 12 * 0.62 = 7.44$.
In the CR process the form was precooled with liquid nitrogen and deformed once at room temperature with a decrease in thickness of 25%.

3.1.1. Sawing

An Isomet 5000 linear precision saw was used for cutting the samples. The samples were cut out of a HPT disc (HPT-series), an ECAP cylinder (ECAP-series), a cold rolling form (CR-series) and an untreated form (Ref-series). The HPT and CR forms were deformed and provided by the Erich Schmid Institute (ESI Leoben). They also provided the reference form. The ECAP form was deformed and provided by AIT - Austrian Institute of Technology.

A slice of the HPT disc rather close to the center was used for the samples. Seven samples were cut from the slice as shown in figure 3.1 and two samples were cut out of an ECAP cylinder as shown in figure 3.2.

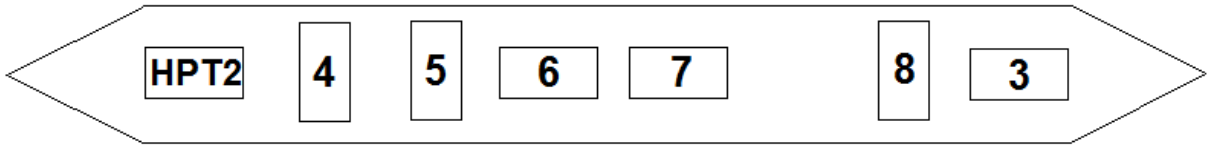

Figure 3.1.: Positions and number of the samples, which were cut from the HPT disc slice

From the CR platelets one sample was cut tangential and one normal to the rolling direction. The HPT, ECAP and CR forms were tempered before they were deformed, the untreated form was not. The mass and dimensions of the samples were measured with Sartorius Scale ($\Delta m = 0.01$ mg) and a slide gauge (Δl =0.05 mm). The measured data are summarized in table 3.2 and 3.3.

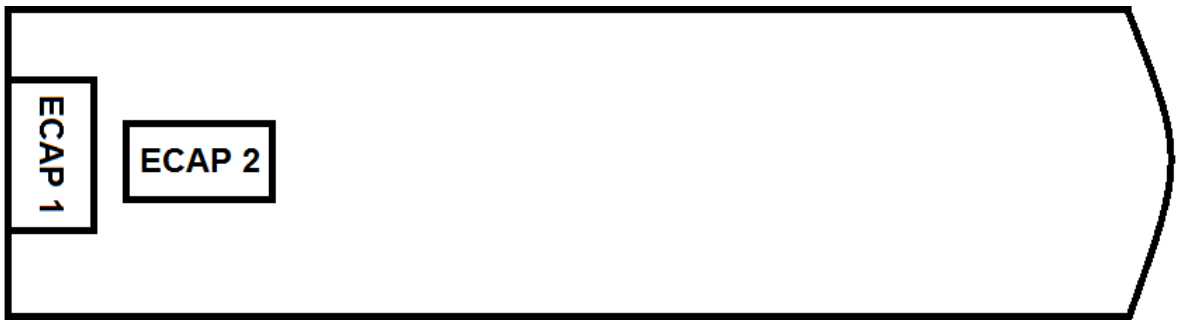

Figure 3.2.: Positions and designation of the samples, which were cut from the ECAP cylinder

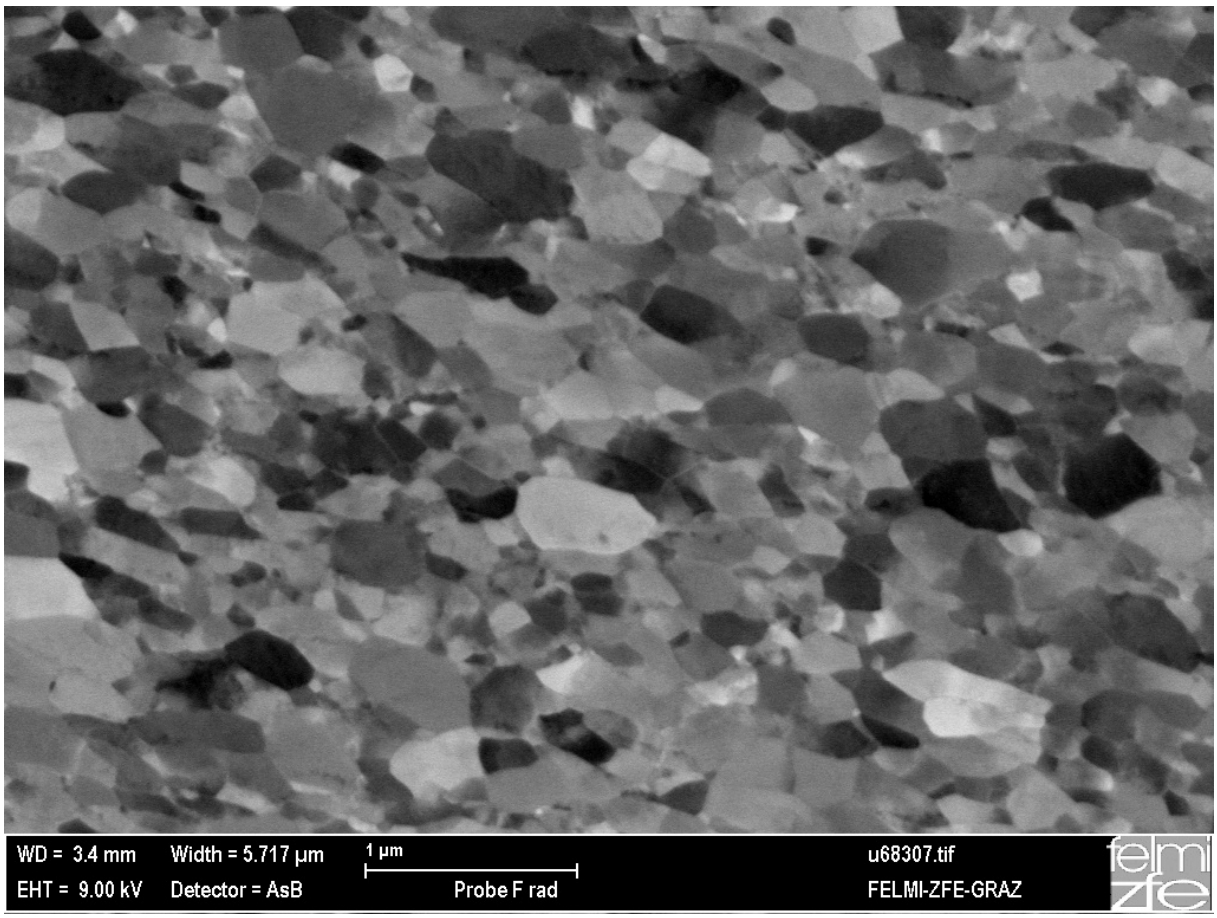

Figure 3.3.: Scanning electron micrograph of a HPT-Ni sample deformed with 5 rotations at room temperature. The grains are elongated from the left-upper direction to the right-lower direction with a size of $\sim 220 \times 120\,\text{nm}$.

In figure 3.3 a measurement with an electron microscope of a HPT-Ni samples is shown. The figure shows that the grains are elongated from the left-upper direction to the right-lower direction with a size of $\sim 220 \times 120\,\text{nm}$.

Table 3.2.: Dimensions and mass of the samples after cutting (before polishing)

Sample	Orientation	Dimensions [mm^3]	Mass [mg]
HPT2	radial	1.10x1.00x2.10	18.39
HPT3	radial	1.05x1.10x2.05	17.97
HPT4	axial	1.10x1.10x2.10	18.55
HPT6	tangential	1.10x1.20x2.10	19.63
HPT7	tangential	1.10x1.10x2.05	19.40
HPT8	axial	1.10x1.10x2.10	20.12

3.1.2. Polishing

With the exception of sample HPT3, all samples were chemically polished using an acid consisting of 10M HNO_3 (in H_2O) with dissolved 0.67M $CuSO_4$ x $5H_2O$ in order to remove surface parts of the sample which could have been affected by sawing. The polishing lasted 5 minutes, with an expected removal of 50 μm/side. After polishing the dimensions and the mass was measured again to see the occured changes (see table 3.3).

Sample HPT3 was left unpolished to determine whether the sawing had an influence on the magnetic measurements or not. As the slide gauge is not as precise as the scale, the values of the volume loss are less precise than those for the mass loss. Additionally, the samples are not perfect rectangular-shaped, as nickel is a soft metal and bends slightly during the sawing procedure.
The loss of mass prooves that the polishing removed an equal amount of all samples as it is within 1% deviation. For HPT2 it is a bit higher because we first polished it for 10 minutes in an identical solution.

3.1.3. Annealing

After measuring the samples as prepared, some samples were temperature annealed using a Linseis L75 VD LT dilatometer, which had the following specifications:

Table 3.3.: Dimensions and mass of the samples after polishing and percentage loss of volume and mass due to polishing

Sample	Orientation	Dimensions [mm^3]	Mass [mg]	Volume loss	Mass loss
HPT2	radial	1.00x0.95x2.05	16.46	19%	12%
HPT4	axial	1.00x1.05x2.05	16.85	18%	10%
HPT6	tangential	1.05x1.15x2.05	17.78	12%	10%
HPT7	tangential	1.00x1.05x2.00	17.75	21%	9%
HPT8	axial	1.00x1.05x2.05	18.36	18%	10%
ECAP1	axial	1.05x1.00x2.00	17.49	-	-
ECAP2	tangential	1.05x1.00x2.00	17.37	-	-
Ref1	-	1.15x1.10x2.10	19.91	-	-
Ref2	-	1.10x1.10x2.15	20.38	-	-
CR N	normal	1.10x1.10x2.10	19.57	-	-
CR T	tangential	1.10x1.10x2.10	19.55	-	-

Range: -150 – 500 °C
Heat rate: 0.1 – 50.0 °C/min
Accuracy: ±150 nm
Maximum length change: ±2.5 mm

The annealing procedure was:

- Cooling to 0°C with 3°C/s
- Hold temperature for 10 minutes
- Heating to target annealing temperature with 3°C/s
- Cooling to 20°C with 20°C/s

The samples were mounted in vertical orientation (x-y plane at the bottom, see figure 3.6).

As the dilatometer was limited to an annealing temperature of 500 °C, an additional vacuum furnace was used to further anneal the samples to higher temperatures.

3.2. Measurement of the hysteresis loop

Measurements were performed with a SQUID (**S**uperconducting **Qu**antum **I**nterference **D**evice)-Magnetometer (MPMS-XL-7, Fa. Quantum Design) in the group of Univ.-Prof. Heinz Krenn, associated with Karl-Franzens-Universität Graz. According to specifications [18] the error in measurement is below 10^{-8} emu for fields lower than 2500 Oe and below $6 \cdot 10^{-7}$ for fields up to 70000 Oe.

The SQUID-Magnetometer consists out of three superconducting coils (precisely four as the middle one is doubled) which form a gradiometer of second-order.

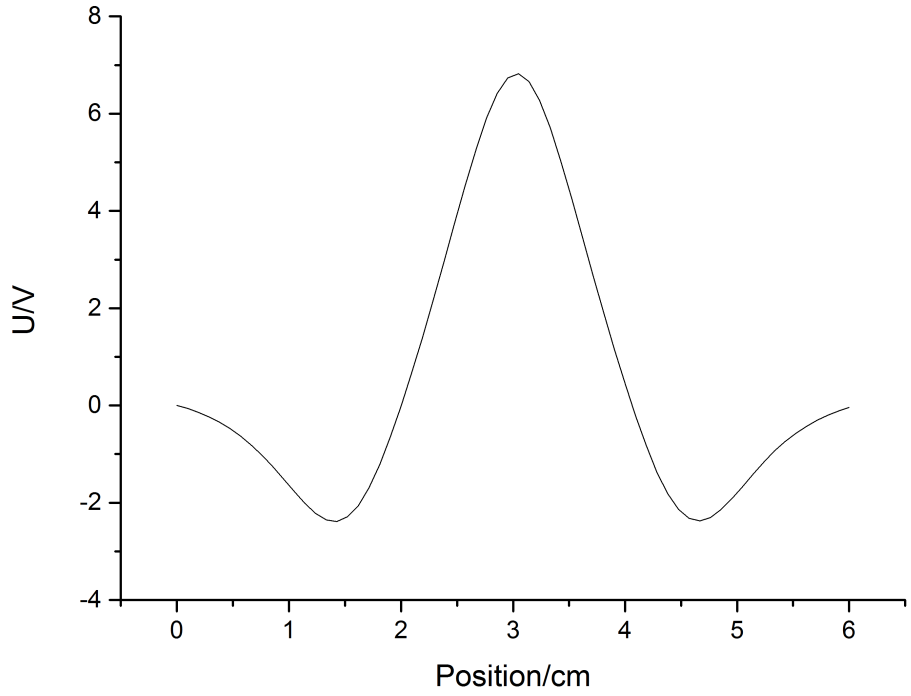

Figure 3.4.: Measured signal of the SQUID-Magnetometer at a constant applied magnetic field.

Measurement with a SQUID works as follows: A superconducting magnet generates a homogeneous magnetic field, which magnetizes the sample. In the center of the magnetic field a superconducting detector coil is placed. The sample is moved in discrete steps through the detector coil, which induces a current. This current is proportional to the change of the magnetic flux. This induced current is connected with a different superconducting coil to the SQUID-sensor via induction. The SQUID-sensor consists of a superconducting ring with Josephson junctions and is very sensible to

flux changes. The changes in the magnetic flux trigger a change in the current of the SQUID-sensor. Using an oscillator circuit the voltage can be obtained. The current for the outer coils is inverse to the current of the inner coil, creating the characteristic measurement seen in figure 3.4. Fitting the peak voltage of the measured signal with a model function for an ideal point-shaped magnetic dipole the magnetization M can be calculated.

In order to measure the hysteresis loop of the samples with the SQUID, the samples had to be attached to a specimen holder as seen in figure 3.5. This holder consists of a nonmagnetic transparent straw, a black cable tie, vacuum grease and cotton. The cable tie was placed inside the straw and the cotton (leftmost white substance in figure 3.5) was used on the lower end to hold the cable tie in place. The long sample holder was used so that no change in magnetisation occurs during measurement because of the sample holder (during measurement the sample holder is moved up and down). A drill with a 1 mm drill bit was used to create a space for the sample, which was fixed using vacuum grease. Before measuring the grease was left to harden for a while, so that the sample cannot move or start swinging while measuring. As nickel is ferromagnetic the measured magnetic moment is several orders higher than of the materials used in the sample holder, which can therefore be neglected.

Figure 3.5.: Picture of the sample holder, which was inserted into the SQUID, with a nickel sample mounted in (red arrow). The blue arrow indicates the direction of the applied magnetic field H in the SQUID when the sample holder is mounted in.

For the measurement the program MPMS MultiVu Application was used.

The geometry of the mounted in sample is represented in figure 3.6.

A list of the measurements carried out is shown in table 3.4. All measurements were executed at T =27 °C.

Table 3.4.: List of samples and sample conditions for SQUID Measurements. For sample orientation see figure 3.1 and 3.2

Sample	Orientation	Polished	Sample condition
HPT2	radial	✓	as prepared
HPT3	radial	×	as prepared
HPT4	axial	✓	as prepared, annealed at $100°C, 160°C, 220°C, 500°C$
HPT6	axial	✓	as prepared
HPT7	tangential	✓	as prepared, annealed at $100°C, 160°C, 220°C, 500°C$
HPT8	tangential	✓	as prepared, annealed at $160°C, 220°C, 500°C$
ECAP1	axial	✓	as prepared
ECAP2	tangential	✓	as prepared
Ref1	-	✓	as prepared, annealed at $500°C$
Ref2	-	✓	annealed at $1000°C$
CR N	normal	✓	as prepared, annealed at $500°C$
CR T	tangential	✓	as prepared

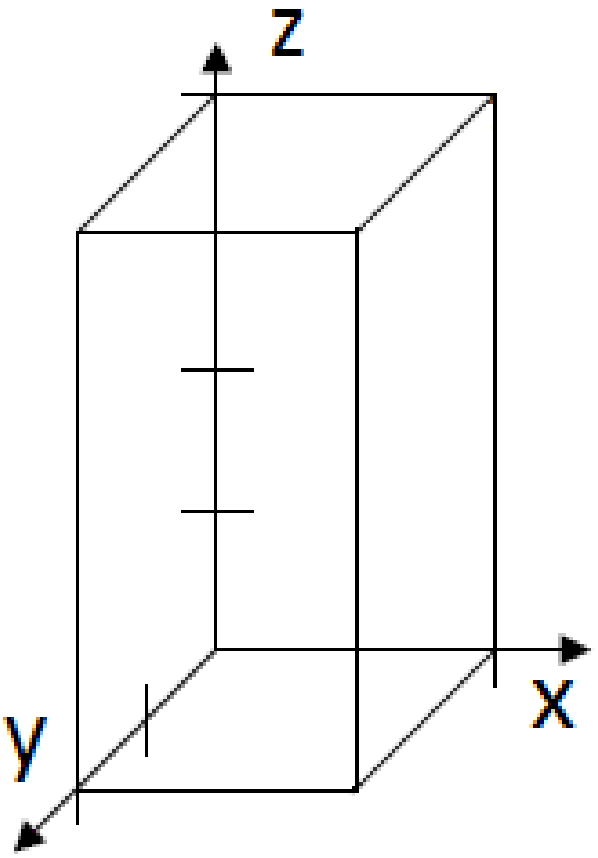

Figure 3.6.: Sketch of the sample with which the SQUID measurements were performed.

4. Results

In this chapter the results of the measurements will be presented.

At first a length change measurement from the dilatometer was conducted (section 4.1). Then a full hysteresis loop was measured (section 4.2). Afterwards to determine the reason for the slight change in saturation magnetization, multiple measurements with the same sample were executed (subsection 4.2.1). Then the hysteresis loops for the non annealed (a.p.) and the annealed states were measured (subsection 4.2.2). The saturation magnetization and the remanent magnetization of all measured samples are summarized in subsection 4.2.3. In the final subsection (4.2.4) additional measurements for higher fields (up to 70000 Oe compared to the 20000 Oe for the previous measurements) were executed.

4.1. Dilatometric characterization of annealing behavior

Figure 4.1 shows the variation of length of an axial HPT nickel sample compared to an undeformed reference sample in the dilatometer upon time-linear heating. The black curve represents the measured data points; the dashed colored vertical lines have been added to show the different stages at which the annealing process was stopped and a measurement with the SQUID was conducted.

The dilatometer curve is explained by Steyskal and Oberdorfer [1] by dividing it into different areas. In the first area (below 100 °C) there is hardly any difference between the deformed and the reference sample. In area between 100 °C and 160 °C predominant vacancies anneal out at grain boundaries and at dislocations. The next area between 160 °C and 220 °C is dominated by recrystallization processes and grain

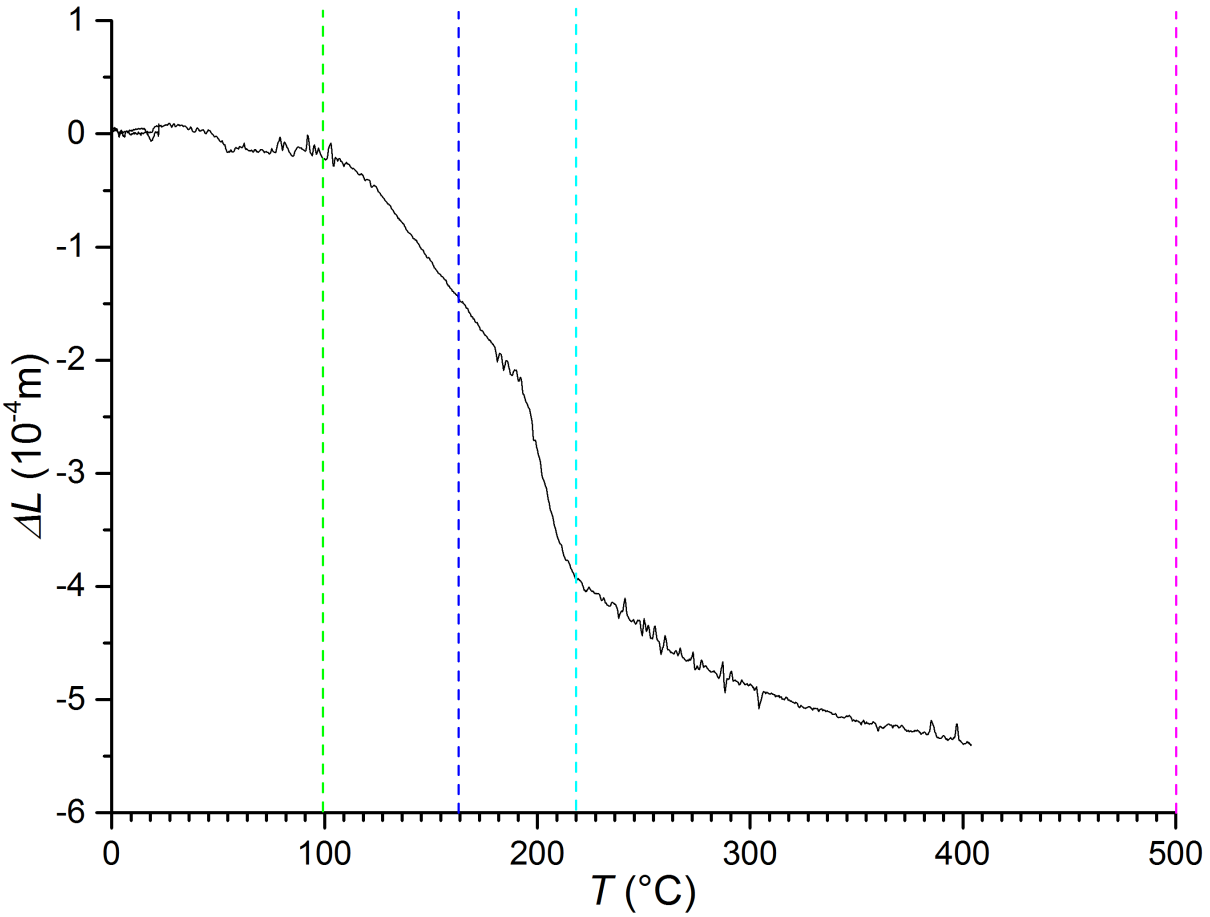

Figure 4.1.: Variation of the length ΔL of an axial HPT nickel sample during annealing (temperature T). The vertical dashed lines indicate the final temperatures upon linear heating for the magnetic measurements. Those temperatures are the boundaries between different annealing processes as will be explained in the text.

growth. In the final area (>220 °C) void shrinkage (bulk- and pipe-diffusion) and further grain growth is dominating.

4.2. Measurement of hysteresis loops

Figure 4.2 shows a full hysteresis loop for the sample HPT2, which is a sample in the as prepared state (without annealing). For comparison the measured magnetization (unit emu) is related to the mass of the sample (emu/g).

A full hysteresis loop ± 20000 Oe took $\sim$ 6 hours to measure. Therefore to save time and furthermore coolant, the measuring range was restricted to the positive branch. The areas of interest, ± 300 Oe and $1000 - 4000$ Oe, were scanned more precise for better evaluation. Further plots will focus on those areas.

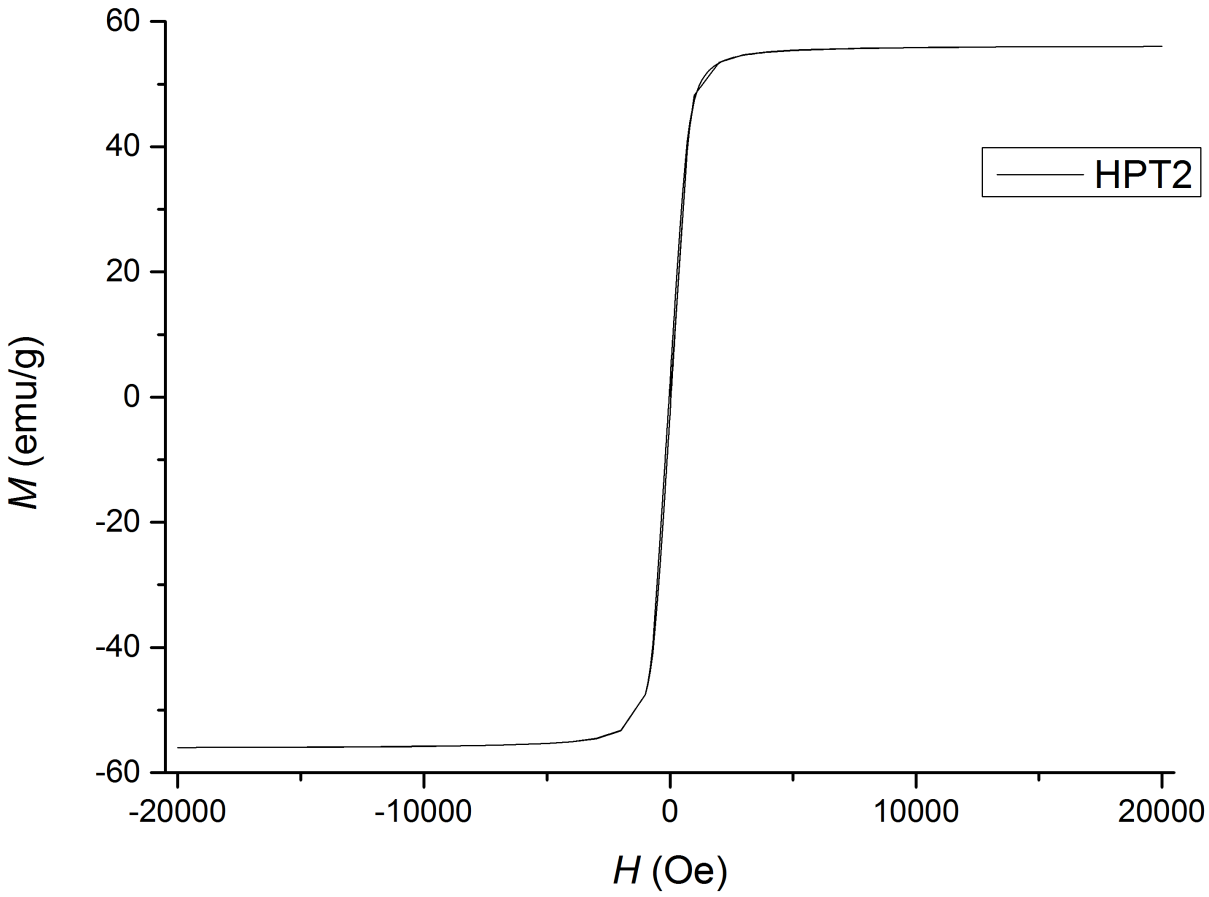

Figure 4.2.: Full hysteresis loop of sample HPT2 in the as prepared state (without annealing). As nickel is very soft magnetic there is almost no hysteresis area. M : specific magnetization, H : applied magnetic field.

In figure 4.3 the virgin curves for all HPT as prepared samples are plotted. For HPT2 and HPT3 the only difference is the chemical polishing. This figure shows the differently oriented samples (radial, axial and tangential) together. Additionally, compared to all other samples, HPT7 was also mounted perpendicular in the sample holder, as figure 4.3 shows, it is harder to magnetize in this direction. The influence of the different preparation methods and sample position will be discussed in section 5.1. In the subplot the area around zero is highlighted, showing that all samples, except HPT7 $\perp$ placed, have the same slope. Demagnetizing was conducted before every measurement by flipping and decreasing the applied magnetic field (100 Oe, -50 Oe, 20 Oe, -10 Oe). The virgin curve of "HPT7 tangential polished" starts higher than the other curves due to residual magnetism in the magnetic coils of the SQUID. In order to save He costs it was omitted to get rid of this residual magnetism by demagnetizing as it only decays slowly with time.

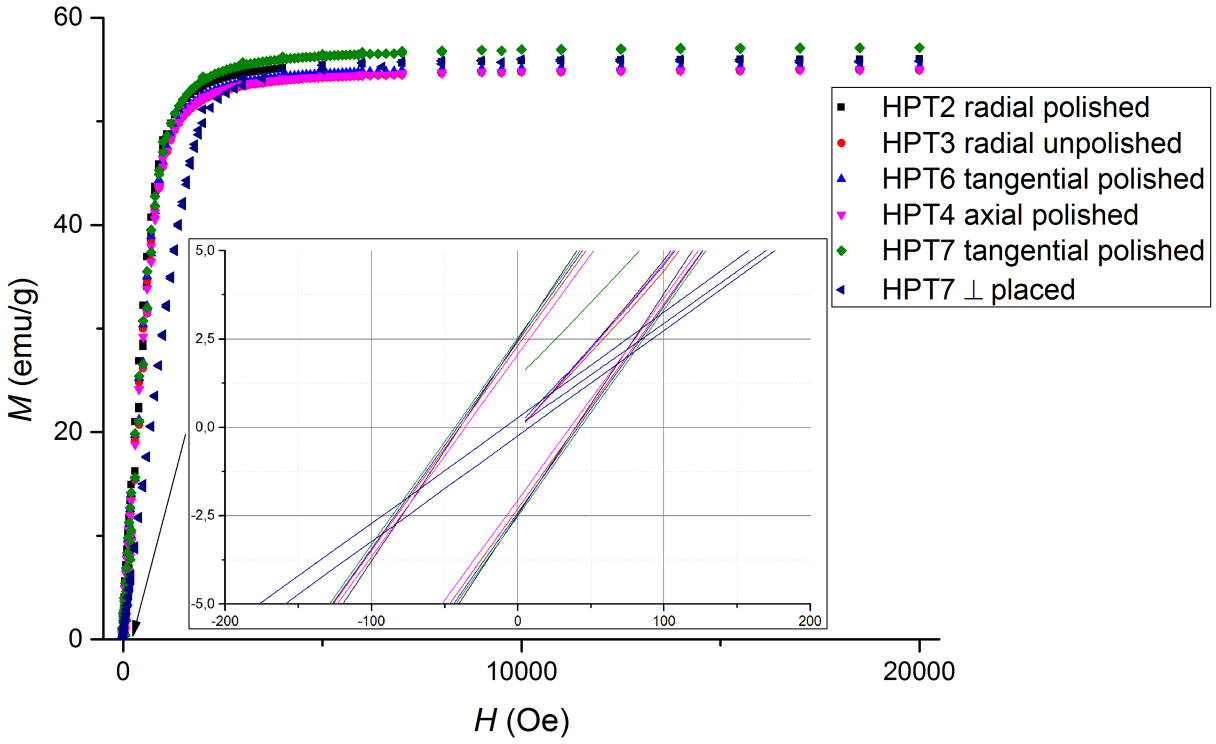

Figure 4.3.: Positive half of the hysteresis loops of all measured HPT samples in the as prepared state (without annealing). The samples were differently prepared (either polished or not) and differently cut from the disc (axial, radial, tangential). Additionally, compared to the other samples, which were placed with the z-axis parallel to the magnetic field, the HPT7 sample was also measured with the z-axis perpendicular to the magnetic field (HPT7 $\perp$ placed). The area around zero is magnified in the subplot. M : specific magnetization, H : applied magnetic field.

4.2.1. Influence of exact sample positioning on saturation magnetization

As seen in figure 4.3 the saturation magnetization for each sample is slightly different despite being normed by their masses. Additional measurements with the sample HPT7 500°C were conducted (see figure 4.4) to find whether the differences arise from sample mounting. Position P1 has no relation to the further measurements. In position P2 three hysteresis loops (measurement M1, M2, M3) were carried out without changing the sample position. For position P3 the sample was taken out of the sample holder and build in upside-down (180 ° turn along the x-axis) compared to position P2. For P3+45°z the sample holder was rotated along the z-axis by 45° without removing it from the magnetometer.

The saturation magnetization of nickel is 55.1 emu/g according to literature[19]. The

saturation magnetization of all measured samples is within a 4% range of this value. The values for the saturation magnetizations can be found in table 4.1.

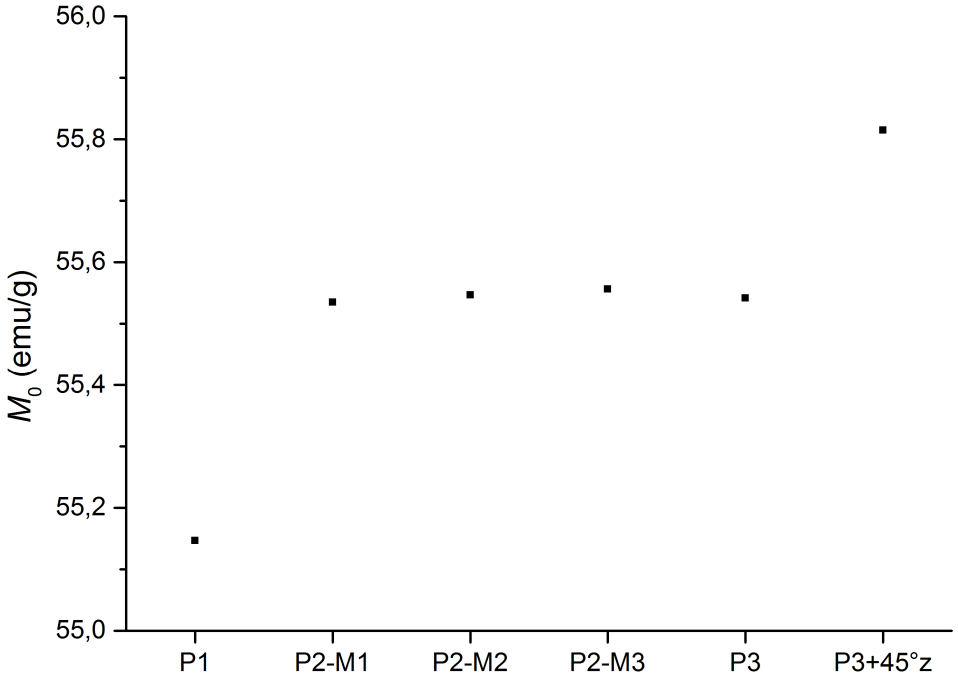

Figure 4.4.: Influence of sample mounting on the saturation magnetization M_0 of sample HPT7 after annealing at 500°C. The sample was remounted into the sample holder three times (position P1, P2, P3). For the position P2 multiple measurements (M1, M2, M3) were executed. At the position P3 the sample was turned by 180° along the x-axis in comparison to P2. Additionally, the sample was rotated by 45° along the z-axis without removing the sample from the magnetometer (P3+45°z).

4.2.2. Influence of annealing on the magnetization curve of HPT-samples

For the samples HPT4 and HPT7 additionally to the measurement of the hysteresis loop as prepared, the samples were temperature annealed and measured again (figure 4.5). The details to the annealing can be found in section 4.1.

As mentioned in section 4.2, for some measurements it was not possible to get rid of the residual magnetism in the coils, which can be observed for the ”HPT4 100°C” curve and to a minor extend also for the ”HPT4 500°C” curve (see the subplot figure 4.5(a)).

Table 4.1.: Saturation magnetization M_0 at 20000 Oe and remanent magnetization M_r for both half hystereses of the magnetic measurements

Stage	Orientation	M_0 (emu/g)	M_r (emu/g)
HPT2	radial	56.01	2.48/-2.47
HPT3 (unpolished)	radial	54.93	2.31/-2.30
HPT6	tangential	55.28	2.43/-2.42
HPT4 a.p.	axial	54.99	2.07/-2.06
HPT4 100°C	-//-	55.27	2.02/-2.01
HPT4 160°C	-//-	56.51	1.68/-1.66
HPT4 220°C	-//-	55.75	0.03/-0.02
HPT4 500°C	-//-	55.57	-0.53/0.53
HPT7 a.p.	tangential	56.12	2.54/-2.52
HPT7 100°C	-//-	56.01	2.43/-2.41
HPT7 160°C	-//-	55.58	1.95/-1.94
HPT7 220°C	-//-	54.96	0.01/-0.03
HPT7 500°C P1	-//-	55.15	-0.49/0.52
HPT7 500°C P2-M1	-//-	55.53	-
HPT7 500°C P2-M2	-//-	55.54	-
HPT7 500°C P2-M3	-//-	55.55	-
HPT7 500°C P3	-//-	55.54	-
HPT7 500°C P3+45°z	-//-	55.81	-
HPT7 500°C $\perp$	-//-	55.82	-0.24/0.27
ECAP1	axial	55.36	2.29/-2.28
ECAP2	tangential	55.16	2.20/-2.19
CR T	tangential	55.07	1.93/-1.99
CR N	normal	55.20	1.39/-1.43
CR N 500°C	-//-	54.94	-0.43/0.45
Ref1	-	55.13	1.12/-1.18
Ref1 500°C	-	55.01	-0.43/0.46
Ref2 1000°C	-	55.48	-0.55/0.58

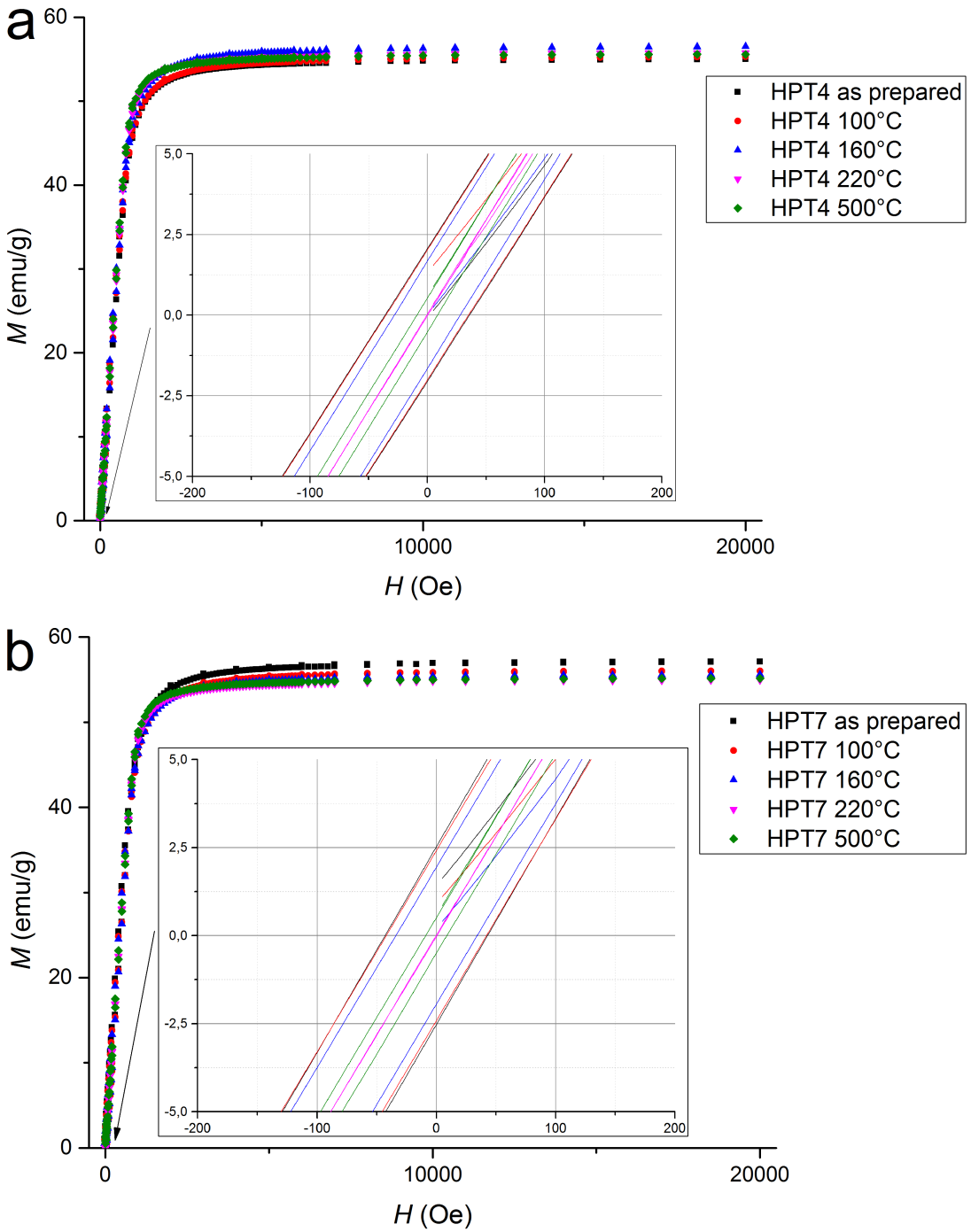

Figure 4.5.: Positive half of the hysteresis loops of samples HPT4 (a) and HPT7 (b) in the as-prepared state and after annealing at different temperatures. The area around zero is magnified in the subplot. M : specific magnetization, H : applied magnetic field.

The residual magnetism is the magnetic moment remaining at a field of 0 Oe. As seen in table 4.1, the saturation magnetization hardly changes. The residual magnetization, however decreases slightly after annealing at 160°C and almost disappears for $T_a =$ 220°C. At the highest annealing stage of 500°C an inverted magnetic hysteresis is observed, details to this phenomena are explained in section 5.2. In figure 4.5(b) the

same plot as figure 4.5(a) for HPT7 is shown. In the subplot there are also several cases of residual magnetism in the coils.

4.2.3. Magnetization curves of ECAP, CR and Reference samples

In figure 4.6 the magnetization curves for samples of the types ECAP, CR and reference are plotted. Deviations at the start of the virgin curves are due to residual magnetism in the magnetic coils of the SQUID. This residual magnetism can be either positive or negative.

4.2.4. High-field measurements

For studying the approach to ferromagnetic saturation, measurements at high magnetic fields are required. For instance, Kisker [10] worked with fields which are well above our maximum field of 20000 Oe used in the measurements so far. Therefore additional measurements from 7500 Oe to 70000 Oe were executed as shown in figure 4.7. For studying the annealing behavior a new axially oriented sample HPT8 was used. For comparison the annealed axially oriented sample HPT4 was also measured (figure 4.7(a)). A few selected differently processed samples were measured as well (figure 4.7(b)).

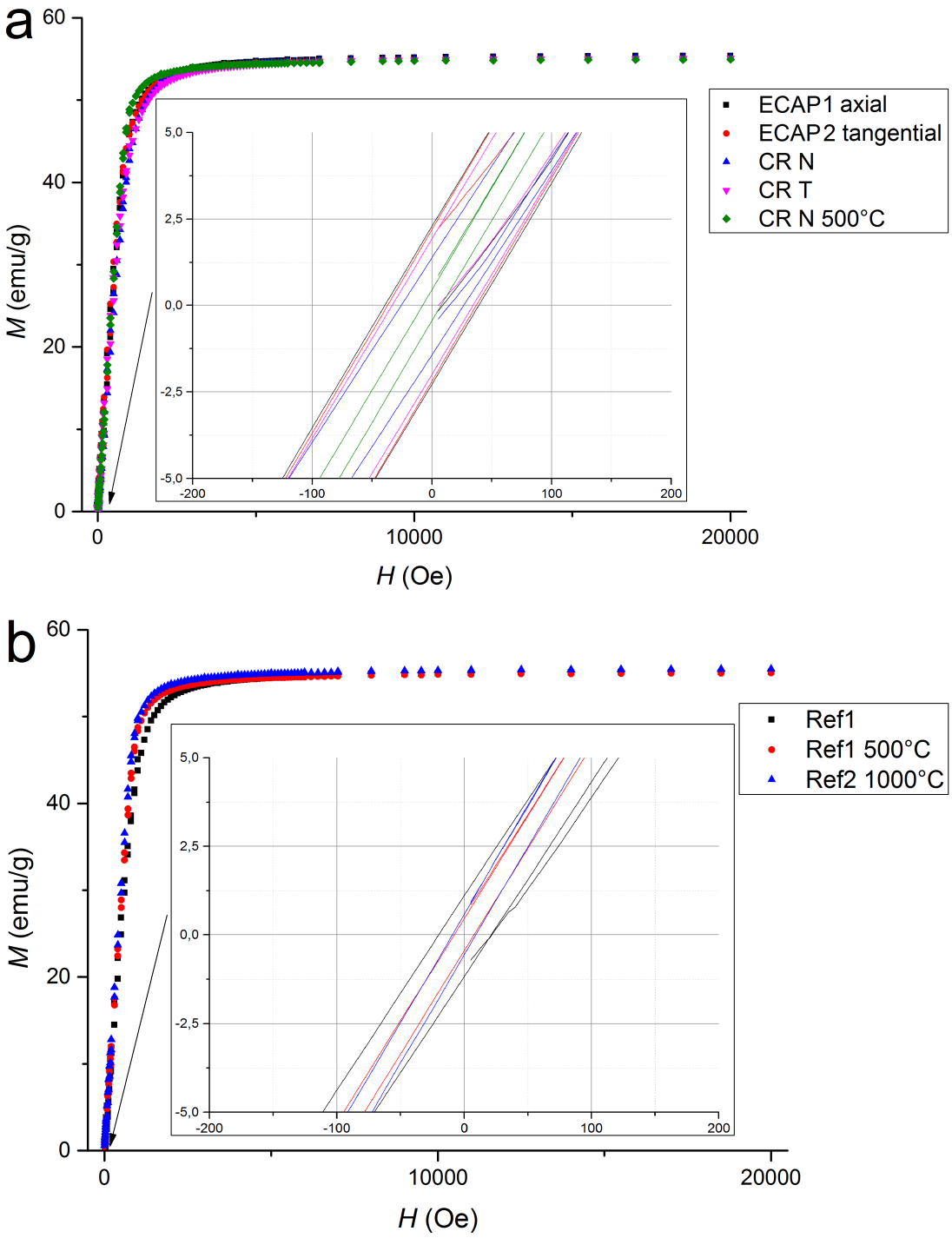

Figure 4.6.: Positive half of the hysteresis loops of all ECAP and CR samples (a) and of all reference samples (b). Details on the samples can be found in table 3.4. The area around zero is magnified in the subplot. M : specific magnetization, H : applied magnetic field.

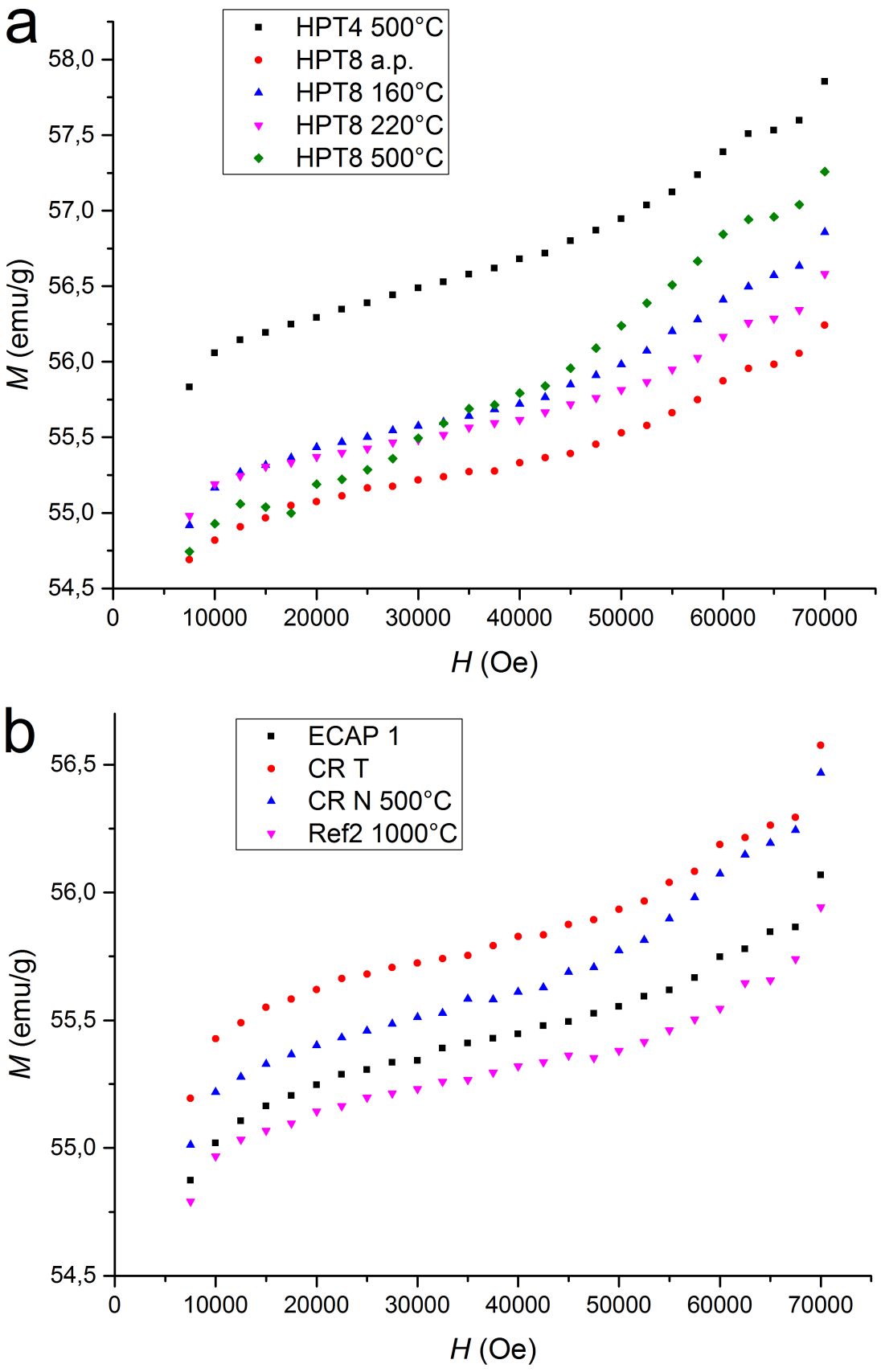

Figure 4.7.: High-field measurement of the magnetization for samples HPT4 and HPT8 (a) and for sample types ECAP, CR and reference (b) in the as-prepared state and after annealing at different temperatures. M : specific magnetization, H : applied magnetic field.

5. Analysis and Discussion

In this chapter the results measured in chapter 4 will be analyzed and discussed.

The first section (5.1) deals with the influence of the different grain orientations, and with the influence of chemical polishing and the positioning of the sample in the magnetometer. Section 5.2 discusses the coercivity and changes which happen to it due to annealing. In the section 5.3 H-field dependence is divided in different ranges. Section 5.4 deals with the low-field which is particular specific with respect to permeability and coercivity. The next higher H-field part area is dealt with in section 5.5. This area is mainly dominated by rotation processes. In the high-field area (section 5.6), the approach to saturation is analyzed according to the model equation (2.3).

5.1. Influence of sample preparation and positioning

In this section the different influences of grain orientation, polishing and geometry will be discussed. A compilation of sample data is given in table 4.1.

5.1.1. Influence of sample orientation with respect to deformation axis

The grains in the samples are oriented in a preferred direction due to the deformation process elongating them (see figure 3.3). The grain orientation depends on how the samples are cut from the form. As seen in table 4.1, the saturation magnetizations for the HPT samples lie all in the same range and are independent of the grain orientation of the samples. The same can be said for the ECAP samples, indicating that other effects are deciding.

5.1.2. Influence of polishing

The polished sample HPT2 and the unpolished sample HPT3 show hardly any difference in their saturation magnetization and remanent magnetization (see table 4.1). This shows, that sample cutting using a high speed saw at a slow forward feed, produces a negligible amount of modifications on the surface of the sample.

5.1.3. Influence of the sample position in the SQUID

In figure 4.4 the saturation magnetization M_0 for the same sample and different positioning is displayed. The data for the saturation magnetization can be found in table 4.1.

For different samples the largest difference in M_0 is between HPT3 and HPT7 a.p. with 3.8% (figure 4.3). For the same sample (HPT7 500°C) the result is reproducible if the initial situation is not changed (within 0.04%) as seen in figure 4.4 by the multiple measurements (P2-M1/2/3). There is no correlation between position P1 and position P2. However between position P3 and P3+45°z the sample holder was rotated. Analyzing the differences between the positions and measurements, it can be concluded, that the alignment of the sample in the SQUID is responsible for the change in M_0. For the HPT7 500°C sample a difference of 1.2% was observed (difference between P1 and P3+45°z). Another factor for alignment is the sample holder. For all measurements of HPT7 500°C the same sample holder was used, however for other samples other sample holders were used. As the samples were placed in holes that were drilled, the holes can be slightly tilted, which can add an additional deviation. This can be explained with magnetic field lines as seen by the bar magnets in figure 5.1.

As seen in figure 5.1 at the left side the sample is perfectly placed in the field lines and the applied magnetic field can easily magnetize to saturation magnetization. On the right side, on the other hand, in the red areas the field lines cannot perfectly enter and exit the sample, which means an additional external field is necessary to achieve the same M_0 as on the left side. Due to the same reasons, for different samples (e.g.

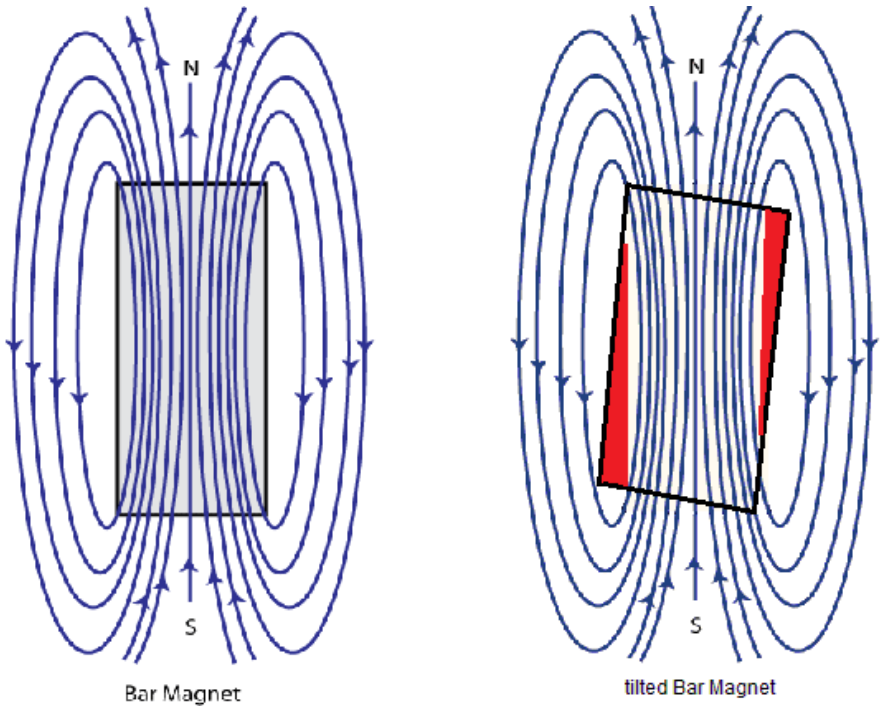

Figure 5.1.: Magnetic field lines for a bar magnet and a tilted bar magnet. [20] As can be seen the field lines in the right sample can not enter and exit the sample perfectly. Therefore an additional field is necessary for the red areas to reach the same magnetization. S, N: magnetic south and north pole respectively and blue arrow lines as field lines.

HPT3 and HPT7) a deviation from a perfect cuboid can further increase the difference in M_0.

It can therefore be concluded that the alignment of the sample in the SQUID magnetometer is responsible for the fluctuations of the measured M_0 of samples for different annealing stages; for different samples a deviation from a rectangular shape can increase the effect.

5.2. Coercivity

Figure 5.2 shows the coercivity for the various samples deduced from their respective magnetic hysteresis. All HPT as prepared samples have almost the same coercivity, therefore HPT7 a.p. is representative for them. The HPT4 and HPT7 samples at different annealing stages have almost the same coercivity, therefore HPT4 was omitted (see table 5.1).

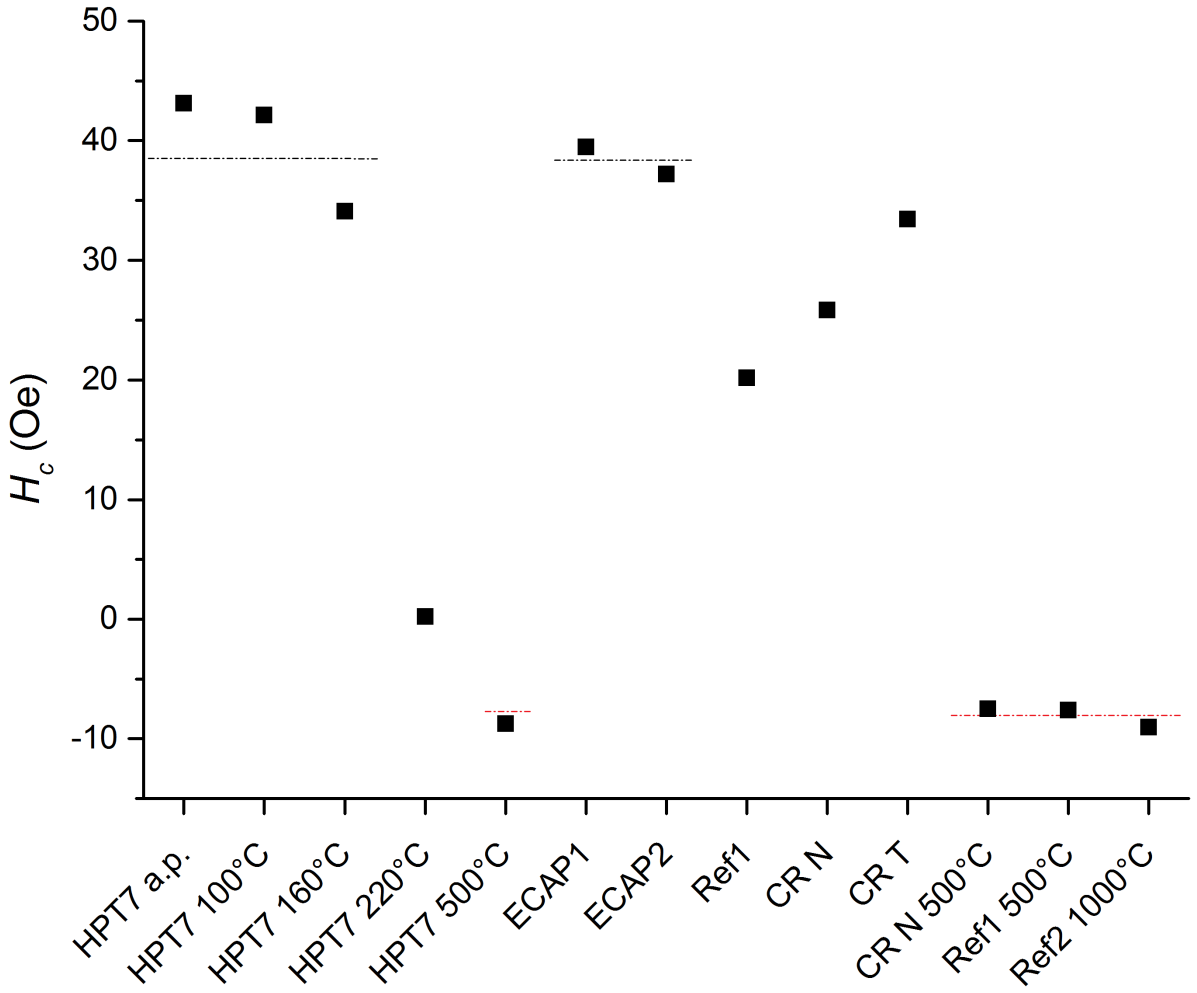

Figure 5.2.: Coercivity H_c of different samples. Note: The negative coercivity values for some samples are due to a measurement error of the SQUID (see text for details). The black and red point dashed lines characterize samples that show the same behavior.

The coercivities of HPT samples before recrystallization ($\leq$160 °C) and of ECAP samples are similar, which is indicated in figure 5.2 by the black point dashed line. The CR samples have a smaller coercivity and the reference sample has the smallest (of the not annealed samples). There is a clear distinction in coercivity for samples after the recrystallization ($T_a \geq 220$°C), as all samples have a clearly lower coercivity afterwards (red point dashed line). Löffler also reaches this conclusion in his article [21].

In figure 5.3 the coercivity values for the magnetization and for the demagnetization are plotted as a function of the annealing temperature for samples HPT4 and HPT7.

In Hanmin [22] it is mentioned that an inverted hysteresis is observed due to bad positioning, therefore sample HPT7 500°C was built in perpendicular and an additional measurement was conducted. The measured hysteresis loop is plotted in figure 4.3. As it still has an inverted hysteresis, the positioning was not the deciding reason.

Table 5.1.: Coercivity deduced from the magnetic hysteresis. UHH: Upper Half Hysteresis, LHH: Lower Half Hysteresis

Sample	Coercivity UHH [Oe]	Coercivity LHH [Oe]
HPT3	39.8	−39.7
HPT6	41.3	−41.3
HPT4 a.p.	36.0	−35.9
HPT4 100°C	35.3	−35.1
HPT4 160°C	28.2	−28.1
HPT4 220°C	0.4	−0.4
HPT4 500°C	−8.5	8.4
HPT7 a.p.	43.1	−43.0
HPT7 100°C	42.1	−41.9
HPT7 160°C	34.1	−34.0
HPT7 220°C	0.2	−0.2
HPT7 500°C	−8.7	8.6
ECAP1	39.4	−39.4
ECAP2	37.1	−37.0
Ref1	20.1	−20.0
CR N	25.8	−25.7
CR T	33.4	−33.3
CR N 500°C	−7.5	7.4
Ref1 500°C	−7.5	7.5
Ref2 1000°C	−9.0	8.9
Ref3 500°C	−8.7	8.6

Another possible reason for the inverted hysteresis is the fact that "there is no absolute field sensor located anywhere in the magnetometer, so the magnetic field value reported to the user is based only on the current set by the power supply. Because a superconducting solenoid is used to generate the magnetic field, the user has to take into account the existence of pinned magnetic flux lines and flux movement within the magnet." [23] The two phenomena that cause this are superconducting magnet remanence and flux creep and escape. [23]

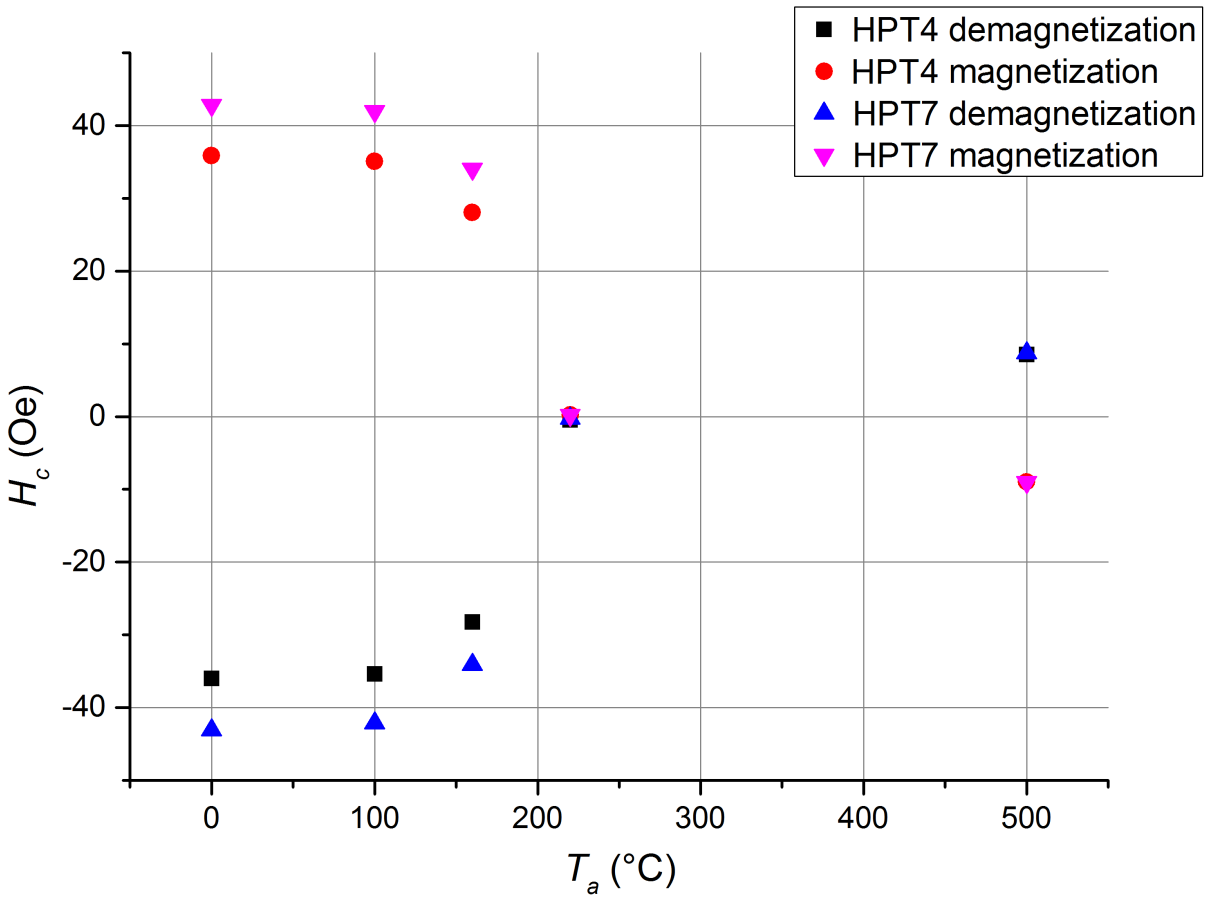

Figure 5.3.: Variation of the coercivity H_c with annealing temperature T_a of samples HPT4 and HPT7 for both the magnetization and the demagnetization. Note: The inverted coercivity values for $T_a = 500°C$ are due to a measurement error of the SQUID (see text for details).

This remanent magnetization is proposed as a reasons for the "inverted" hysteresis in [23] as the remanent magnetic field remains in the SQUID even if the magnetic coils are deactivated. To verify this, a gaussmeter was used to measure the remaining field without any applied magnetic field (during demagnetization). This device indeed verified that a field remains in the SQUID. However the remaining field was only 2.1 Oe, which is several times lower than the coercivity at the $T_a = 500°C$ stages.

Additionally, if a ferromagnetic sample is in the SQUID, a field can be trapped inside the material. This flux gets pinned at defects and remains even after discharging the magnet. This field has a very important characteristic: "it is directed opposite to the last experienced strong field by the magnet and assumes the largest values around the zero magnetic field. This results in a well-known 'negative' hysteresis, an apparent inverted (clockwise) magnetic field loop seen in soft ferromagnets" [23], which is exactly what is observed in our measurement. As this effect is only observable with a built-in sample it was not possible to measure with the gaussmeter.

A solution to this problem is proposed by first measuring the soft ferromagnetic material and afterwards using the same sequence to measure a paramagnetic salt (Dy_2O_3). Using those values it possible to calculate the real magnetic field acting upon the sample and the field error. As no suitable paramagnetic salt with the same geometry 2.6 was available, the real coercivity could not be determined.

5.3. Defining the lower-, medium-, and high-field regions

Figure 5.4(a) shows the regions in a linear plot for the virgin curve. As the areas are difficult to define in this plot, in figure 5.4(b) the y-axis was changed to $1 - M(H)/M_0$ and both axis are not linear but logarithmic. In this plot the areas are linked with the different slopes. Area I is below 500 Oe and as seen in figure 5.4(b) there is hardly any slope in this area. This area will be discussed in section 5.4. Area II is between 1000 Oe and 4000 Oe and the solid green line in this area shows that a $H^{-3/2}$ behavior is expected here. This area will be discussed in section 5.5. Area III is between 10000 Oe and 40000 Oe. The solid blue line shows that in this area a $H^{-1/2}$ behavior can be expected. This area will be discussed in section 5.6. Above 40000 Oe the para effect is dominant.

5.4. Low field area, Area I

The low field area or area I is below 500 Oe and the change in magnetization is mainly due to Bloch wall movement, as it happens before the magnetic domains tends to align parallel to the field. [16]

The permeability calculated by $\mu = \frac{dB}{dH}$ is plotted in figure 5.5(a)-(c).

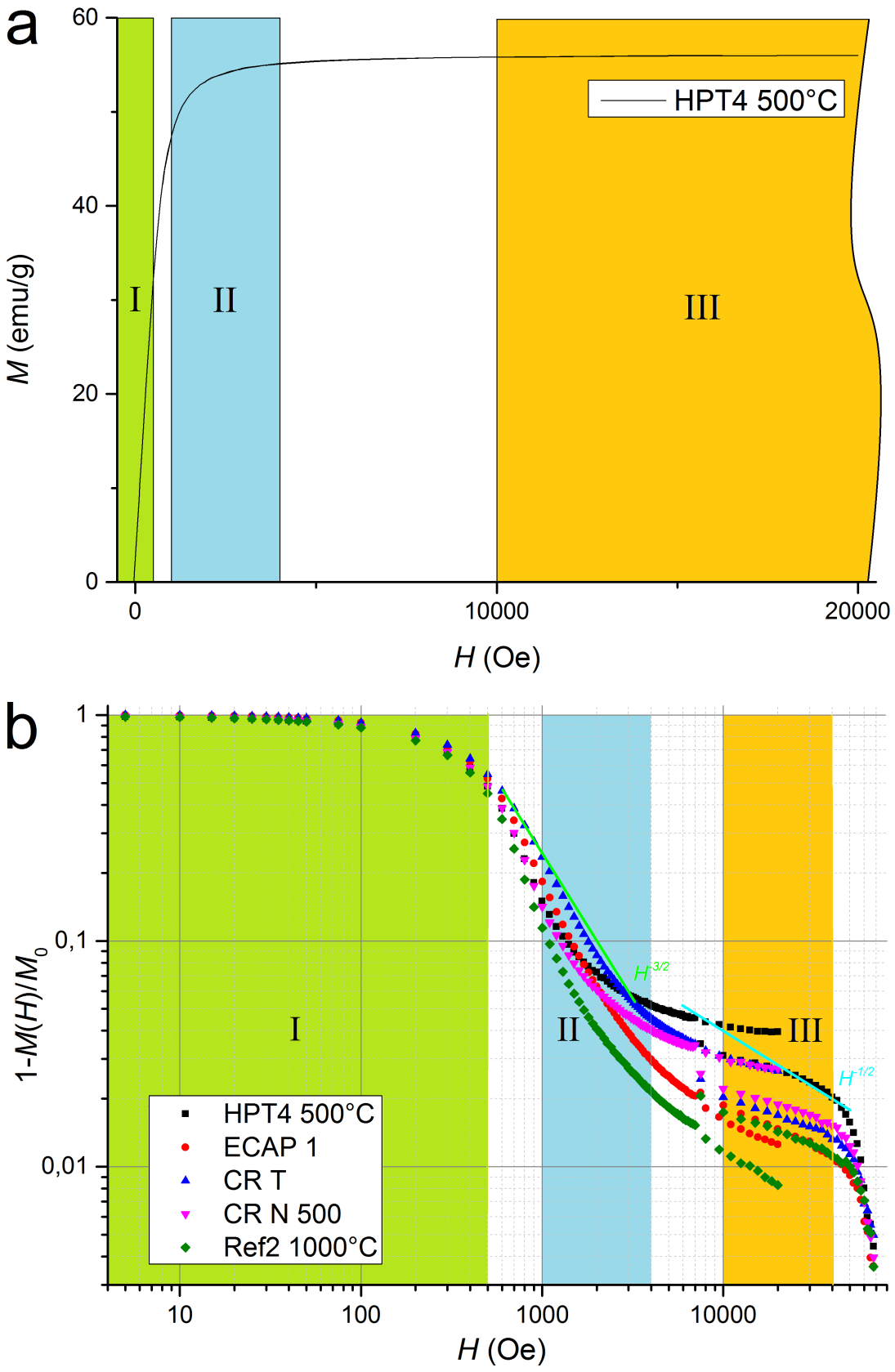

Figure 5.4.: Areas of interest in the positive half of the hysteresis loops. Plotted linearly (a) and double-logarithmic with $1 - M(H)/M_0$ as y-axis (b). The solid lines in (b) indicate the different processes occurring in the specific area (see text).

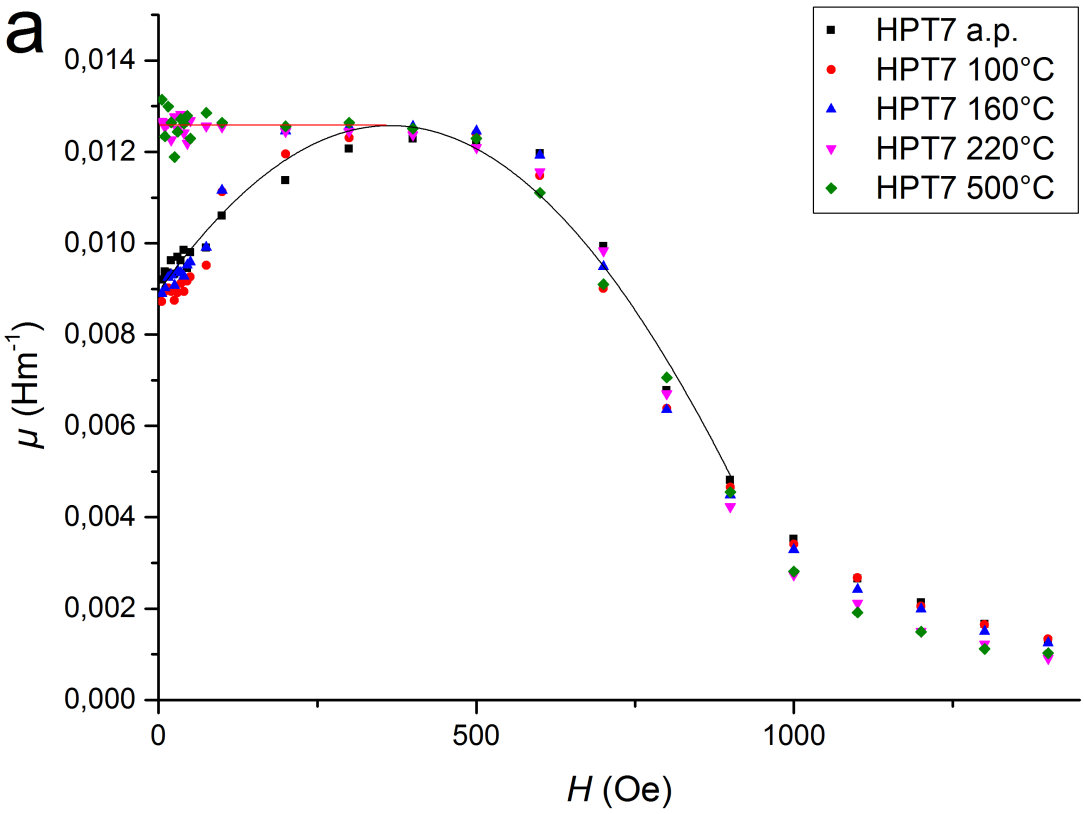

Figure 5.5.: Permeability μ of sample HPT7 (a), ECAP and CR (b), reference samples (c) as a function of the applied magnetic field H in the low-field part. The lines are guides for the eyes. The black ones represent the expected ferromagnetic behavior and the red lines display the behavior of the samples at annealing stages after recrystallization ($>$ 220°C).

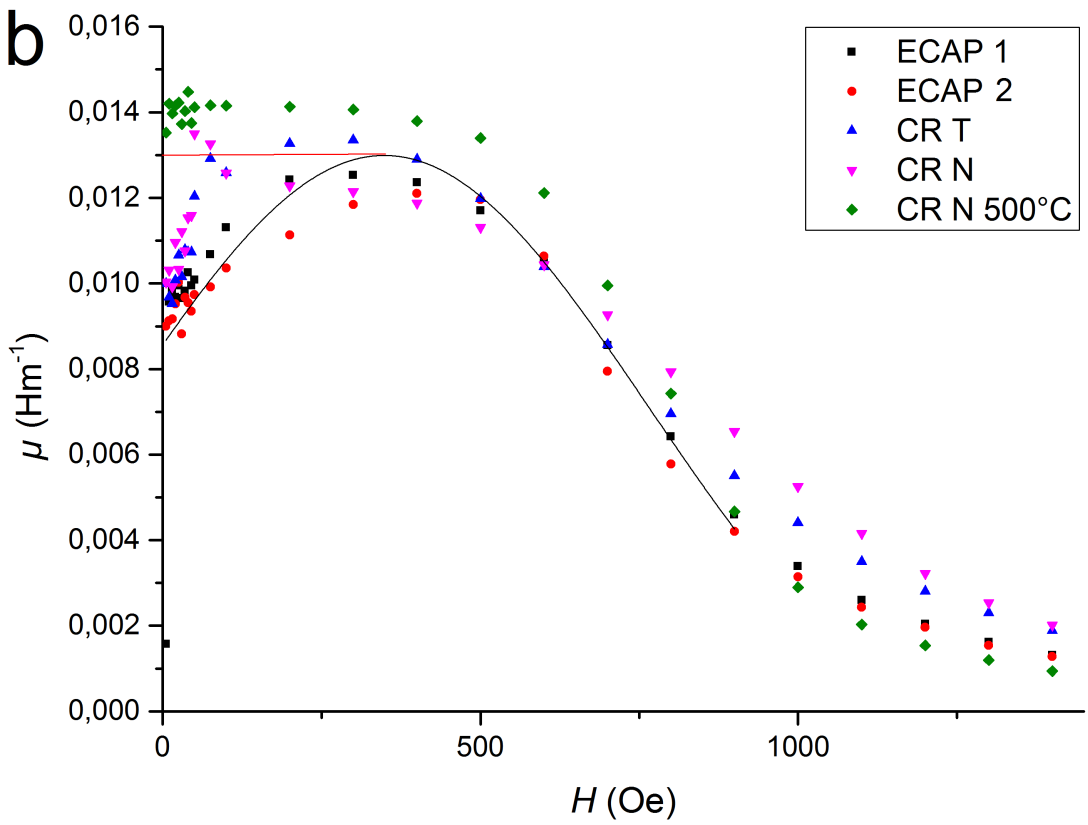
b
ECAP 1
ECAP 2
CR T
CR N
CR N 500°C
μ (Hm-1)
H (Oe)
0,000
0,002
0,004
0,006
0,008
0,010
0,012
0,014
0,016
0
500
1000

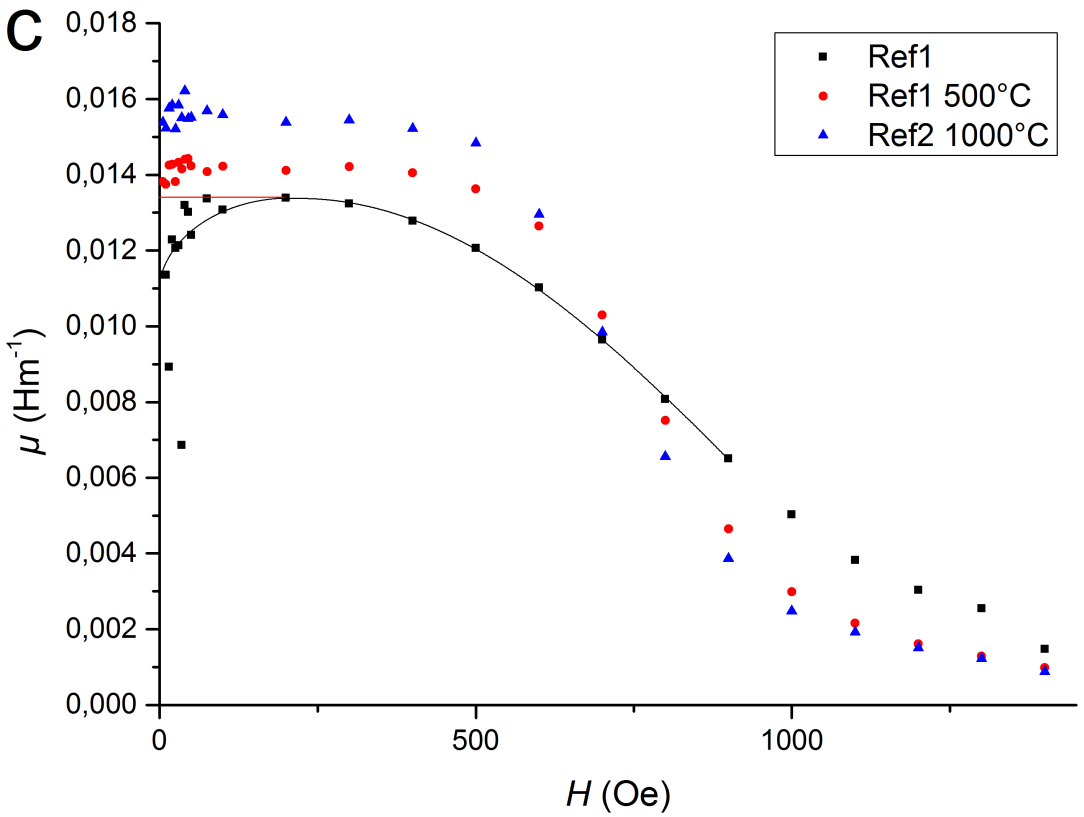
c
Ref1
Ref1 500°C
Ref2 1000°C
μ (Hm-1)
H (Oe)
0,000
0,002
0,004
0,006
0,008
0,010
0,012
0,014
0,016
0,018
0
500
1000

The permeability is dependent on the ferromagnetic element. As our nickel samples are soft ferromagnetic the peak will be reached at very low B-fields as seen in figure 5.5(a) for the HPT7 sample at all annealing stages (for higher annealing stages it look more like a plateau than a peak).

As seen in figure 5.5(a) the permeability for the earlier annealing stages behaves like expected for a ferromagnetic element (black line). It starts by increasing from a local minimum until it reaches the peak (maximum). This implies that these virgin curves behave just like the ideal one shown in figure 2.6, where the increase in permeability increases until it reaches a turning point at the maximum and then falls of.

For the higher annealing stages (220°C and 500°C) the local minimum before the peak disappears. Different to the earlier stages there is no curvature in the virgin curve at low magnetization. This indicates that after annealing either the minimum before the peak became so small, that the resolution of our SQUID was insufficient or that the minimum completely disappears. The initial permeability for these measurements increases and the remanent magnetism almost completely vanishes (see table 4.1), indicating that the nickel becomes magnetic softer after annealing.

The permeability for ECAP and CR samples is shown in figure 5.5(b) and for the reference samples in figure 5.5(c). The ECAP samples behave similar to the HPT a.p. samples. The samples CR N and CR T have a higher slope (and higher initial permeability), reaching the maximum earlier and the annealed sample CR N 500°C shows similar behavior to HPT 500°C samples. For the reference samples roughly the same as for the CR samples can be observed. While Ref1 shows a clear local minimum before the maximum, the annealed samples don't.

This leads to the conclusion that severe deformation processes (HPT and ECAP) decrease the initial permeability and therefore hinder the Bloch wall movement. While there was hardly a difference between the CR and the reference samples, after annealing the initial permeability increases, no matter how/whether the samples were deformed. All annealed samples show easy Bloch wall movement as the initial permeability increases. It falls of at around the same field as the as prepared samples (indicating that most Bloch wall movement is completed).

5.5. Medium-field area, Area II

As mentioned above, this area is $1000 - 4000$ Oe. In this area the magnetization changes mainly due to rotation of the magnetic domains [16]. This rotation is strongly influenced by the anisotropy. Therefore using equation (2.5) to fit the curves we can calculate the effective anisotropy constant using an equation from Sahar [15].

The evaluation was executed using two different approaches. First in figure 5.6 the data was fitted using equation (2.5). The obtained coefficients can be found in table 5.2 (M_s is a constant). The plots for the other samples can be found in the appendix. (figures A.1(a-d)).

The second evaluation was used by rescaling the x-axis. Instead of the applied magnetic field, the denominators of the coefficients (H^{-x}) are plotted on the x-axis (see figures 5.7(a,b) and in the appendix figures A.2-A.5). The linear fits in those plots give information about the dominant H^{-x}. To determine the quality of the linear fits the goodness of the fit was calculated. The goodness of the fit indicated, that $a_{3/2}$ and a_2 were dominant, which is why only those coefficients are plotted (figure 5.9).

The goodness of the linear fit of figures 5.7(a,b), A.2-A.5 has been calculated using the equation

$$\chi^2 = \sum \frac{(O-E)^2}{\sigma^2} \tag{5.1}$$

to determine which H^{-x} behavior is dominant. The data can be found in table 5.3. O the observed data, E the theoretical data and σ^2 the variance.

Table 5.3 shows that for the HPT and ECAP samples the χ^2-values of $H^{-1/2}$, H^{-1} and H^{-2} are magnitudes higher than for $H^{-3/2}$, indicating great deviation from the perfect linear fit. This means that for HPT and ECAP samples $H^{-3/2}$ is the dominant factor. For the CR and reference samples the χ^2-value of H^{-2} is the lowest, i.e. for those samples H^{-2} is dominant. For their annealed stages (Ref and CR N) $H^{-3/2}$ is the best fit. This shows that for all measurements of recrystallized samples ($T_a \geq 220°$C) $H^{-3/2}$ is dominant. As the theory by Kronmüller operates at higher fields, the H^{-x} behavior cannot be linked to the defects.

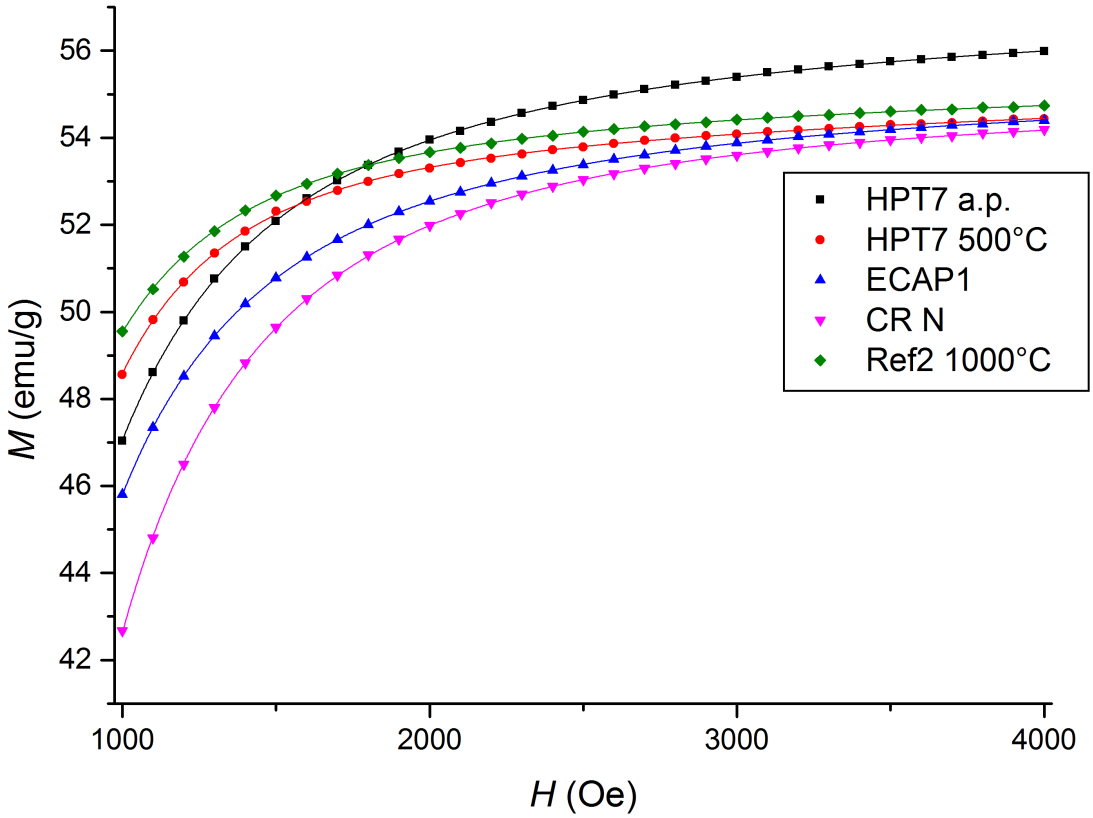

Figure 5.6.: Magnetization behavior of representative samples in the medium-field area. The data points were fitted with equation (2.5). M : specific magnetization, H : applied magnetic field.

Anisotropy constant

As seen in figure 2.5 depending on the anisotropy constant the curvature of the magnetic hysteresis changes. When adjusting the x-axis to H^{-x} the change in curvature of the virgin curve, is represented as a change in the slope of the linear fit (data in table A.1-A.4). The fitting data can be found in table A.5. In figure 5.8 the normed specific magnetization versus $H^{-3/2}$ is shown for HPT7 at different annealing stages. It can be seen that after recrystallization ($T_a \geq 220°C$) the slope strongly changes. The same can also be observed for the HPT4 sample.

The plots for the remaining samples for $H^{-3/2}$ (figures A.4(a-f)) and H^{-2} (figures A.5(a-g)), and for all samples for $H^{-1/2}$ (figures A.2(a-g)) and H^{-1} (figures A.3(a-g)) together with the tables for the fit data can be found in the appendix.

In figure 5.9 the coefficients $a_{3/2}$ and a_2, as they were dominant according to the goodness of the fit, obtained by fitting equation (2.5) to the virgin curves between 1000 Oe and 4000 Oe are shown (data in table 5.2). The plots can be found in figure 5.6

and in the appendix in figures A.1(a-d). All HPT a.p. samples have almost the same coefficients, therefore only HPT7 a.p. is plotted to represent them. HPT4 and HPT7 at different annealing stages have almost the same coefficients, therefore HPT4 was omitted.

The coefficients for HPT (before recrystallization) and ECAP samples is comparable as seen by the black point dashed line in figure 5.9(a). For $a_{3/2}$ the CR and reference samples have a greater value. After recrystallization the HPT sample has almost the same value, as seen by the red point dashed line. The CR N and the Ref1 sample also have almost the same value after annealing them to 500°C (blue point dashed line) despite differing before annealing. This value appears to further drop if the sample is annealed at higher temperatures, as seen in Ref2 1000°C.
It can therefore be concluded that $a_{3/2}$ strongly depends on the method of deformation, however after annealing the samples the differences from the method of deformation disappear.

For a_2 the value for the HPT and ECAP samples are also comparable (black point dashed line in figure 5.9(b)). After annealing the values for the HPT sample rise, compared to CR and reference samples for which the value drop. The sample Ref1, CR N and CR T are dominated by a_2 and while the value for Ref1 (red point dashed line) is the highest, the value for both CR samples is comparable (blue point dashed line). The data for a_2 is not as conclusive, as for $a_{3/2}$. While sample with the same method of deformation have comparable values for a_2, after recrystallization those values strongly vary.

The changes in $a_{3/2}$ and a_2 cannot be directly linked to the change in slope for the corresponding samples. For example comparing the slope in table A.3 and A.4 to the coefficient a_2 in table 5.2, while the slope decreases for both $H^{-3/2}$ and H^{-2} after recrystallization, the coefficient $a_{3/2}$ decreases and a_2 increases after recrystallization. This makes a direct comparison between the two evaluation methods difficult. It can be concluded that not only one coefficient is dominant and the others can be neglected, but rather all coefficients are necessary.

In [15] a method is proposed to calculate the effective anisotropy constant K_{eff} from

the coefficient a_2 (calculated in (2.5)). It is calculated using:

$$K_{eff} = \mu_0 M_s \cdot (105 a_2/8)^{1/2} \tag{5.2}$$

Using the coefficients from table 5.2, the values for K_{eff} were calculated (see table 5.4). The literature value for K_{eff} is $5.4 \cdot 10^4\ erg/cm^3$ for polycrystalline nickel. [24]

All our values are higher than the literature value, which could be either due to the fact that the literature value is for polycrystalline nickel and we have deformed nickel samples.

The results using equation (5.2) are questionable, as for the HPT samples K_{eff} increases with annealing, while for the CR and reference samples K_{eff} decreases. The interpretation for this data could be as follows: SPD strongly decreases the anisotropy constant compared to cold rolled or reference sample. After annealing the anisotropy constant increases for SPD samples, while it decreases for the other samples to a comparable value. The increase in K_{eff} with T_a for the HPT samples could indicate, that in the as prepared state the crystal anisotropy is not dominant for the rotation, but the internal stress gives a contribution. It is unknown which H^{-x} dependence the internal stress has and it might not be H^{-2}. Another factor is that the $a_{3/2}/H^{3/2}$ term in our fitting equation is not used by Sahar. For our measurements $H^{-3/2}$ is the dominant term, therefore it could be that equation (5.2) is not applicable if H^{-2} is not dominant. In table 5.4 the error of K_{eff} is between 13% and 46%, indicating that it is not possible to make a credible statement regarding the effective anisotropy constant using a_2.

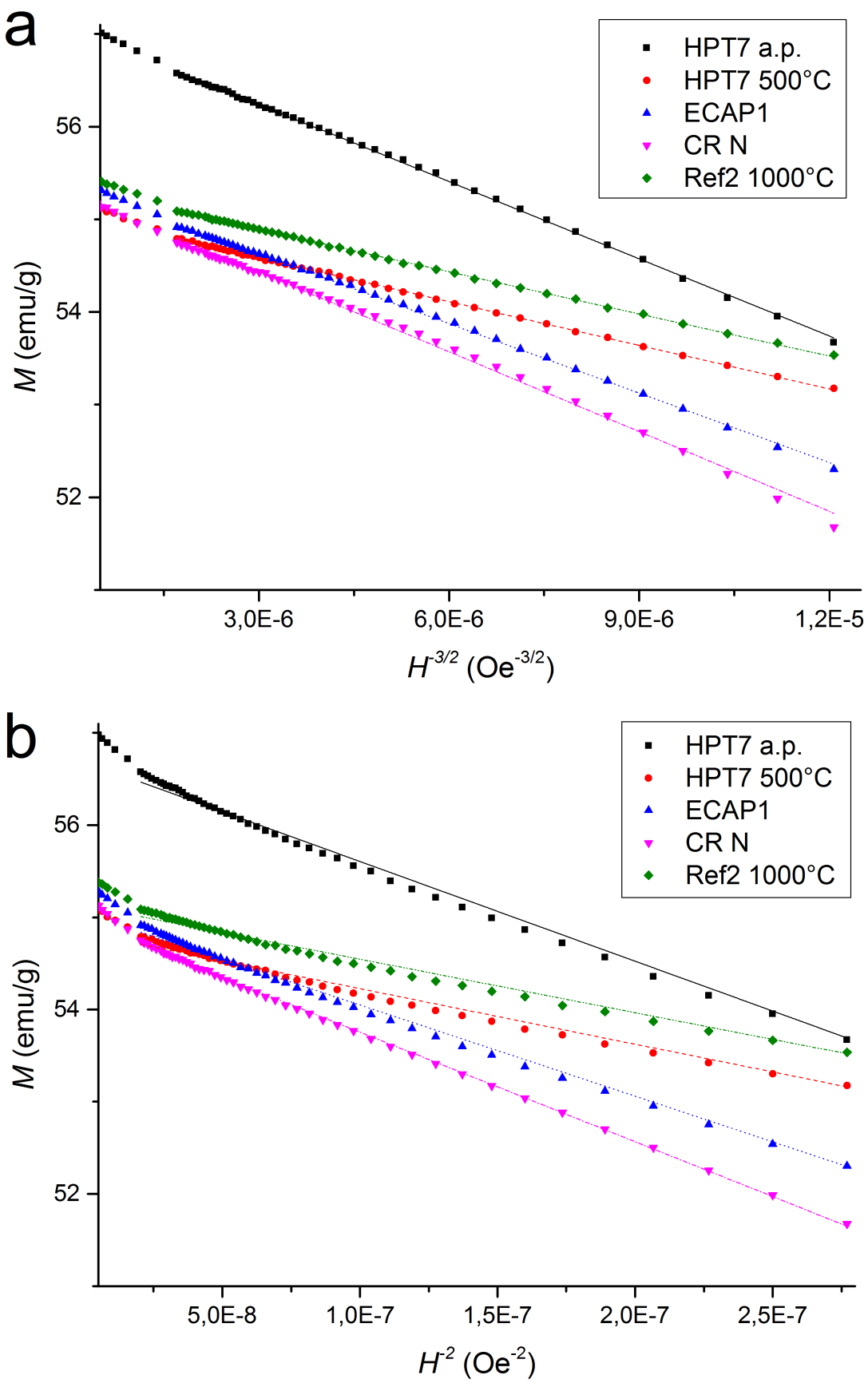

Figure 5.7.: Plots according to (a) the $H^{-3/2}$ and in (b) the H^{-2} behavior for the medium-field range. A linear fit has been added for both figures. All data points are from the virgin curves. M : specific magnetization, H : applied magnetic field.

Table 5.2.: Parameters of the fitted curves according to equation 2.5 in the medium-field range $1000 - 4000$ Oe. (cf. figures 5.6, A.1(a-d)

Sample	$a_{1/2}/(emu/g)^{-3/2}$	$a_1/(emu/g)^{-2}$	$a_{3/2}/(emu/g)^{-5/2}$	$a_2/(emu/g)^{-3}$
HPT2 a.p.	1.21 ± 0.10	12.1 ± 2.7	7564 ± 177	164565 ± 3674
HPT3 a.p.	1.22 ± 0.09	13.2 ± 4.2	8367 ± 183	152445 ± 2764
HPT6 a.p.	1.24 ± 0.07	14.1 ± 5.0	8653 ± 160	165678 ± 4576
HPT4 a.p.	1.43 ± 0.06	15.5 ± 6.8	9234 ± 143	160986 ± 3809
HPT4 100°C	1.40 ± 0.07	16.4 ± 6.1	8865 ± 150	156546 ± 4231
HPT4 160°C	1.20 ± 0.07	17.4 ± 2.1	8546 ± 158	165687 ± 3764
HPT4 220°C	1.55 ± 0.07	17.2 ± 3.3	7686 ± 157	190974 ± 5126
HPT4 500°C	1.30 ± 0.10	14.2 ± 2.9	6987 ± 267	200968 ± 5121
HPT7 a.p.	1.27 ± 0.06	14.0 ± 3.5	8762 ± 142	156464 ± 5132
HPT7 100°C	1.04 ± 0.08	12.4 ± 3.3	8453 ± 168	160847 ± 6231
HPT7 160°C	1.34 ± 0.07	14.2 ± 2.2	8125 ± 154	155454 ± 5091
HPT7 220°C	1.54 ± 0.11	16.3 ± 5.7	7765 ± 215	190857 ± 6345
HPT7 500°C	1.76 ± 0.16	17.7 ± 3.7	7521 ± 311	219865 ± 4312
HPT7 500°C $\perp$	97.13 ± 3.51	335.2 ± 31.7	54524 ± 5324	249857 ± 15451
ECAP1	1.52 ± 0.07	17.3 ± 3.8	9756 ± 144	169876 ± 3164
ECAP2	1.17 ± 0.03	13.1 ± 3.0	8723 ± 99	160986 ± 34534
CR T	1.61 ± 0.03	21.8 ± 3.3	13243 ± 78	243234 ± 13453
CR N	2.91 ± 0.22	39.5 ± 8.2	15643 ± 285	232435 ± 12986
CR N 500°C	0.68 ± 0.18	13.9 ± 3.3	6832 ± 349	195675 ± 5987
Ref1	2.71 ± 0.19	32.5 ± 6.1	14459 ± 364	293211 ± 4454
Ref1 500°C	0.51 ± 0.15	12.9 ± 2.7	6656 ± 356	205424 ± 3343
Ref2 1000°C	0.33 ± 0.13	5.23 ± 1.1	5875 ± 275	153245 ± 4153

Table 5.3.: χ^2 for the linear fits according to H^{-x} in the medium-field range $1000 - 4000\,\mathrm{Oe}$. (cf. figures 5.7(a,b), A.2-A.5

Sample	$H^{-1/2}$	H^{-1}	$H^{-3/2}$	H^{-2}
HPT2 a.p.	1.452	0.432	0.006	0.097
HPT3 a.p.	2.394	0.708	0.018	0.280
HPT6 a.p.	2.394	0.722	0.011	0.239
HPT4 a.p.	2.748	0.930	0.029	0.140
HPT4 100°C	2.639	0.850	0.016	0.186
HPT4 160°C	2.537	0.777	0.009	0.236
HPT4 220°C	1.474	0.515	0.016	0.063
HPT4 500°C	0.773	0.199	0.014	0.183
HPT7 a.p.	3.032	0.943	0.049	0.259
HPT7 100°C	2.810	0.854	0.044	0.291
HPT7 160°C	2.513	0.795	0.048	0.197
HPT7 220°C	1.217	0.381	0.025	0.110
HPT7 500°C	0.780	0.206	0.006	0.145
HPT7 500°C $\perp$	40.152	24.323	12.868	5.535
ECAP1	2.844	0.971	0.038	0.135
ECAP2	2.896	0.980	0.041	0.145
CR T	5.634	2.249	0.200	0.040
CR N	5.566	2.350	0.213	0.019
CR N 500°C	0.825	0.225	0.013	0.152
Ref1	3.915	1.547	0.094	0.073
Ref1 500°C	0.871	0.228	0.009	0.175
Ref2 1000°C	0.694	0.179	0.007	0.146

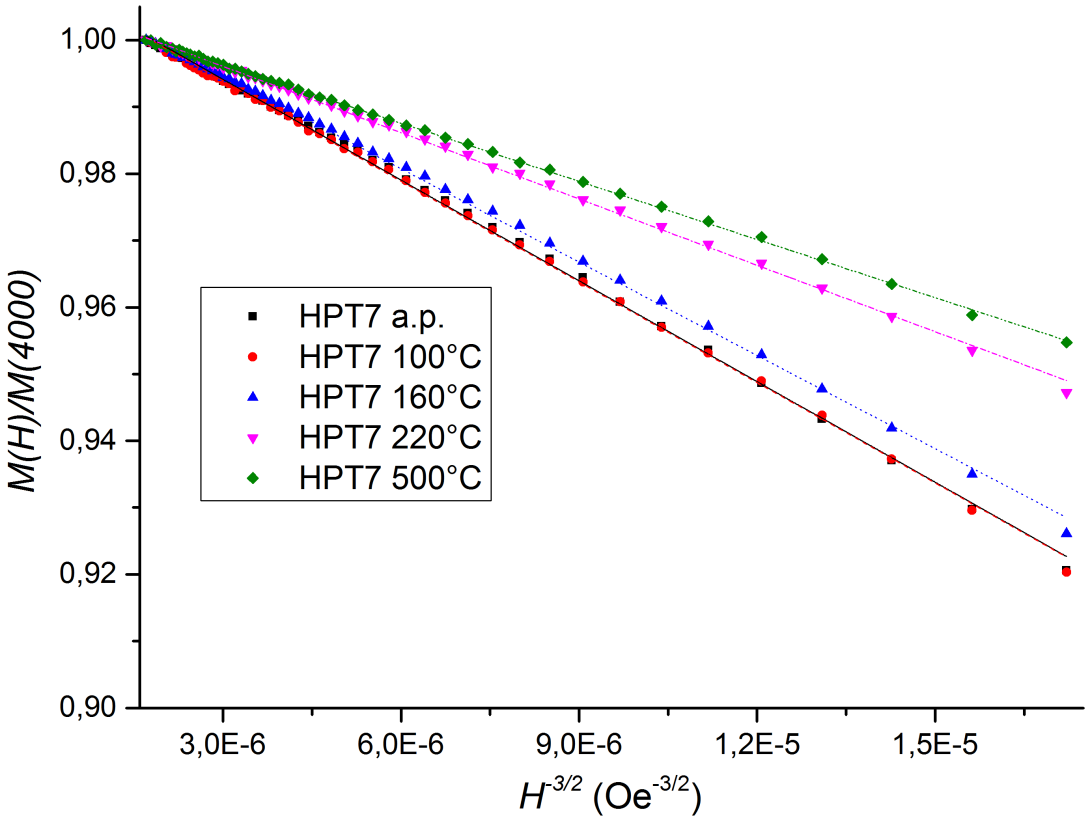

Figure 5.8.: Normalized specific magnetization versus $1/H^{3/2}$ for HPT7 at different annealing stages. Fit data see table A.5

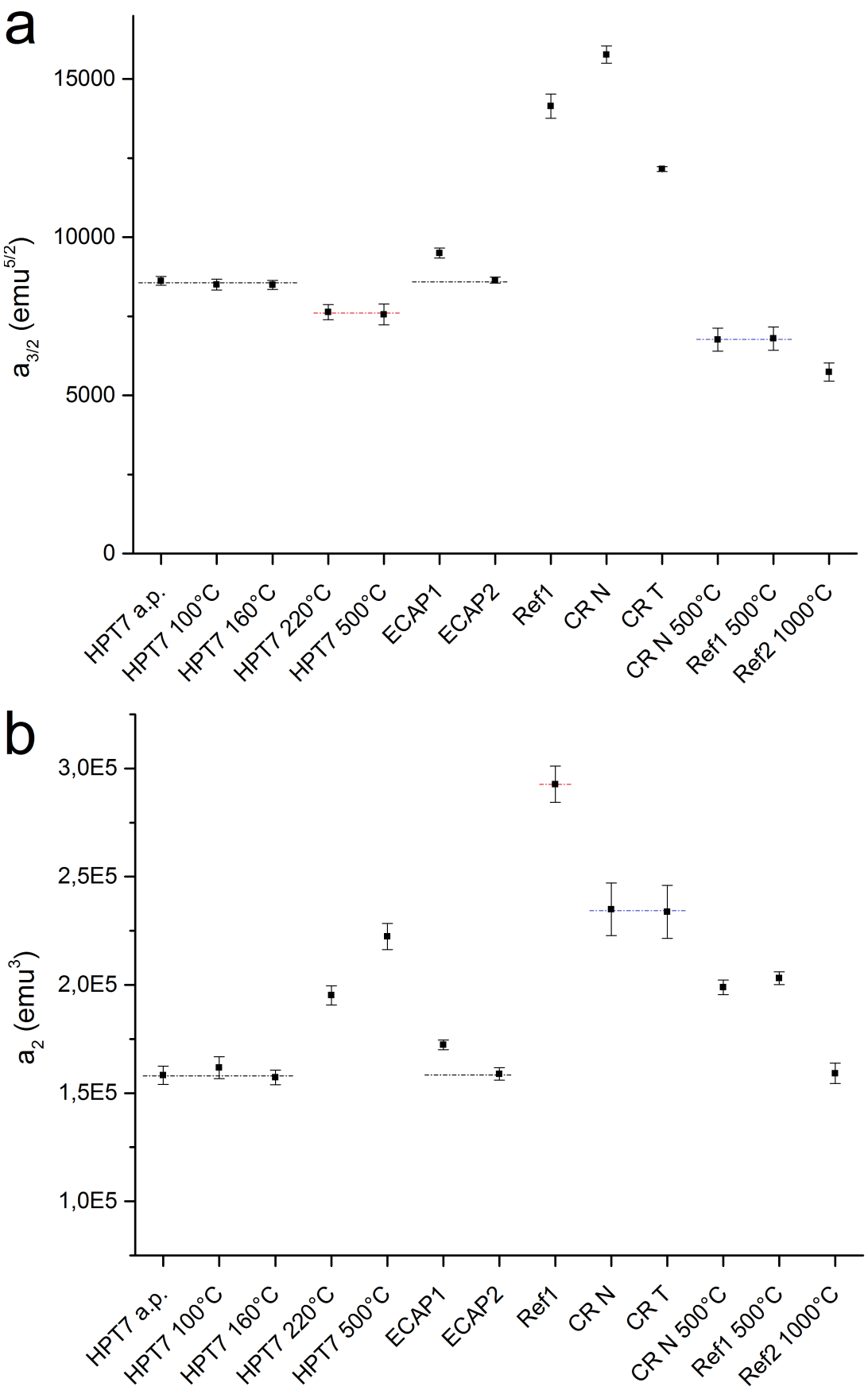

Figure 5.9.: Coefficients $a_{3/2}$ and a_2 obtained by fitting equation (2.5) to the data shown in figure 5.6.

Table 5.4.: Effective anisotropy constant calculated with equation (5.2) for all samples using a_2 from table 5.2

Sample	$K_{eff}(erg/cm^3)$
HPT2 a.p.	82301 ± 12297
HPT3 a.p.	79213 ± 10666
HPT6 a.p.	82579 ± 13724
HPT4 a.p.	81401 ± 12521
HPT4 100°C	80271 ± 13197
HPT4 160°C	82581 ± 12447
HPT4 220°C	88659 ± 14525
HPT4 500°C	90950 ± 14518
HPT7 a.p.	80250 ± 14534
HPT7 100°C	81366 ± 16015
HPT7 160°C	79991 ± 14476
HPT7 220°C	88632 ± 16160
HPT7 500°C	95130 ± 13322
HPT7 500°C $\perp$	101411 ± 25218
ECAP1	83619 ± 11412
ECAP2	81401 ± 37702
CR T	100058 ± 23531
CR N	97811 ± 23119
CR N 500°C	89744 ± 15698
Ref1	109857 ± 13540
Ref1 500°C	91952 ± 11730
Ref2 1000°C	79420 ± 13074

5.6. High-field area, Area III

This area is between 10000 Oe and 40000 Oe. In this area the increase in magnetization is mainly due to the defects, which suppress spin alignment.

Same as in section 5.5 the evaluation was executed with two approaches. Figures 5.10(a) and A.6 were fitted with equation (2.3). In figure 5.10(a) only the data points are shown which were used for the fit. Data points were omitted in the fit either due to the points being a measurement error or because the para effect already predominated in this area; for HPT8 500°C this is above 30000 Oe (see figure 5.10(b), between 5 $\mathrm{mOe}^{-1/2}$ and 6 $\mathrm{mOe}^{-1/2}$ where the slope of magnetization increases in the $H^{-1/2}$-plot). However the para effect in equation (2.3) was necessary in the fit because otherwise the slope would almost completly disappear at $\sim$ 20000 Oe, which is not the case in the data points. For the fit the data point at 17500 Oe for HPT8 500°C was omitted. The coefficients for the fit can be found in table 5.5.

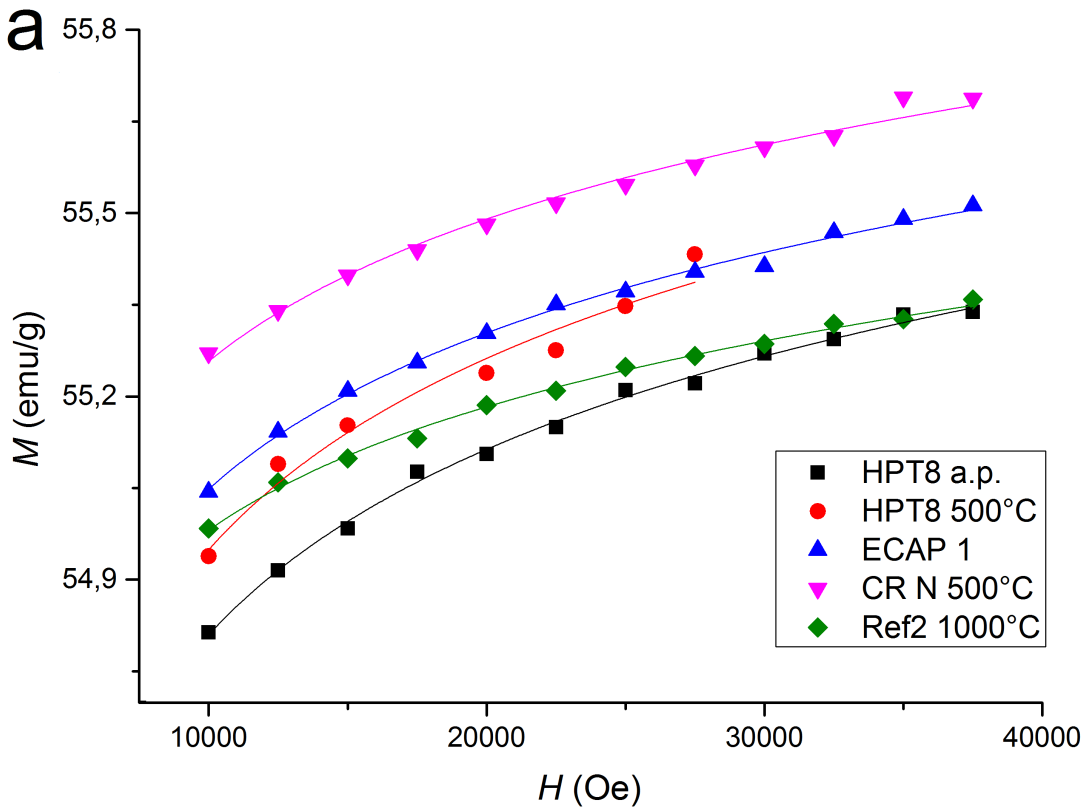

Figure 5.10.: Magnetization behavior of representative samples in the high-field part. Figure (a) shows the data points fitted with equation (2.3). In figure (b) the x-axis was rescaled to $H^{-1/2}$ and a linear fit has been added. In Figure (c) the coefficient $a_{1/2}$ was obtained by fitting equation (2.3) to the data of figure (a). The point-dashed lines in (c) indicate the samples which show the same behavior. All data points are from the virgin curves. M : specific magnetization, H : applied magnetic field.

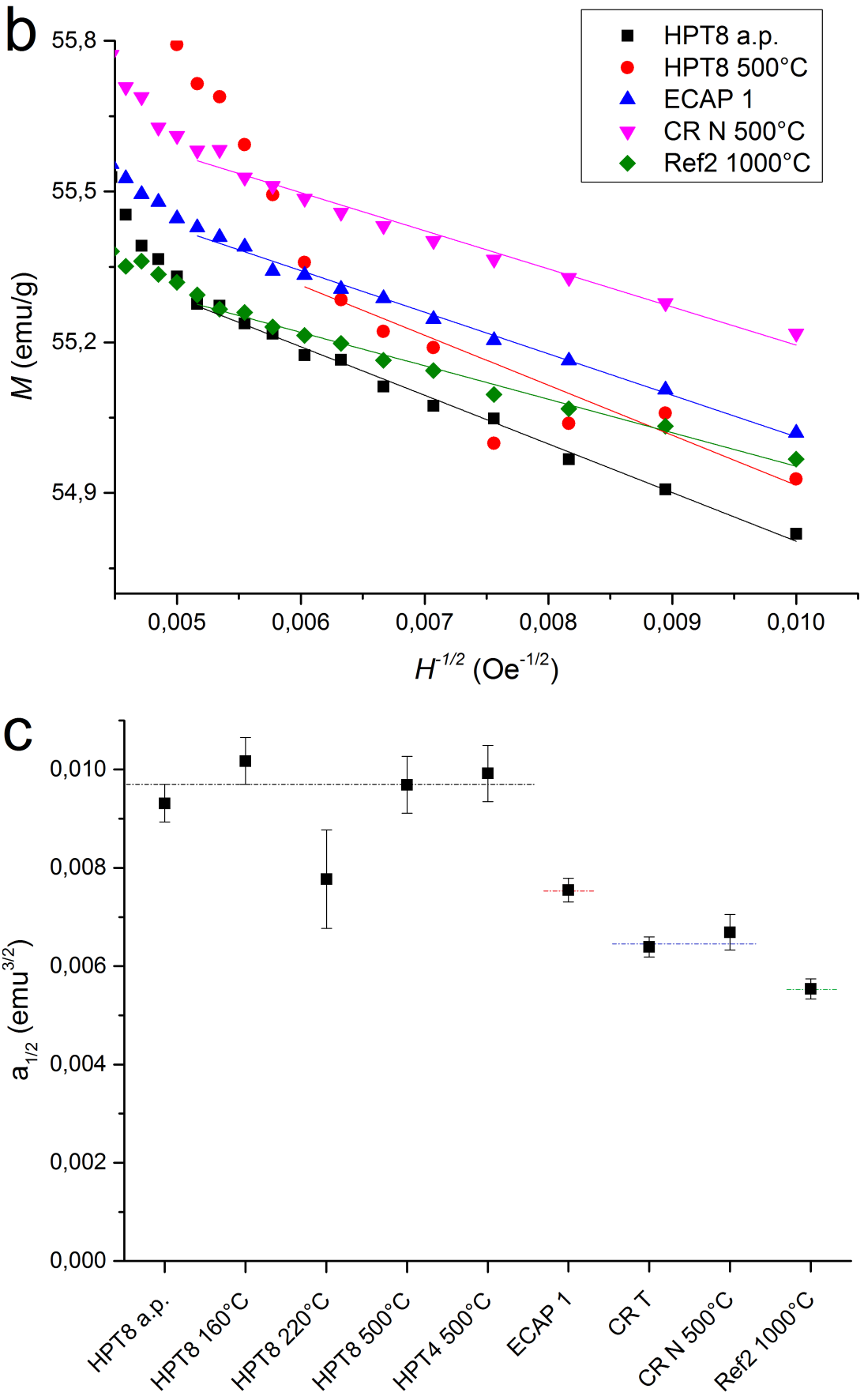

The values in table 5.5 have been converted into T (Tesla) in order to compare them with the values from Kisker.

Table 5.5.: Parameters of the fitted curves according to equation (2.3) in emu/g and in *Tesla*.

Sample	$a_{1/2}\ (emu/g)^{-3/2}$	$M_s\ (emu/g)$	$a_{1/2}\ /10^{-3}(T)^{-3/2}$	$M_s\ (10^{-3})\ T$
HPT8 a.p.	0.82 ± 0.05	56.01 ± 0.79	9.31 ± 0.27	692.8 ± 0.2
HPT8 160°C	0.90 ± 0.18	55.66 ± 0.53	10.17 ± 0.48	697.9 ± 0.3
HPT8 220°C	0.62 ± 0.41	56.15 ± 0.85	7.89 ± 1.17	695.5 ± 0.5
HPT8 500°C	0.86 ± 0.02	55.85 ± 0.76	9.69 ± 0.58	694.7 ± 1.0
HPT4 500°C	0.87 ± 0.17	56.83 ± 1.78	9.92 ± 0.57	700.7 ± 0.7
ECAP1	0.56 ± 0.20	55.73 ± 2.11	7.55 ± 0.24	693.6 ± 0.2
CR T	0.53 ± 0.15	55.73 ± 0.46	6.39 ± 0.19	697.5 ± 0.1
CR N 500°C	0.54 ± 0.12	56.06 ± 0.47	6.69 ± 0.36	695.1 ± 0.3
Ref2 1000°C	0.48 ± 0.05	55.83 ± 1.00	5.54 ± 0.20	692.9 ± 0.1

The fitting algorithm first tried to fit the curve with one coefficient (e.q. $a_{1/2}$) and then proceeded to find good values for the other coefficients. This however failed, as a_1, $a_{3/2}$ and a_2 failed to converge. Their values were less than 10^{-18} in some cases and had an several times bigger error. Therefore, these values have been omitted in table 5.5.

The second evaluation method was same as in section 5.5 by rescaling the x-axis, performing a linear fit and calculating the goodness of the fit (see figure 5.10(b) the x-axis is $H^{-1/2}$). Figure A.7 for the other samples can be found in the appendix. As seen in table 5.6 and figure A.8, the χ^2-values for $a_{1/2}$ are always the lowest, indicating the best fit.

In figure 5.10(c) the $a_{1/2}$ coefficient is plotted and point dashed lines have been added. These lines show, that differently prepared samples have roughly the same values. The deviation for HPT8 220°C may be due to an error in measurement.
Compared to area II (figure 5.9(b)) the behavior is quite different. While in area II a big change in the coefficients occurred between annealed and not annealed samples (see CR), in area III (figure 5.10(c)) only samples of different processing type show clearly different behavior. Compared to area II, the values for $a_{1/2}$ and χ^2 differ substantially between HPT and ECAP samples in area III. This leads to the conclusion, that the annealing (which makes a ferromagnet softer) strongly influences the rotation of magnetization (regime II), while it has hardly any effect on agglomerations of voids

Table 5.6.: χ^2 for the linear fits according to H^{-x} in high-field range (cf. figures 5.10(b) and A.7)

Sample	$H^{-1/2}$	H^{-1}	$H^{-3/2}$	H^{-2}
HPT8 a.p.	4.69	9.52	15.61	22.68
HPT8 160°C	0.15	0.44	1.37	2.81
HPT8 220°C	1.52	9.84	21.01	35.09
HPT8 500°C	5.05	20.02	36.52	55.55
HPT4 500°C	7.24	19.25	31.13	44.11
ECAP1	1.68	6.13	13.64	23.32
CR T	2.57	7.04	13.97	22.44
CR N 500°C	4.40	10.79	19.58	29.70
Ref2 1000°C	2.29	6.51	12.65	20.02

($a_{1/2}$) (regime III).

The scattering for the values of M_s are within 1.1% (table 5.5). The value Kisker [10] obtained for M_s is 0.664 T which is slightly lower than the 0.693 T for HPT8 (see table 5.5).

The values for $a_{1/2}$ (table 5.5) and the slopes for figure 5.10(b) are listed side by side in table 5.7. In area III only the coefficient $a_{1/2}$ has a meaningful value, therefore a correlation between the slope of the linear fit and the coefficient $a_{1/2}$ can be seen.

Calculation of void radius r_0

Kisker uses the coefficient $a_{1/2}$ for nonmagnetic enclosures (holes). His values are $\sim 1.9 \cdot 10^{-2}\,\mathrm{T}^{3/2}$, converting the values for HPT8 in $\mathrm{T}^{3/2}$ the obtained value of the HPT8 500°C is $\sim 1.0 \cdot 10^{-2}\,\mathrm{T}^{3/2}$, which is lower, but still in the same magnitude as Kiskers. Using the following equation from Kisker

$$a_{1/2} = \frac{\sqrt{2}\pi^2 M_s^{5/2}}{27\mu_0^{1/2} A_{ex}^{1/2}} r_0^4 N \tag{5.3}$$

with our values for $a_{1/2}$, it is possible to calculate $r_0^4 N$. In equation (5.3) A_{ex} is the exchange constant, r_0 the average radius of the holes and N the number density of holes. As N is unknown for our material, it is not possible to calculate r_0 directly.

Table 5.7.: Coefficient $a_{1/2}$ of the fitted curves according to equation (2.3) and slope from the linear fits

Sample	$a_{1/2}\ (emu/g)^{-3/2}$	Slope
HPT8 a.p.	0.82 ± 0.05	-96.8 ± 2.4
HPT8 160°C	0.90 ± 0.18	-103.7 ± 4.4
HPT8 220°C	0.62 ± 0.41	-80.4 ± 5.3
HPT8 500°C	0.86 ± 0.02	-99.6 ± 11.3
HPT4 500°C	0.87 ± 0.17	-99.0 ± 6.4
ECAP1	0.56 ± 0.20	-82.7 ± 2.3
CR T	0.53 ± 0.15	-73.4 ± 1.8
CR N 500°C	0.54 ± 0.12	-75.8 ± 3.5
Ref2 1000°C	0.48 ± 0.05	-66.7 ± 2.3

In Kisker's work the exchange length $l_{ex} = 55\,\text{nm}$ is used to calculate a maximum value for N, i.e. N_{max}.

$$N_{max} = \frac{3}{4\pi}\frac{1}{l_{ex}^3} \tag{5.4}$$

The inverse of the exchange volume $\frac{4\pi}{3}l_{ex}^3$ defines the maximum number density N_{max} which is compatible with the model that underlies equation (5.3). Using $A_{ex} = 3.5 \cdot 10^{-16}\,\text{J/m}$ Kisker calculates a value for the radius $r_{0,min} = 6.5\,\text{nm}$.

Using our values, summarized in table 5.5 (A_{ex} and l_{ex} are the same as Kiskers), the minimum radius for our samples can be calculated (see table 5.8). A reason why the values are smaller could be because Kisker uses a granular crystalline nickel sample and measures at $T = -268\,^{\circ}\text{C}$, while we use HPT nickel sample and measure at $T = 27\,^{\circ}\text{C}$. The different measurement temperature may influence the curvature of the hysteresis and therefore $a_{1/2}$. [10]

Table 5.8.: Minimum radius calculated using equation (5.3) and the values from table 5.6

Sample	$r_{0,min}\ nm$
HPT8 a.p.	5.08
HPT8 160°C	5.19
HPT8 220°C	4.87
HPT8 500°C	5.13
HPT4 500°C	5.16
ECAP1	4.82
CR T	4.62
CR N 500°C	4.71
Ref2 1000°C	4.46

6. Conclusion

In this master thesis the magnetic hysteresis behavior for differently processed nickel samples was studied with a SQUID magnetometer. The analyzed samples were deformed using HPT and ECAP, with and without temperature annealing. Additionally, the comparison to cold rolling and reference samples was examined.

Tests prior to the measurement sequences showed that the cutting process and the sample orientation, with respect to the deformation axis, do not effect the magnetic measurements. However, the mounting of the sample in the sample holder strongly influenced the curvature of the virgin curve.

For the coercivity of the HPT- and ECAP-samples the following conclusions were made:

- The HPT ($T_a \leq 160°C$) and ECAP samples are characterized by an enhanced coercivity (figure 5.2)
- After recrystallization ($T_a \geq 220°C$) the coercivity strongly decreased, i.e., the samples became magnetic softer (figure 5.3)
- The cold-rolled and the reference samples had a lower coercivity than the HPT and ECAP samples, which further decreased after annealing (table 5.1)

By means of analysis of the virgin curve three H-field areas could be identified, in which different effects dominate.

Low-field area

- The low-field part is dominated by Bloch wall movement
- The HPT samples showed an increase in initial permeability $\mu(H = 0)$ after annealing with $T_a \geq 220°C$. This is considered as further indication that the samples get magnetic softer after recrystallization (figure 5.5)

Medium-field area

- The medium-field part is dominated by rotation of domain magnetization
- This area is best fitted by a $H^{-3/2}$-dependence except for the cold rolling samples where H^{-2} dominated (table 5.3)
- The absolute values of slopes of the M-$H^{-3/2}$ plots for the HPT- ($T_a \leq 160°C$), ECAP- and CR-samples are distinctly higher than for the recrystallized HPT and the reference samples (figure 5.7). The higher slope indicates a more sluggish approach to magnetic saturation.
- Both the M-H-behavior (figure 5.6) and the slope of the M-H^{-x}-plots (figure 5.7) indicate that HPT-Ni gets magnetically softer upon annealing

High-field area

- The high-field area is dominated by the alignment of spins adjacent to lattice defects
- This area is best fitted by a $H^{-1/2}$ dependence. $-\frac{1}{2}$ is also the single dominant exponent found in the multiexponent fit. Therefore the prefactor $a_{1/2}$ of the analysis is directly correlated with the slope of the M-$H^{-1/2}$-plot (table 5.7)
- The absolute values of slopes of the M-$H^{-1/2}$ plots for the HPT- and ECAP-samples were distinctly higher than for the reference sample (figure 5.10(b))
- The values for $a_{1/2}$ for HPT were higher than for the cold-rolled and reference samples (figure 5.10(c))
- According to the theory of Kronmüller the $H^{-1/2}$-behavior in the saturation regime is due to non-magnetic spherical defects. Presumably these are nanovoids in the Ni sample

- Both the $a_{1/2}$-value and the slope of the M-H$^{-1/2}$-plot indicate a higher concentration or larger size of nanovoids in HPT- and ECAP-processed Ni compared to the reference sample

Appendix A.

List of Figures

In the appendix several additional figures are shown.

In figure A.1 the virgin curves in the medium-field area are plotted.

In figures A.2(a-g) the different samples are plotted versus $H^{-1/2}$. The data from the linear fits can be found in table A.1 and for the normed figure in table A.5.

In figures A.3(a-g) the different samples are plotted versus H^{-1}. The data from the linear fits can be found in table A.2 and for the normed figure in table A.5.

In figures A.4(a-f) the different samples are plotted versus $H^{-3/2}$. The data from the linear fits can be found in table A.3. The normed figure 5.8 can be found in section 5.5.

In figures A.5(a-g) the different samples are plotted versus H^{-2}. The data from the linear fits can be found in table A.4 and for the normed figure in table A.5.

In figure A.6 the samples HPT4 500°C, HPT8 160°C, HPT 220°C and CR T are plotted versus the applied magnetic field and in figure A.7 they are plotted versus $H^{-1/2}$ in the high-field region. Additionally in figure A.8 the values χ^2 for all samples in the high-field area are plotted.

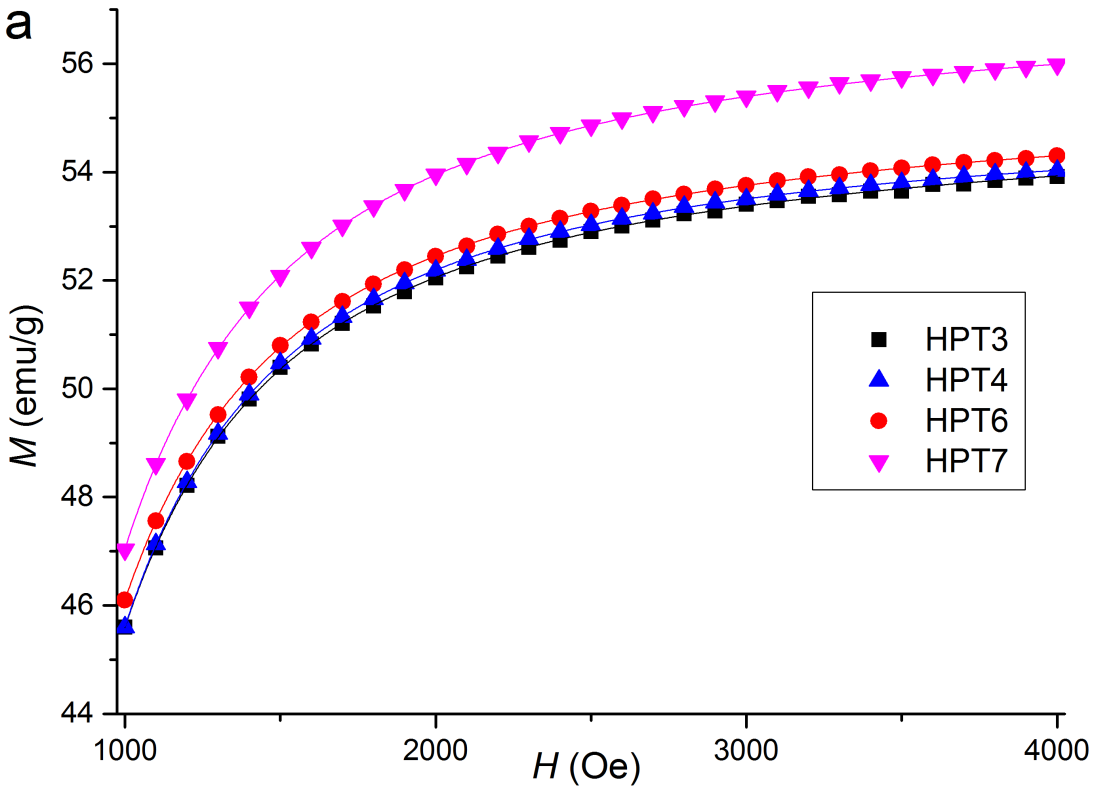
a
56
54
52
50
48
46
44
M (emu/g)
1000
2000
3000
4000
H (Oe)
HPT3
HPT4
HPT6
HPT7

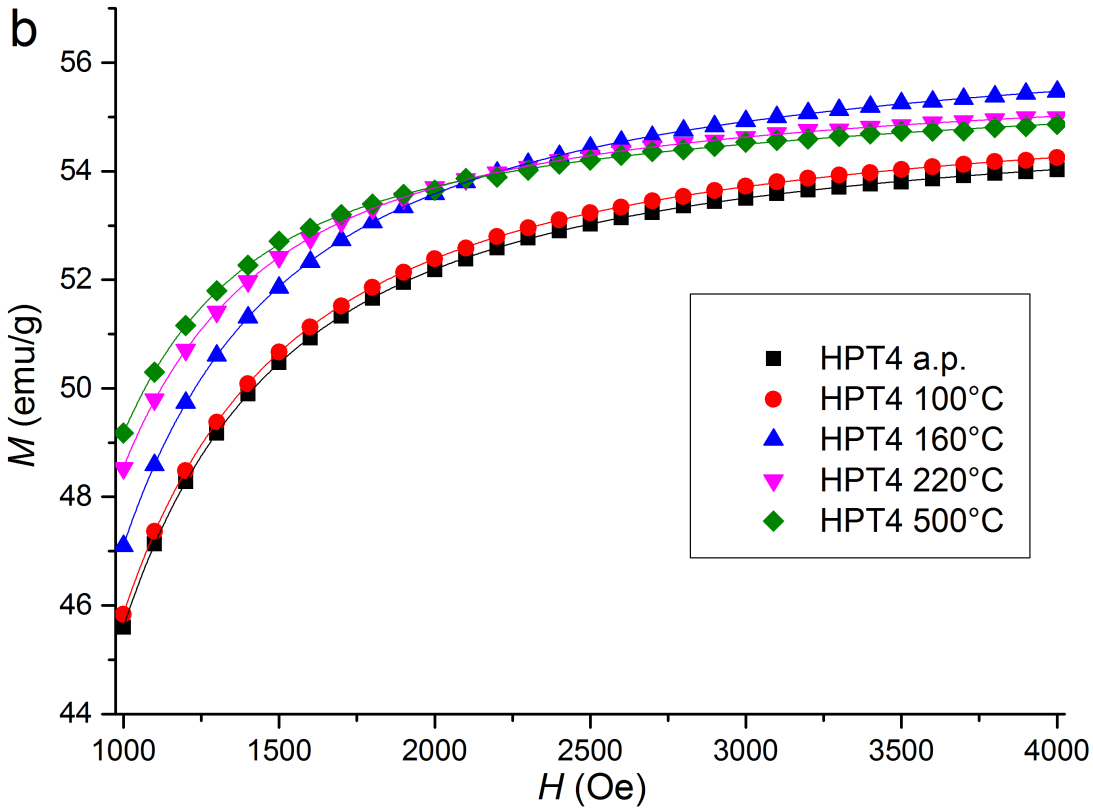
b
56
54
52
50
48
46
44
M (emu/g)
1000
1500
2000
2500
3000
3500
4000
H (Oe)
HPT4 a.p.
HPT4 100°C
HPT4 160°C
HPT4 220°C
HPT4 500°C

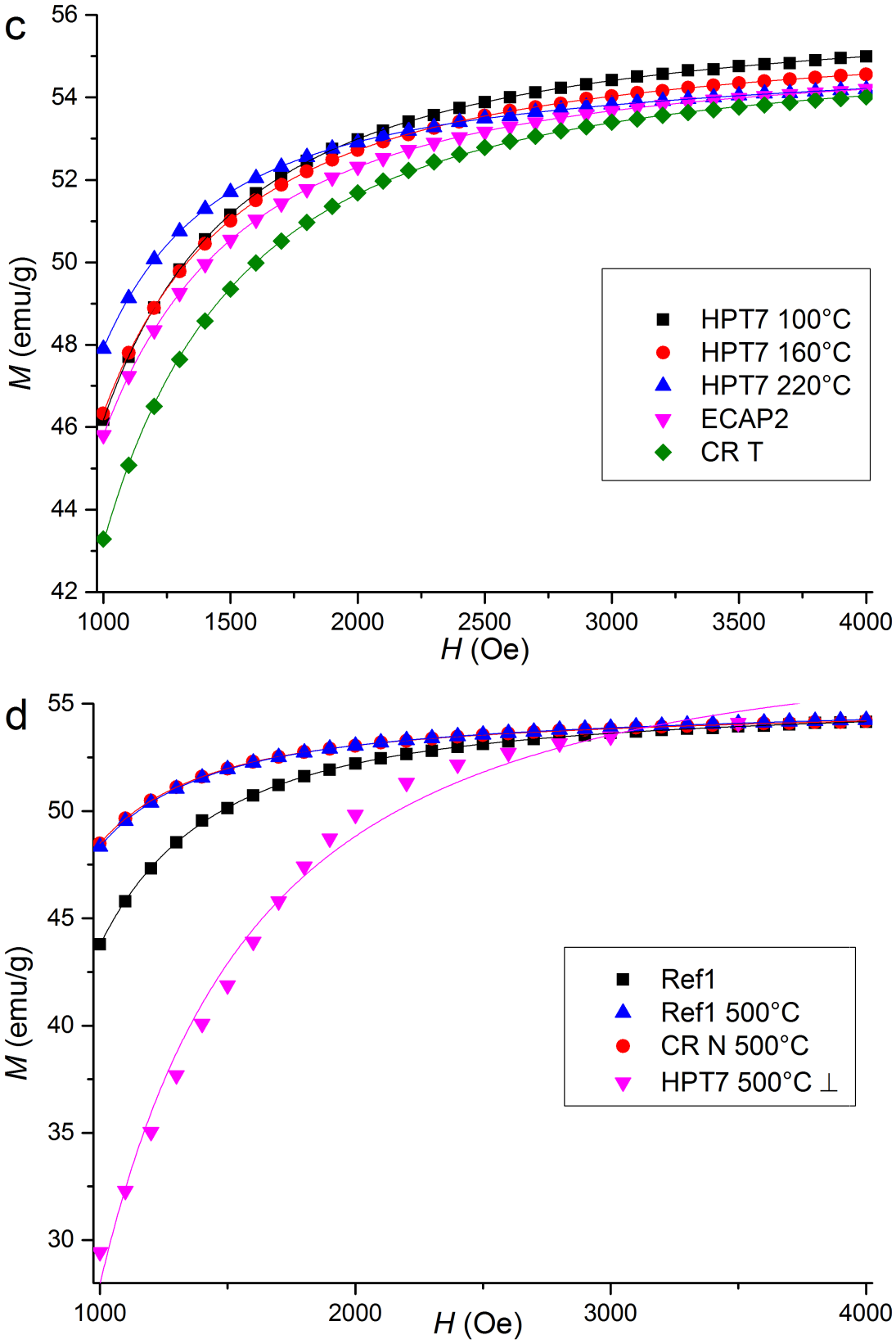

Figure A.1.: Specific magnetization M versus applied field H for the medium-field region. Fitted with equation 2.5

Table A.1.: Parameters of the fitted curves for $1/H^{1/2}$ (Slope$\times x$ + Intercept)

Sample	Intercept	Slope
HPT2 a.p.	59.49 ± 0.24	-276.76 ± 12.56
HPT3 a.p.	57.99 ± 0.14	-265.66 ± 8.43
HPT4 a.p.	58.00 ± 0.16	-260.32 ± 9.03
HPT4 100°C	58.29 ± 0.15	-264.32 ± 8.85
HPT4 160°C	59.55 ± 0.15	-267.31 ± 8.68
HPT4 220°C	57.87 ± 0.11	-187.33 ± 6.61
HPT4 500°C	57.40 ± 0.08	-165.71 ± 4.79
HPT6 a.p.	58.29 ± 0.14	-261.63 ± 8.43
HPT7 a.p.	60.40 ± 0.16	-289.20 ± 9.48
HPT7 100°C	59.33 ± 0.16	-283.97 ± 9.13
HPT7 160°C	58.54 ± 0.15	-260.83 ± 8.64
HPT7 220°C	57.01 ± 0.10	-183.76 ± 6.01
HPT7 500°C	56.92 ± 0.08	-162.33 ± 4.81
HPT7 500°C $\perp$	69.90 ± 2.63	-958.13 ± 126.41
ECAP1	58.43 ± 0.16	-263.87 ± 9.19
ECAP2	58.29 ± 0.16	-267.41 ± 9.27
CR T	59.02 ± 0.22	-329.17 ± 12.93
CR N	58.95 ± 0.22	-313.24 ± 12.85
CR N 500°C	56.73 ± 0.08	-165.70 ± 4.95
Ref1	58.46 ± 0.19	-281.69 ± 10.78
Ref1 500°C	56.92 ± 0.09	-173.80 ± 5.08
Ref2 1000°C	57.14 ± 0.08	-156.19 ± 4.54

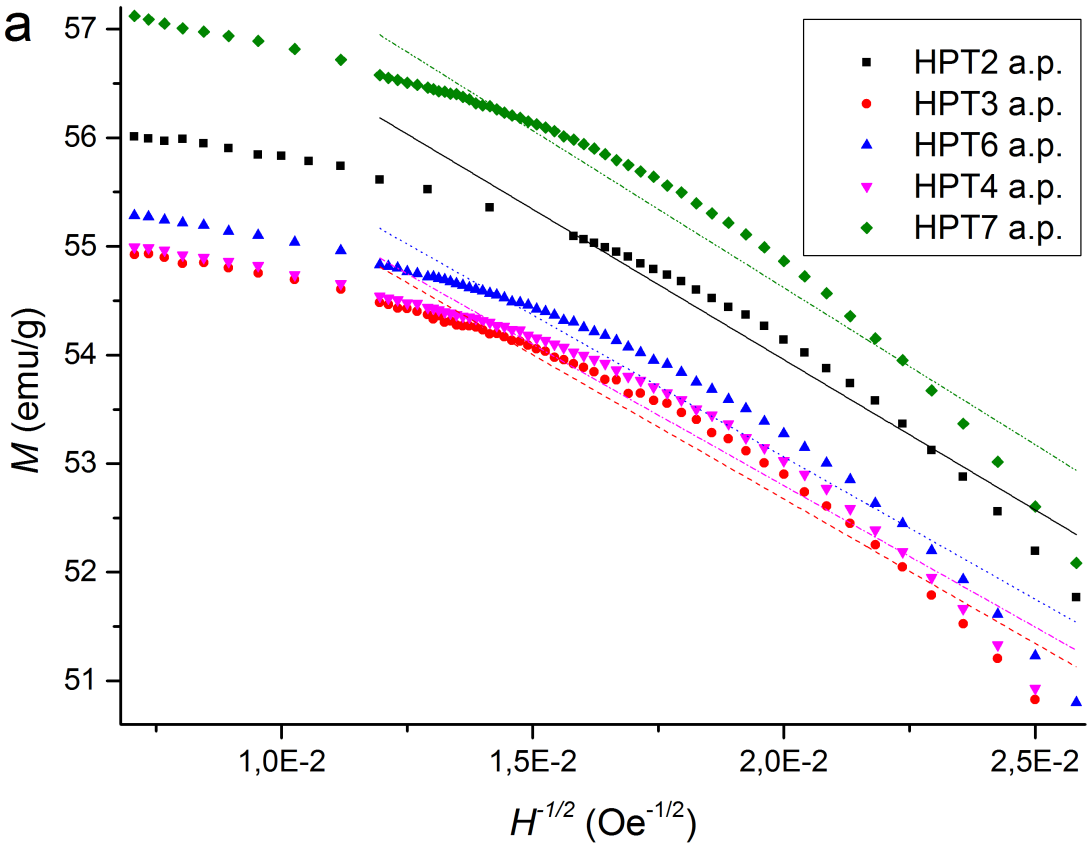
a
57
56
55
54
53
52
51
M (emu/g)
1,0E-2
1,5E-2
2,0E-2
2,5E-2
H-1/2 (Oe-1/2)
HPT2 a.p.
HPT3 a.p.
HPT6 a.p.
HPT4 a.p.
HPT7 a.p.

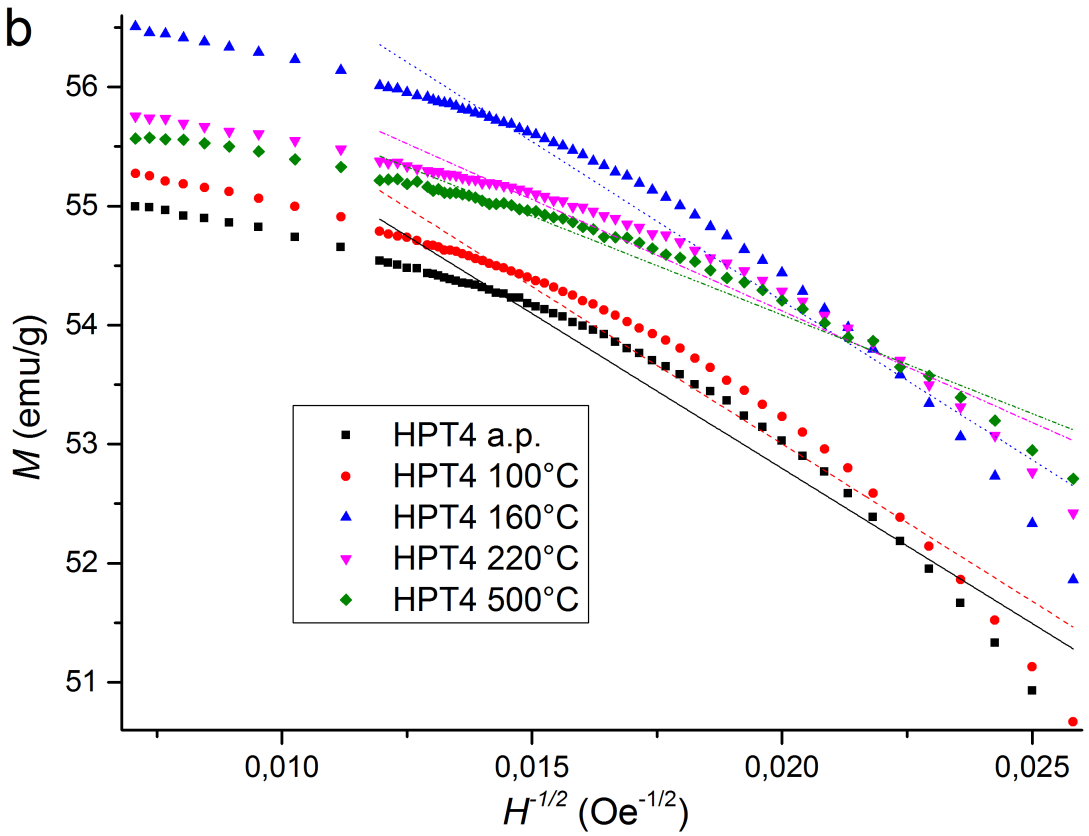
b
56
55
54
53
52
51
M (emu/g)
0,010
0,015
0,020
0,025
H-1/2 (Oe-1/2)
HPT4 a.p.
HPT4 100°C
HPT4 160°C
HPT4 220°C
HPT4 500°C

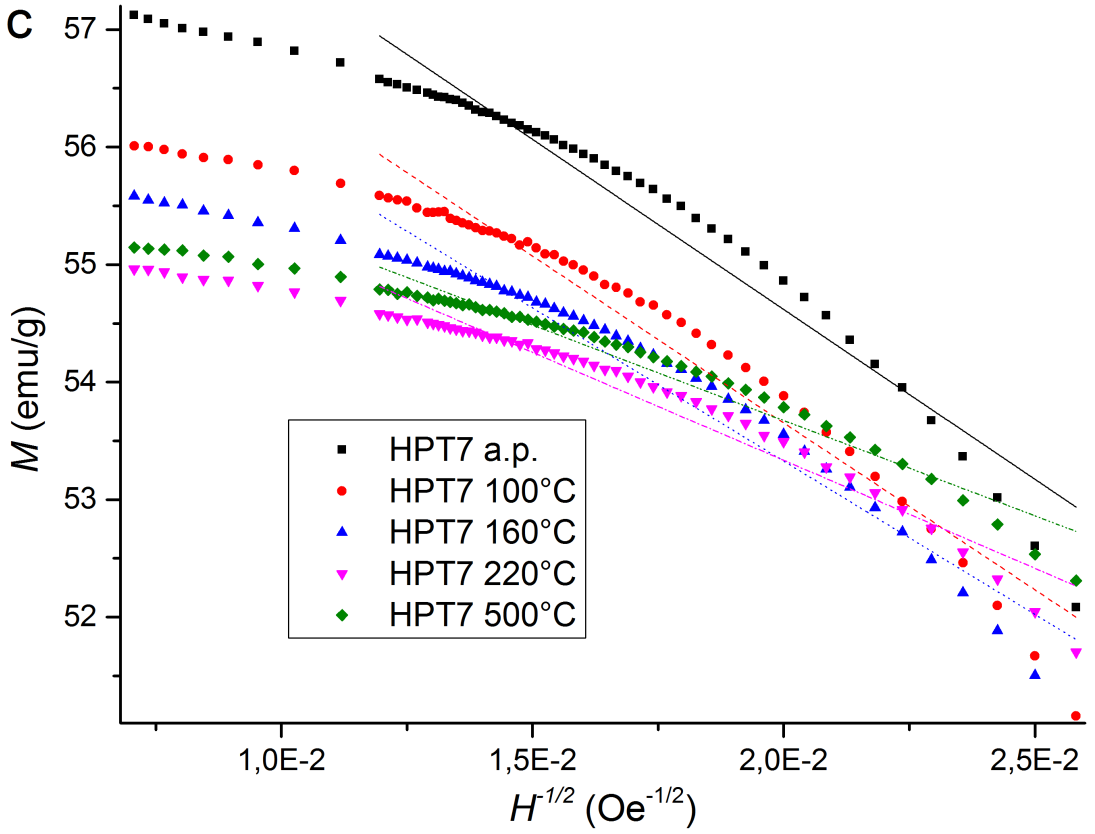
c
57
56
55
54
53
52
M (emu/g)
HPT7 a.p.
HPT7 100°C
HPT7 160°C
HPT7 220°C
HPT7 500°C
1,0E-2
1,5E-2
2,0E-2
2,5E-2
H-1/2 (Oe-1/2)

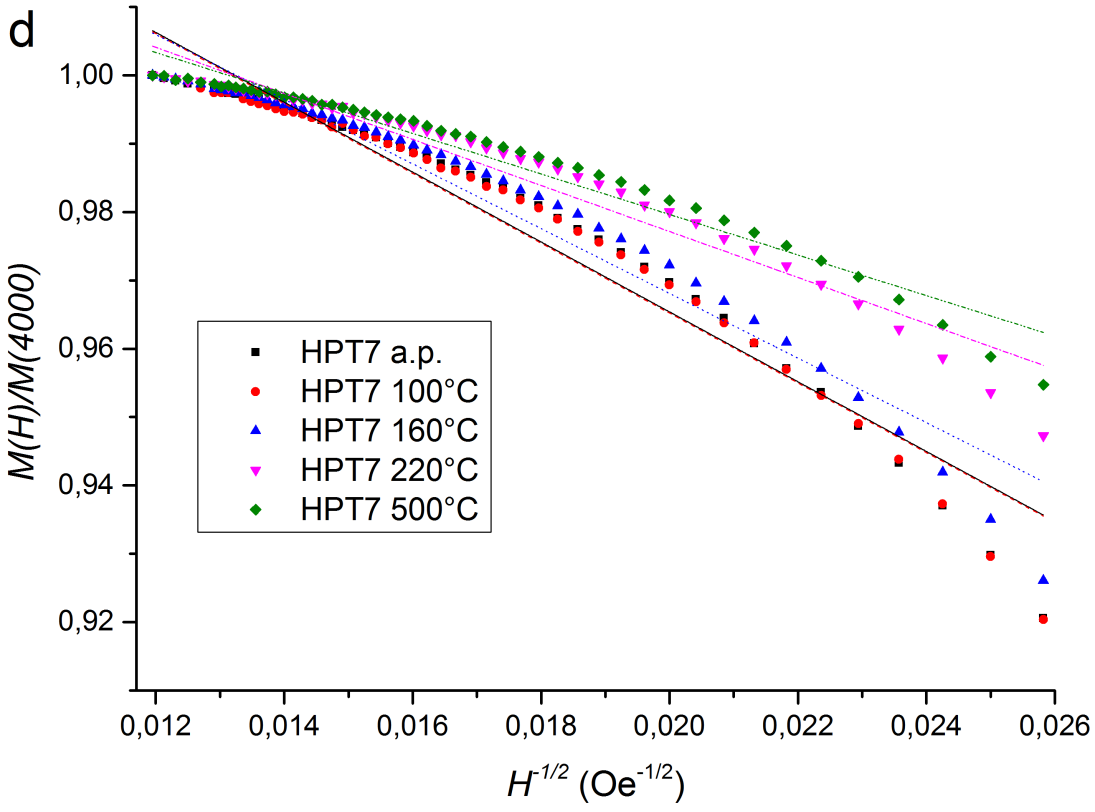
d
1,00
0,98
0,96
0,94
0,92
M(H)/M(4000)
HPT7 a.p.
HPT7 100°C
HPT7 160°C
HPT7 220°C
HPT7 500°C
0,012
0,014
0,016
0,018
0,020
0,022
0,024
0,026
H-1/2 (Oe-1/2)

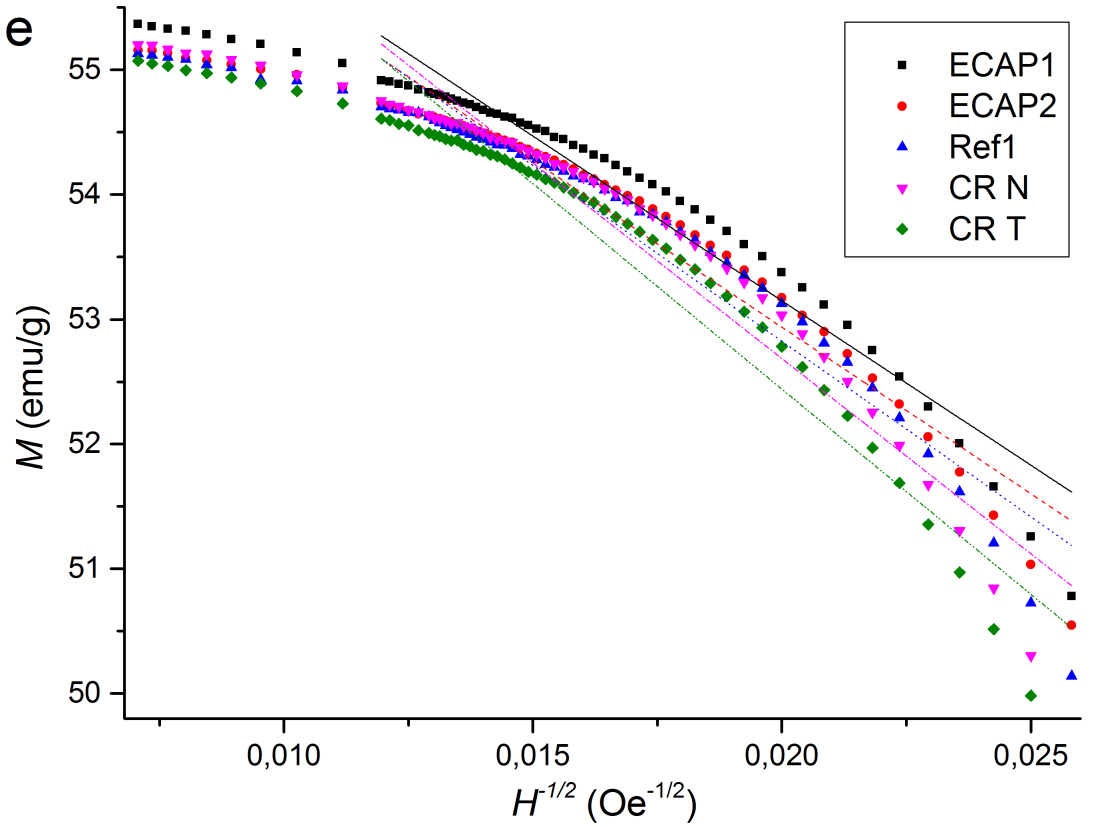
e
ECAP1
ECAP2
Ref1
CR N
CR T
M (emu/g)
55
54
53
52
51
50
0,010
0,015
0,020
0,025
H-1/2 (Oe-1/2)

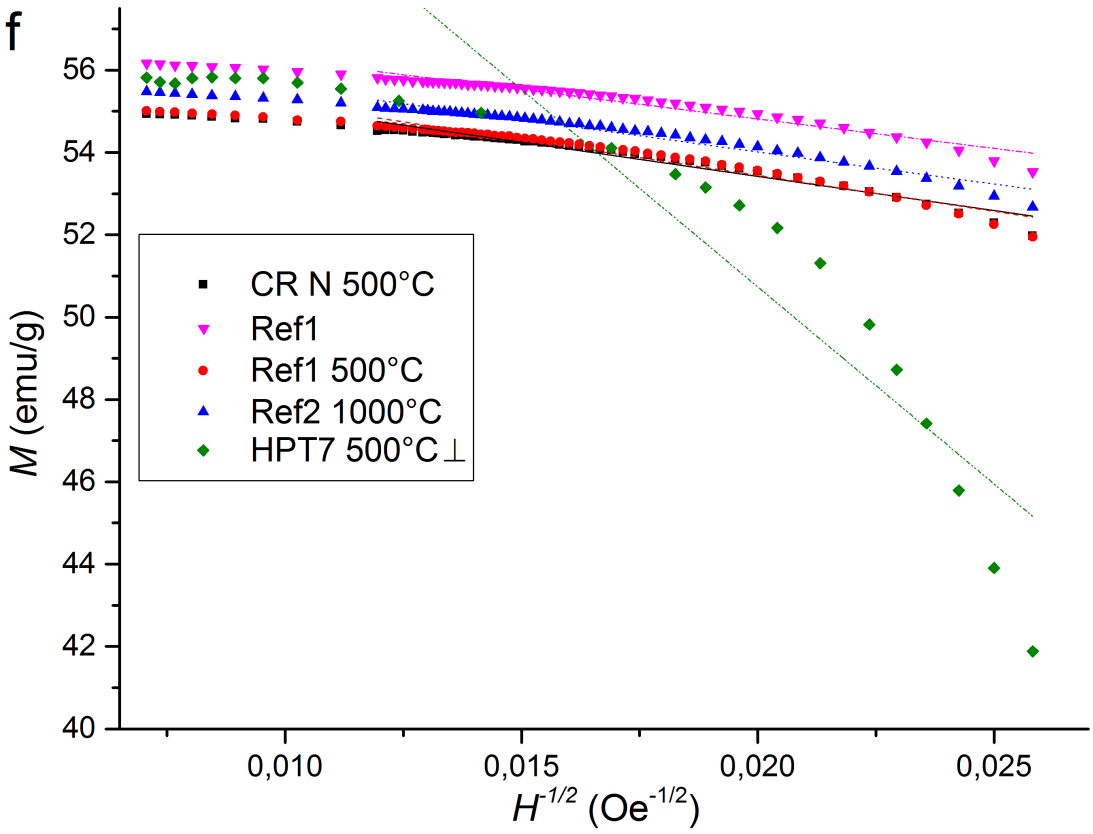
f
CR N 500°C
Ref1
Ref1 500°C
Ref2 1000°C
HPT7 500°C⊥
M (emu/g)
56
54
52
50
48
46
44
42
40
0,010
0,015
0,020
0,025
H-1/2 (Oe-1/2)

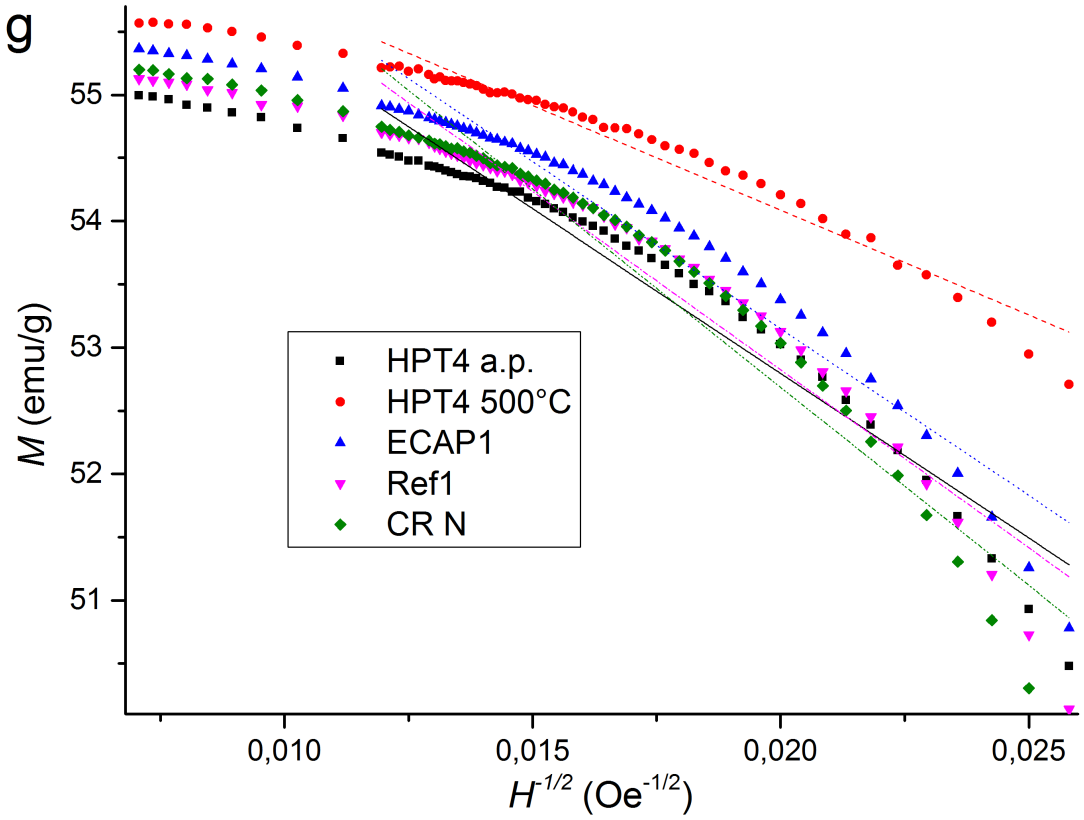

Figure A.2.: Specific magnetization M versus $1/H^{1/2}$ for the medium-field region. Linear fit as Slope*x + Intercept from table A.1 and in table A.5 for the normed figure

Table A.2.: Parameters of the fitted curves for $1/H$ (Slope$\times x$ + Intercept)

Sample	Intercept	Slope
HPT2 a.p.	56.96 ± 0.07	-7322 ± 177
HPT3 a.p.	55.71 ± 0.04	-7388 ± 125
HPT4 a.p.	55.78 ± 0.04	-7255 ± 143
HPT4 100°C	56.02 ± 0.04	-7360 ± 137
HPT4 160°C	57.26 ± 0.04	-7438 ± 131
HPT4 220°C	56.26 ± 0.03	-5222 ± 106
HPT4 500°C	55.98 ± 0.02	-4599 ± 66
HPT6 a.p.	56.05 ± 0.04	-7279 ± 126
HPT7 a.p.	57.93 ± 0.04	-8049 ± 144
HPT7 100°C	56.90 ± 0.04	-7900 ± 137
HPT7 160°C	56.31 ± 0.04	-7261 ± 132
HPT7 220°C	55.44 ± 0.03	-5114 ± 91
HPT7 500°C	55.53 ± 0.02	-4508 ± 67
HPT7 500°C $\perp$	61.41 ± 1.16	-25641 ± 2530
ECAP1	56.17 ± 0.04	-7354 ± 146
ECAP2	56.00 ± 0.04	-7452 ± 147
CR T	56.22 ± 0.07	-9202 ± 223
CR N	56.28 ± 0.07	-8766 ± 228
CR N 500°C	55.31 ± 0.02	-4602 ± 70
Ref1	56.05 ± 0.06	-7867 ± 185
Ref1 500°C	55.42 ± 0.02	-4825 ± 71
Ref2 1000°C	55.80 ± 0.02	-4335 ± 63

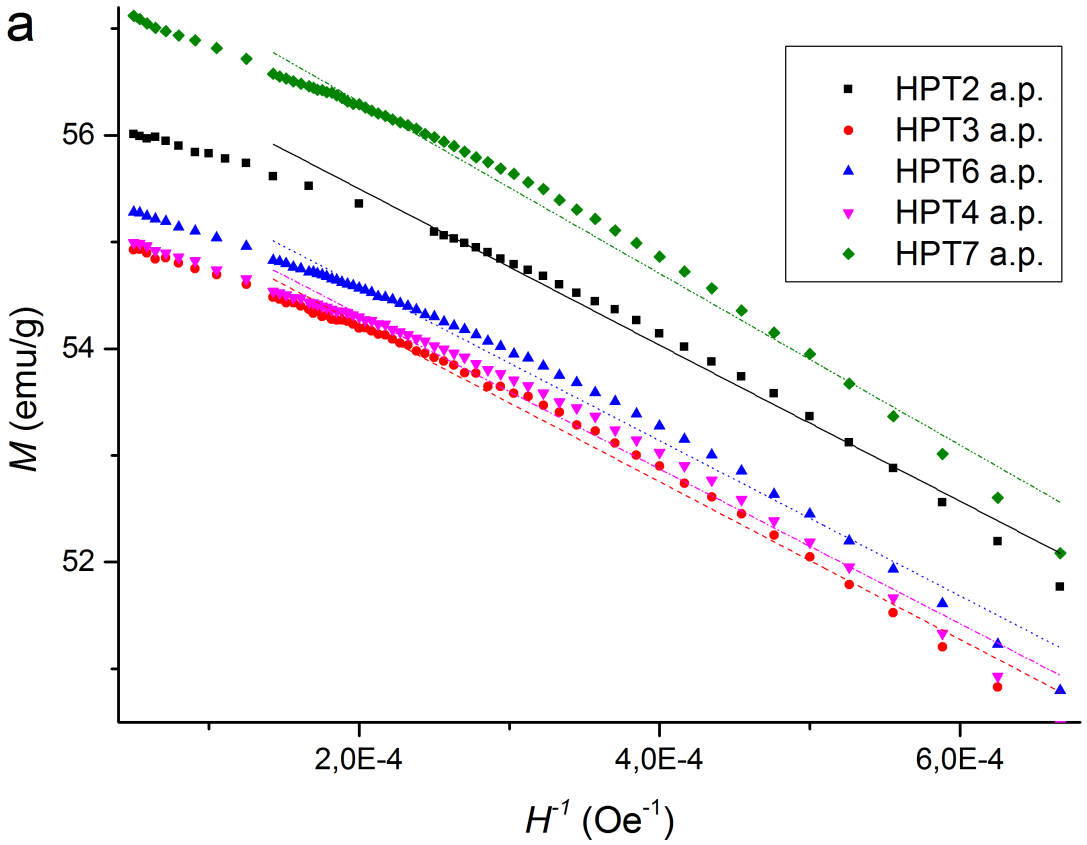
a
HPT2 a.p.
HPT3 a.p.
HPT6 a.p.
HPT4 a.p.
HPT7 a.p.
56
54
52
M (emu/g)
2,0E-4
4,0E-4
6,0E-4
H-1 (Oe-1)

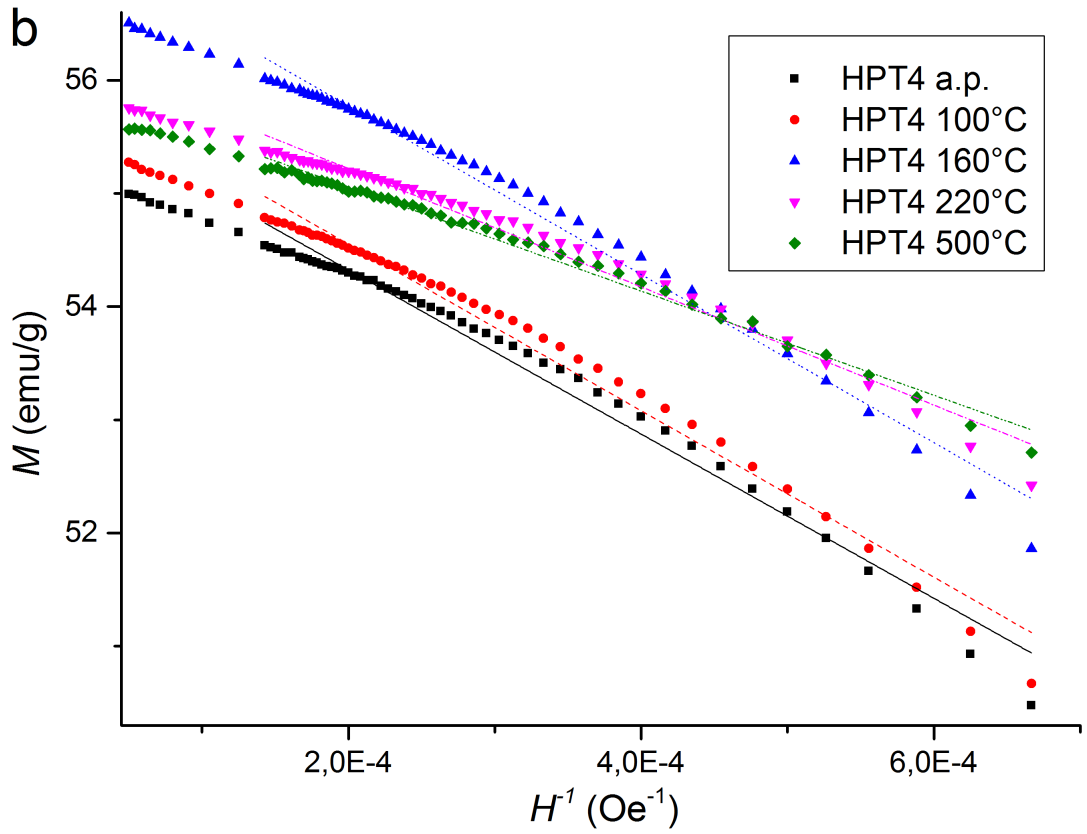
b
HPT4 a.p.
HPT4 100°C
HPT4 160°C
HPT4 220°C
HPT4 500°C
56
54
52
M (emu/g)
2,0E-4
4,0E-4
6,0E-4
H-1 (Oe-1)

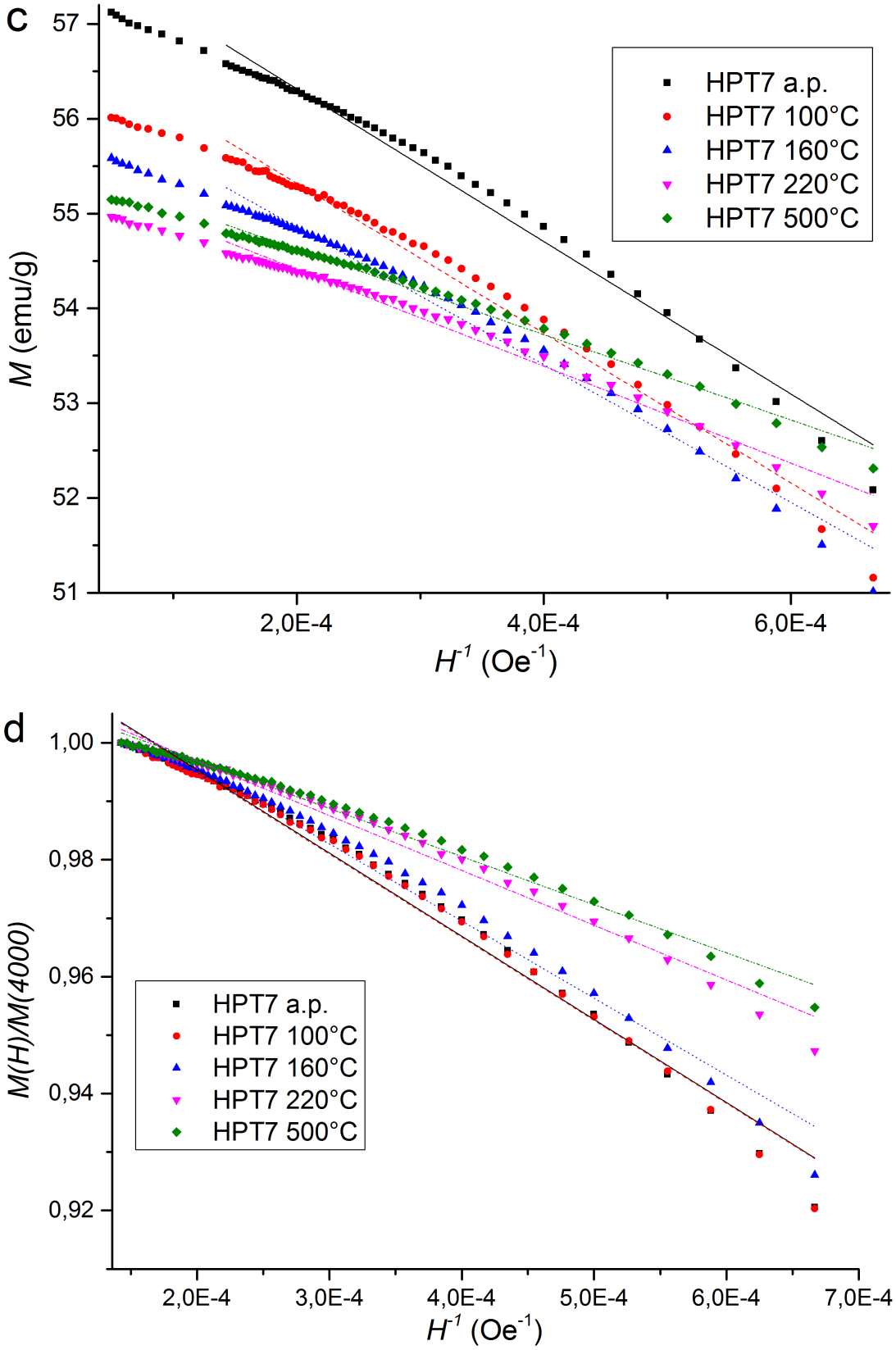
c
57
56
55
54
53
52
51
M (emu/g)
2,0E-4
4,0E-4
6,0E-4
H-1 (Oe-1)
HPT7 a.p.
HPT7 100°C
HPT7 160°C
HPT7 220°C
HPT7 500°C
d
1,00
0,98
0,96
0,94
0,92
M(H)/M(4000)
2,0E-4
3,0E-4
4,0E-4
5,0E-4
6,0E-4
7,0E-4
H-1 (Oe-1)
HPT7 a.p.
HPT7 100°C
HPT7 160°C
HPT7 220°C
HPT7 500°C

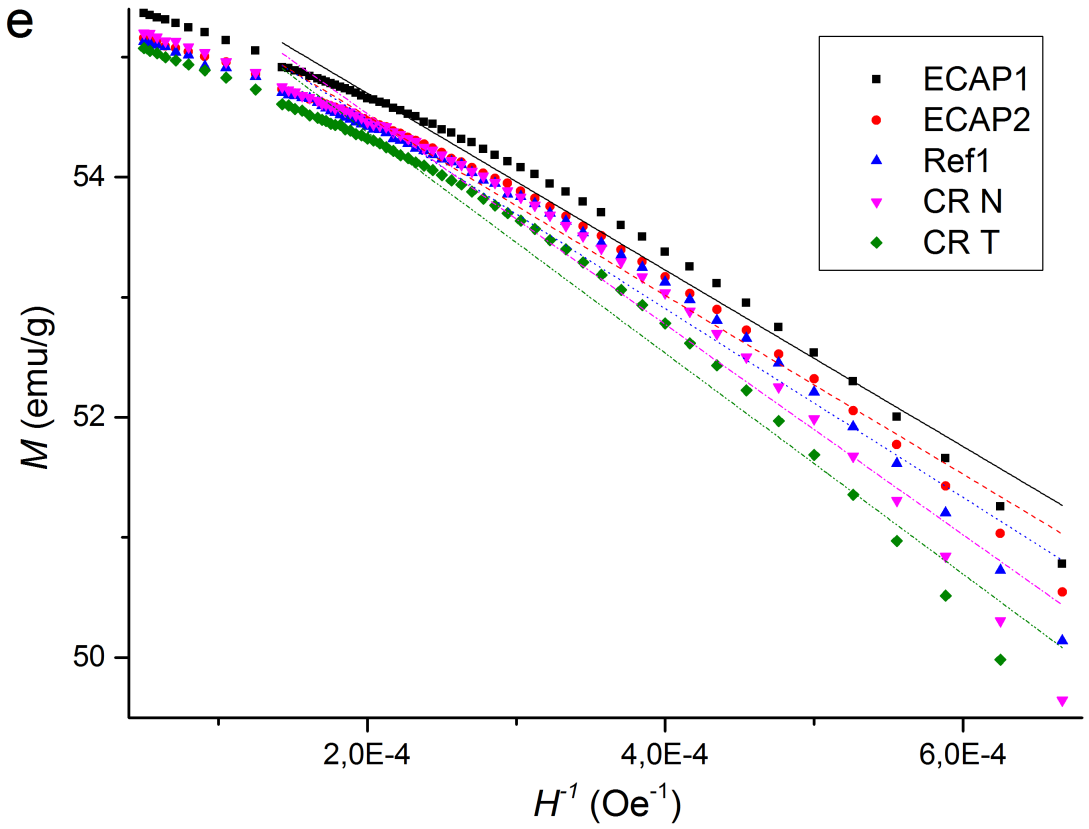
e
ECAP1
ECAP2
Ref1
CR N
CR T
M (emu/g)
54
52
50
2,0E-4
4,0E-4
6,0E-4
H-1 (Oe-1)

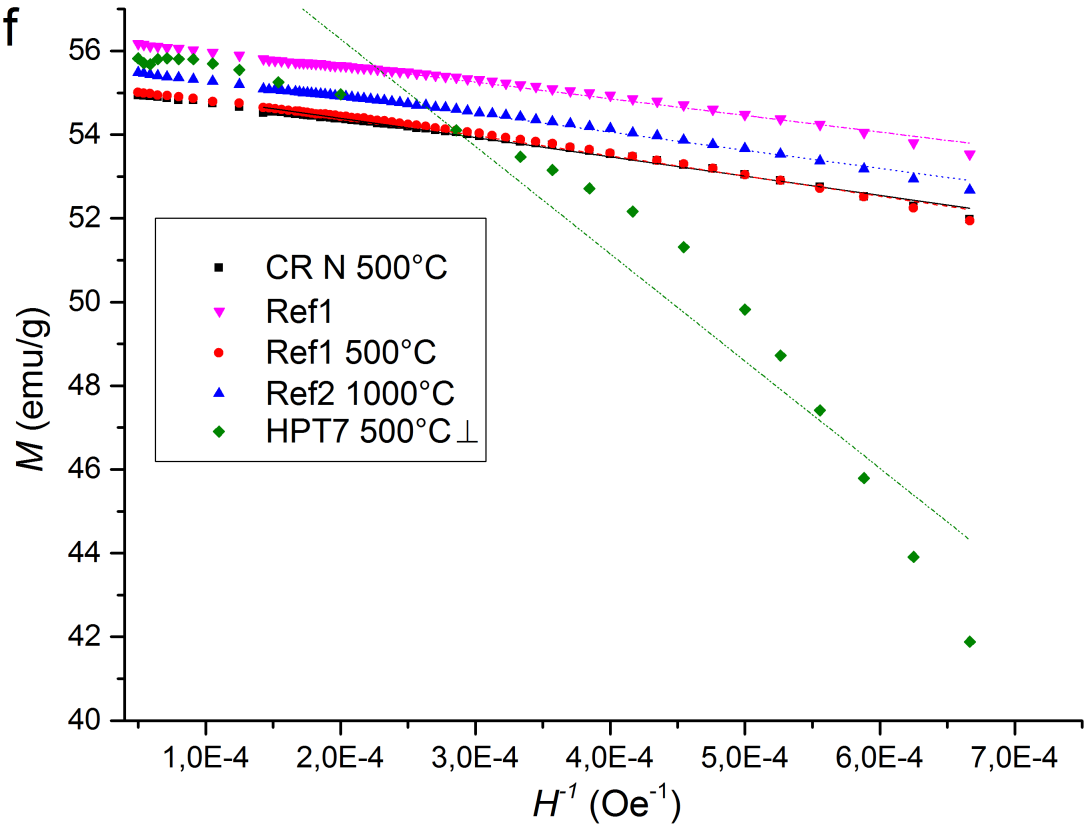
f
CR N 500°C
Ref1
Ref1 500°C
Ref2 1000°C
HPT7 500°C⊥
M (emu/g)
56
54
52
50
48
46
44
42
40
1,0E-4
2,0E-4
3,0E-4
4,0E-4
5,0E-4
6,0E-4
7,0E-4
H-1 (Oe-1)

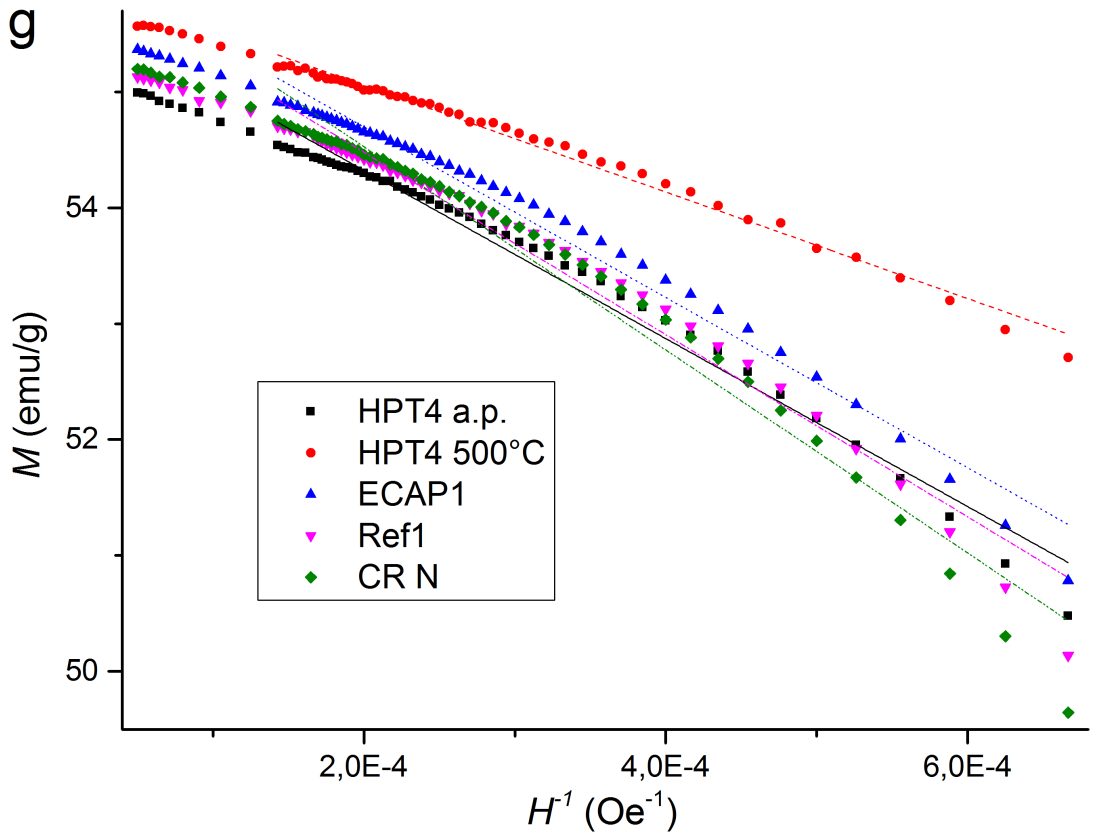

Figure A.3.: Specific magnetization M versus $1/H$ for the medium-field region. Linear fit as Slope*x + Intercept from table A.2 and in table A.5 for the normed figure

Table A.3.: Parameters of the fitted curves for $1/H^{3/2}$ (Slope$\times x$ + Intercept)

Sample	Intercept	Slope$[10^5]$
HPT2 a.p.	56.05 ± 0.01	-2.40 ± 0.01
HPT3 a.p.	54.93 ± 0.01	-2.57 ± 0.01
HPT4 a.p.	55.00 ± 0.01	-2.49 ± 0.01
HPT4 100°C	55.24 ± 0.01	-2.54 ± 0.01
HPT4 160°C	56.47 ± 0.00	-2.58 ± 0.01
HPT4 220°C	55.70 ± 0.01	-1.79 ± 0.01
HPT4 500°C	55.50 ± 0.00	-1.62 ± 0.01
HPT6 a.p.	55.28 ± 0.00	-2.53 ± 0.01
HPT7 a.p.	57.10 ± 0.01	-2.84 ± 0.01
HPT7 100°C	56.09 ± 0.01	-2.79 ± 0.01
HPT7 160°C	55.56 ± 0.01	-2.57 ± 0.01
HPT7 220°C	54.91 ± 0.01	-1.81 ± 0.01
HPT7 500°C	55.06 ± 0.00	-1.59 ± 0.00
HPT7 500°C $\perp$	58.51 ± 0.63	-8.70 ± 0.61
ECAP1	55.39 ± 0.01	-2.54 ± 0.01
ECAP2	55.21 ± 0.01	-2.58 ± 0.01
CR T	55.23 ± 0.02	-3.15 ± 0.03
CR N	55.33 ± 0.02	-2.97 ± 0.03
CR N 500°C	54.84 ± 0.00	-1.62 ± 0.01
Ref1	55.20 ± 0.01	-2.68 ± 0.02
Ref1 500°C	54.93 ± 0.00	-1.70 ± 0.01
Ref2 1000°C	55.35 ± 0.00	-1.53 ± 0.00

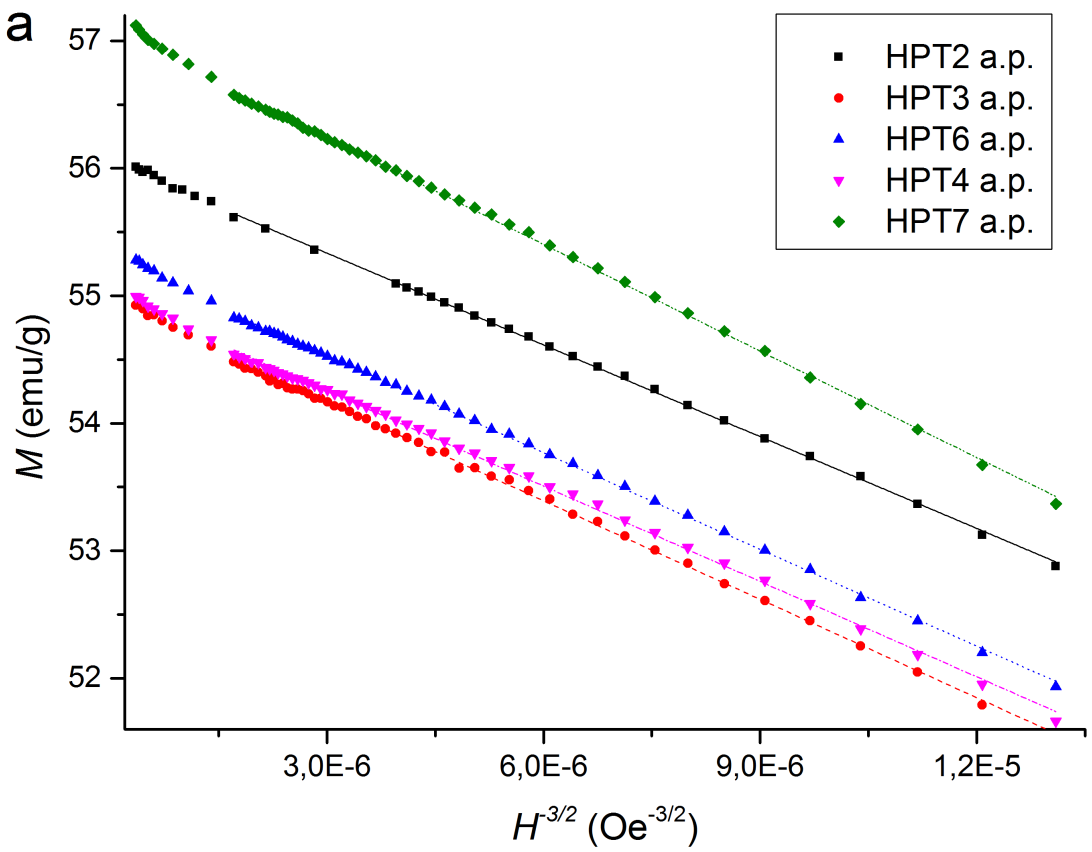
a
HPT2 a.p.
HPT3 a.p.
HPT6 a.p.
HPT4 a.p.
HPT7 a.p.
M (emu/g)
57
56
55
54
53
52
3,0E-6
6,0E-6
9,0E-6
1,2E-5
H-3/2 (Oe-3/2)

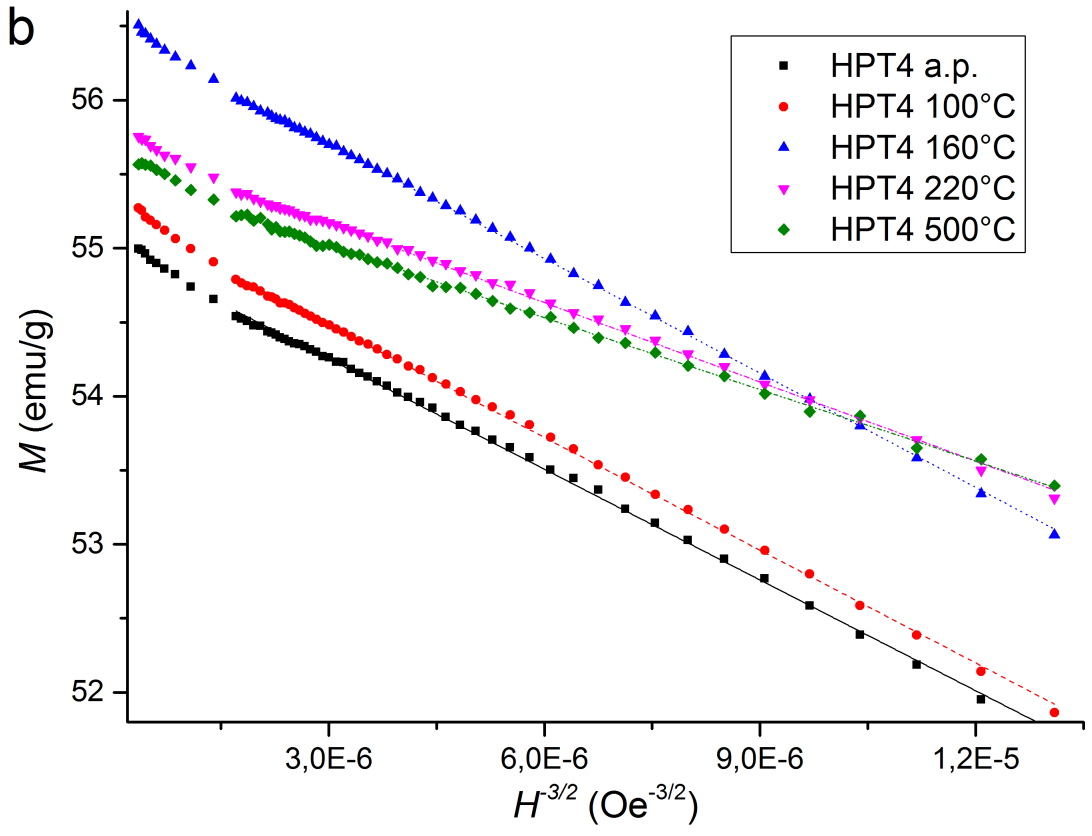
b
HPT4 a.p.
HPT4 100°C
HPT4 160°C
HPT4 220°C
HPT4 500°C
M (emu/g)
56
55
54
53
52
3,0E-6
6,0E-6
9,0E-6
1,2E-5
H-3/2 (Oe-3/2)

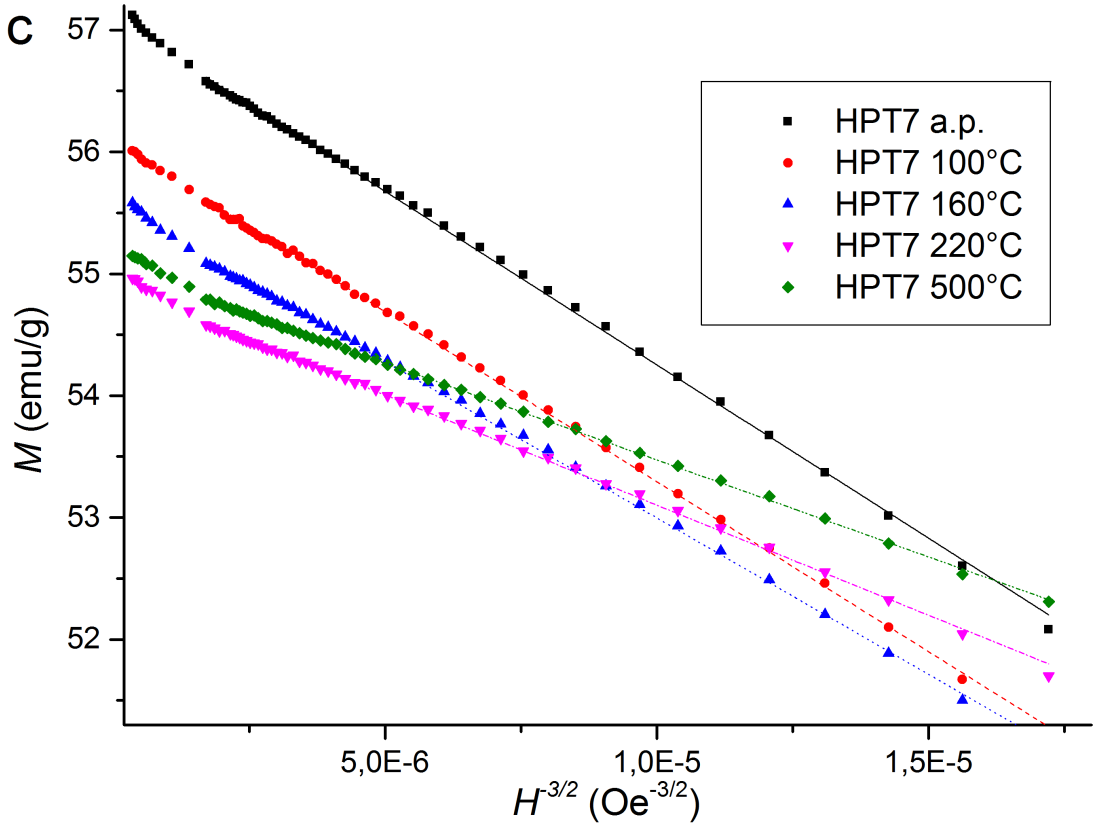
c
57
56
55
54
53
52
M (emu/g)
HPT7 a.p.
HPT7 100°C
HPT7 160°C
HPT7 220°C
HPT7 500°C
5,0E-6
1,0E-5
1,5E-5
H-3/2 (Oe-3/2)

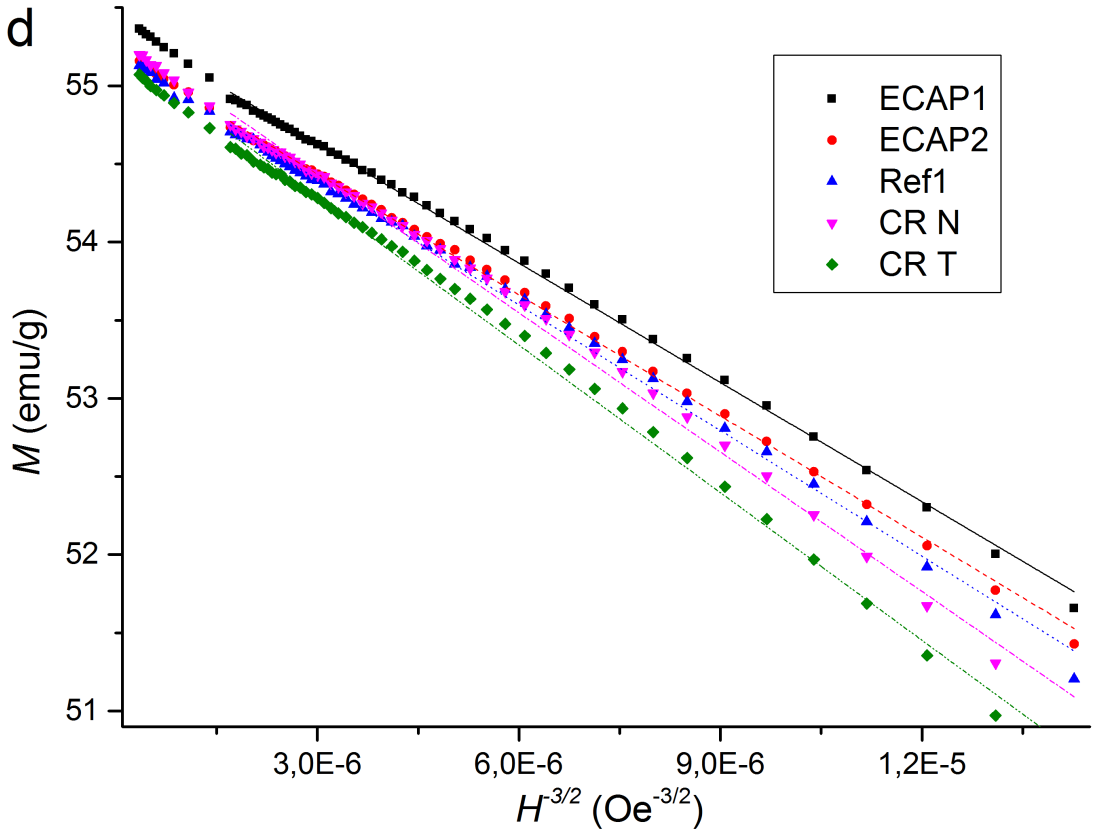
d
55
54
53
52
51
M (emu/g)
ECAP1
ECAP2
Ref1
CR N
CR T
3,0E-6
6,0E-6
9,0E-6
1,2E-5
H-3/2 (Oe-3/2)

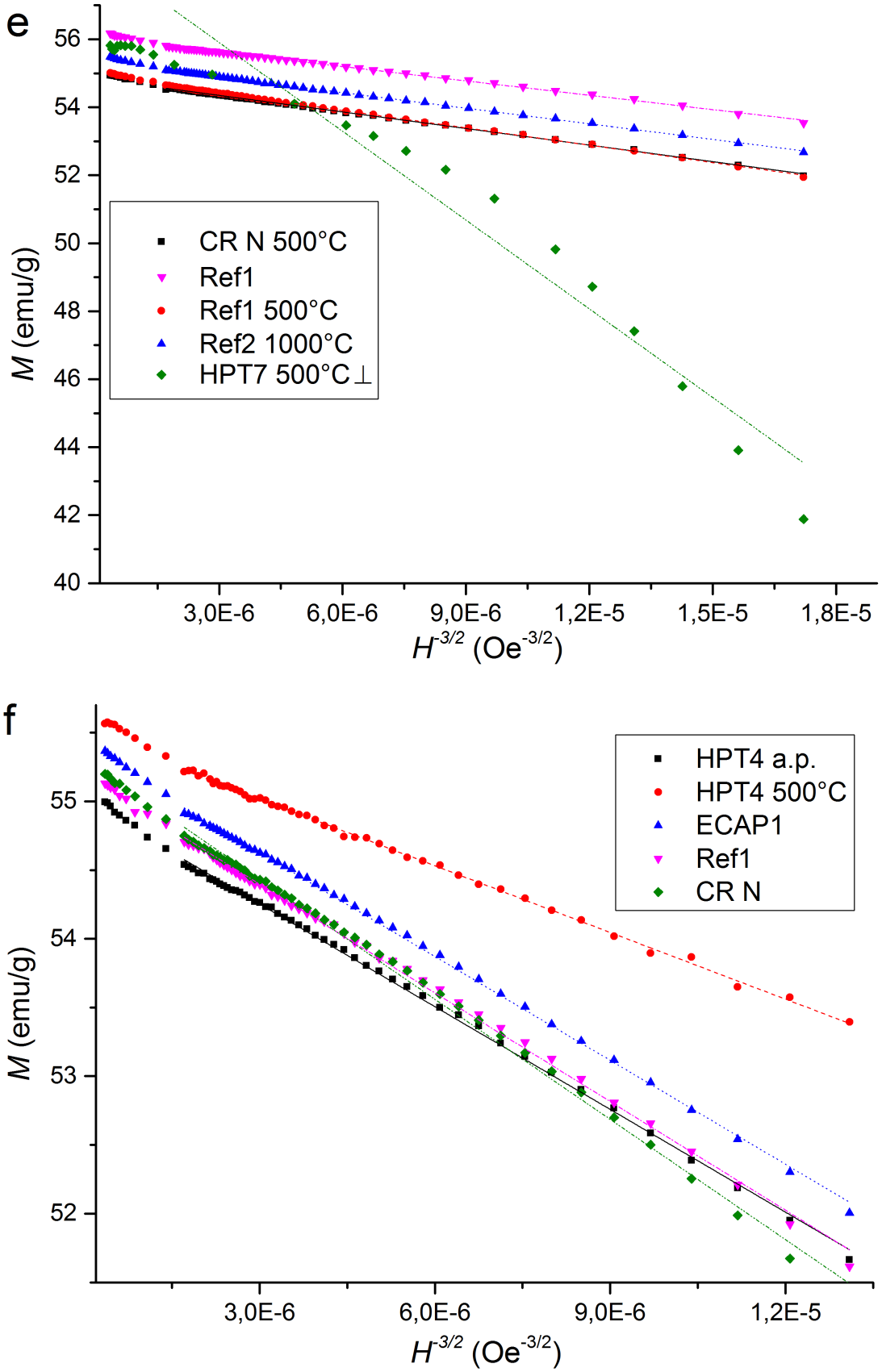

Figure A.4.: Specific magnetization M versus $1/H^{3/2}$ for the medium-field region. Linear fit as Slope*x + Intercept from table A.3

Table A.4.: Parameters of the fitted curves for $1/H^2$ (Slope$\times x$ + Intercept)

Sample	Intercept	Slope $[10^6]$
HPT2 a.p.	55.64 ± 0.02	-8.98 ± 0.10
HPT3 a.p.	54.57 ± 0.02	-9.91 ± 0.11
HPT4 a.p.	54.66 ± 0.01	-9.77 ± 0.07
HPT4 100°C	54.89 ± 0.01	-9.89 ± 0.09
HPT4 160°C	56.12 ± 0.01	-9.99 ± 0.10
HPT4 220°C	55.46 ± 0.01	-7.04 ± 0.05
HPT4 500°C	55.27 ± 0.01	-6.14 ± 0.09
HPT6 a.p.	54.93 ± 0.01	-9.77 ± 0.10
HPT7 a.p.	56.69 ± 0.01	-10.82 ± 0.10
HPT7 100°C	55.68 ± 0.02	-10.61 ± 0.11
HPT7 160°C	55.19 ± 0.01	-9.76 ± 0.09
HPT7 220°C	54.65 ± 0.01	-6.87 ± 0.07
HPT7 500°C	54.83 ± 0.01	-6.03 ± 0.08
HPT7 500°C $\perp$	57.00 ± 0.35	-31.81 ± 1.44
ECAP1	55.04 ± 0.01	-9.90 ± 0.07
ECAP2	54.85 ± 0.01	-10.00 ± 0.08
CR T	54.81 ± 0.01	-12.53 ± 0.04
CR N	54.95 ± 0.00	-11.92 ± 0.03
CR N 500°C	54.60 ± 0.01	-6.16 ± 0.08
Ref1	54.85 ± 0.01	-10.58 ± 0.05
Ref1 500°C	54.68 ± 0.01	-6.45 ± 0.08
Ref2 1000°C	55.13 ± 0.01	-5.80 ± 0.08

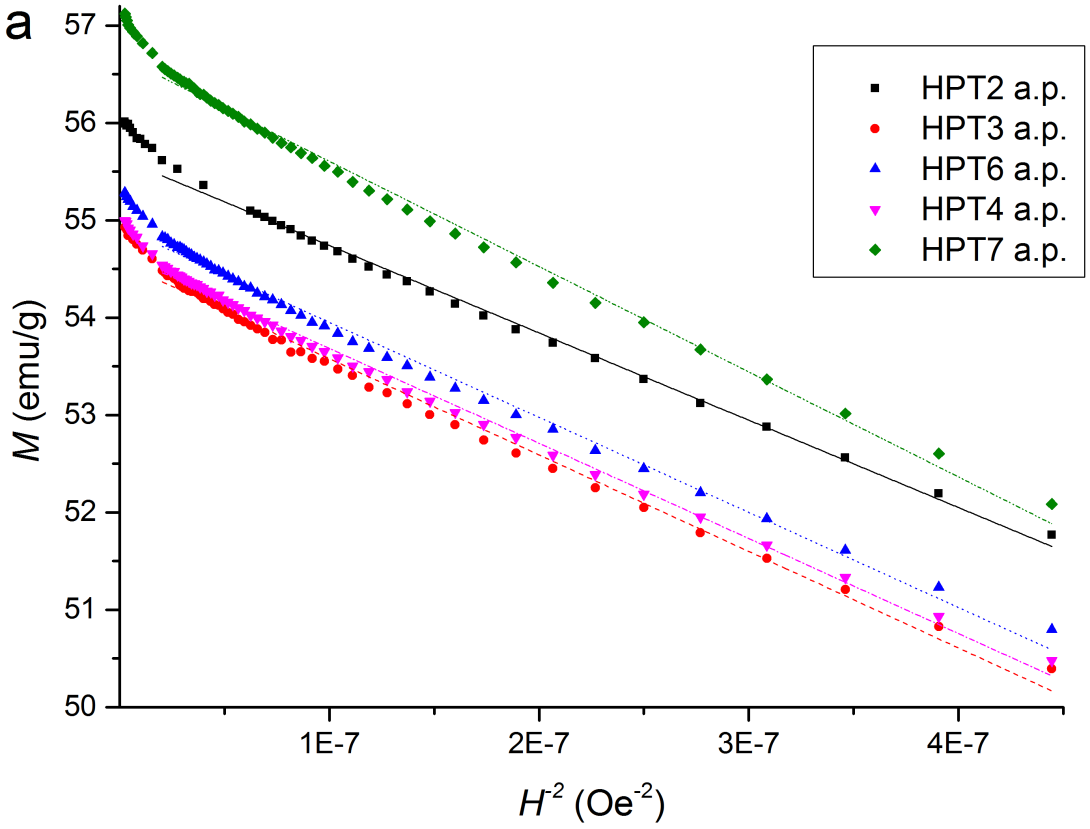
a
HPT2 a.p.
HPT3 a.p.
HPT6 a.p.
HPT4 a.p.
HPT7 a.p.
M (emu/g)
57
56
55
54
53
52
51
50
1E-7
2E-7
3E-7
4E-7
H-2 (Oe-2)

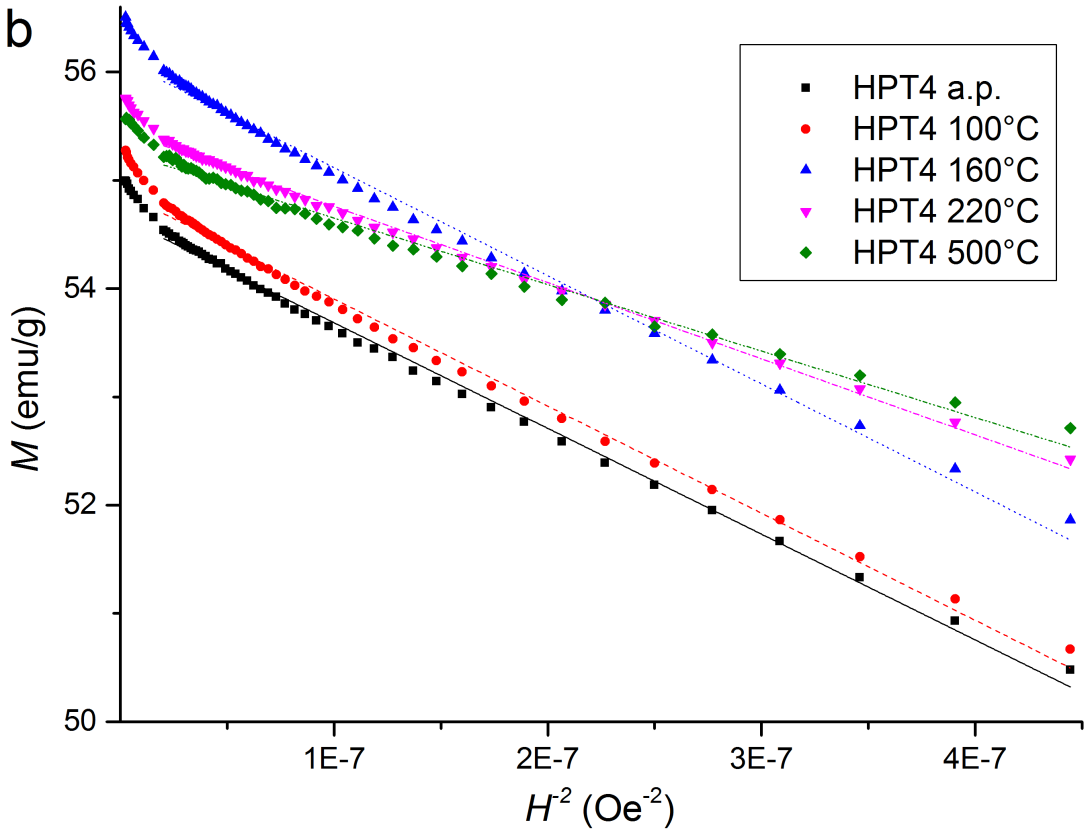
b
HPT4 a.p.
HPT4 100°C
HPT4 160°C
HPT4 220°C
HPT4 500°C
M (emu/g)
56
54
52
50
1E-7
2E-7
3E-7
4E-7
H-2 (Oe-2)

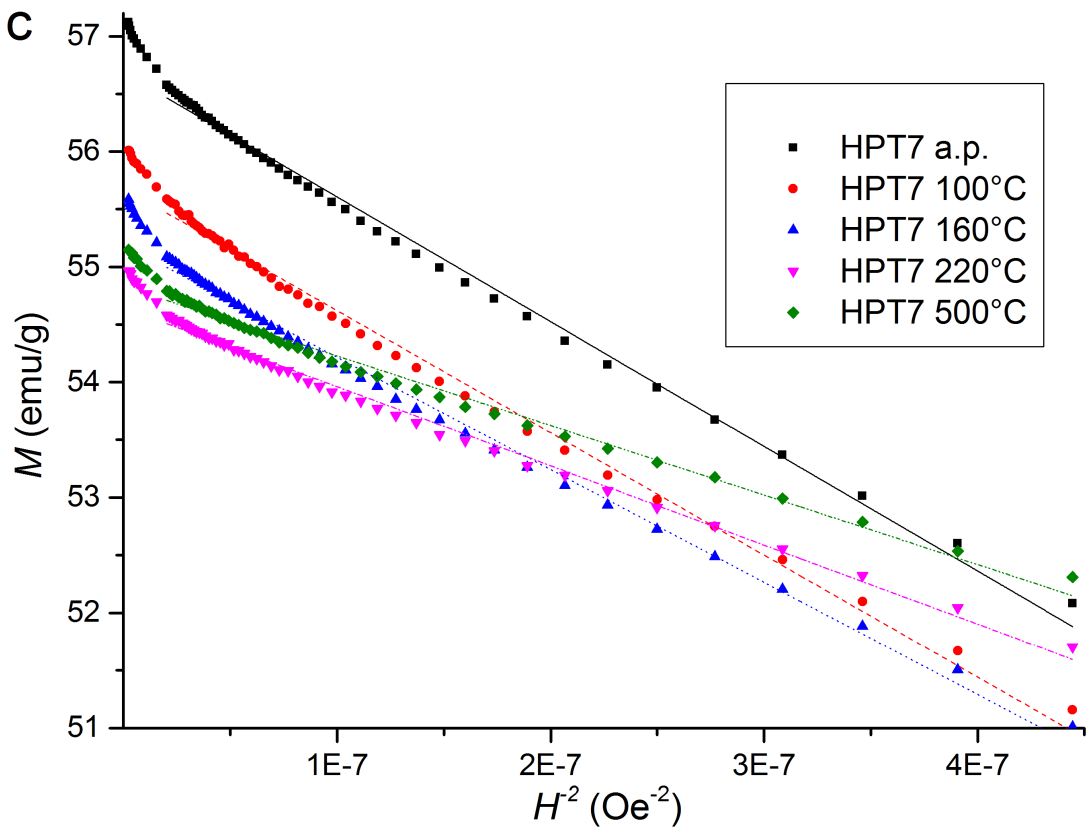
c
57
56
55
54
53
52
51
M (emu/g)
1E-7
2E-7
3E-7
4E-7
H-2 (Oe-2)
HPT7 a.p.
HPT7 100°C
HPT7 160°C
HPT7 220°C
HPT7 500°C

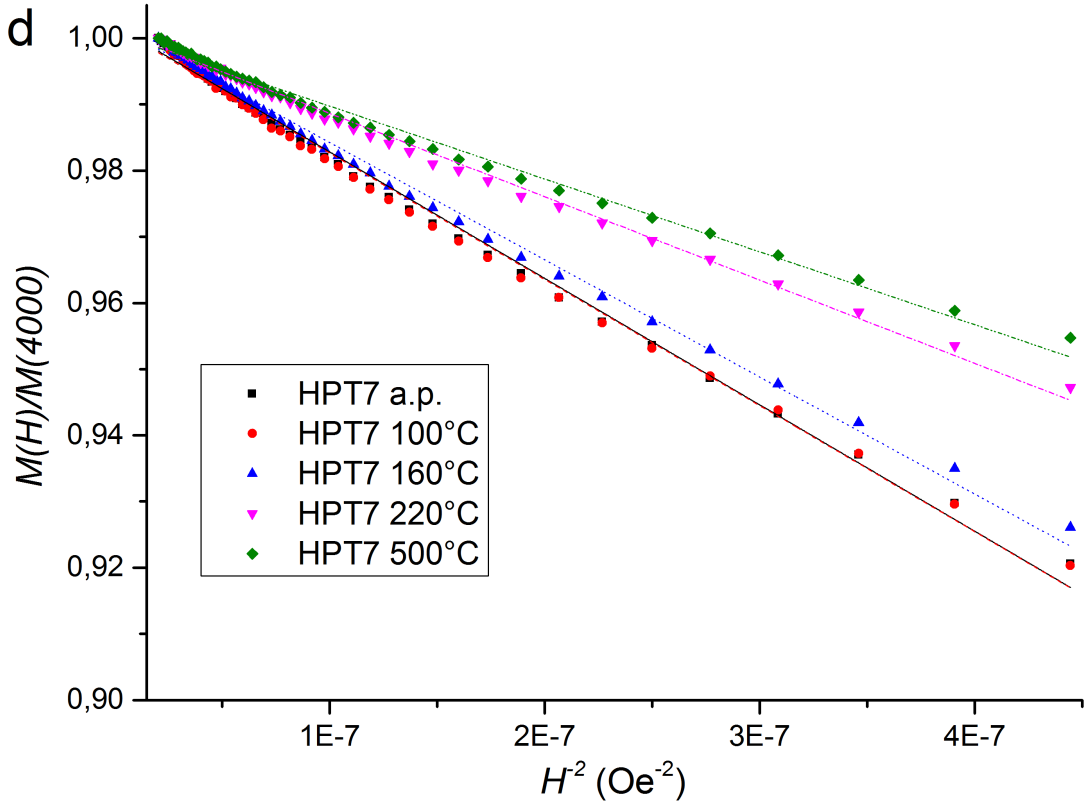
d
1,00
0,98
0,96
0,94
0,92
0,90
M(H)/M(4000)
1E-7
2E-7
3E-7
4E-7
H-2 (Oe-2)
HPT7 a.p.
HPT7 100°C
HPT7 160°C
HPT7 220°C
HPT7 500°C

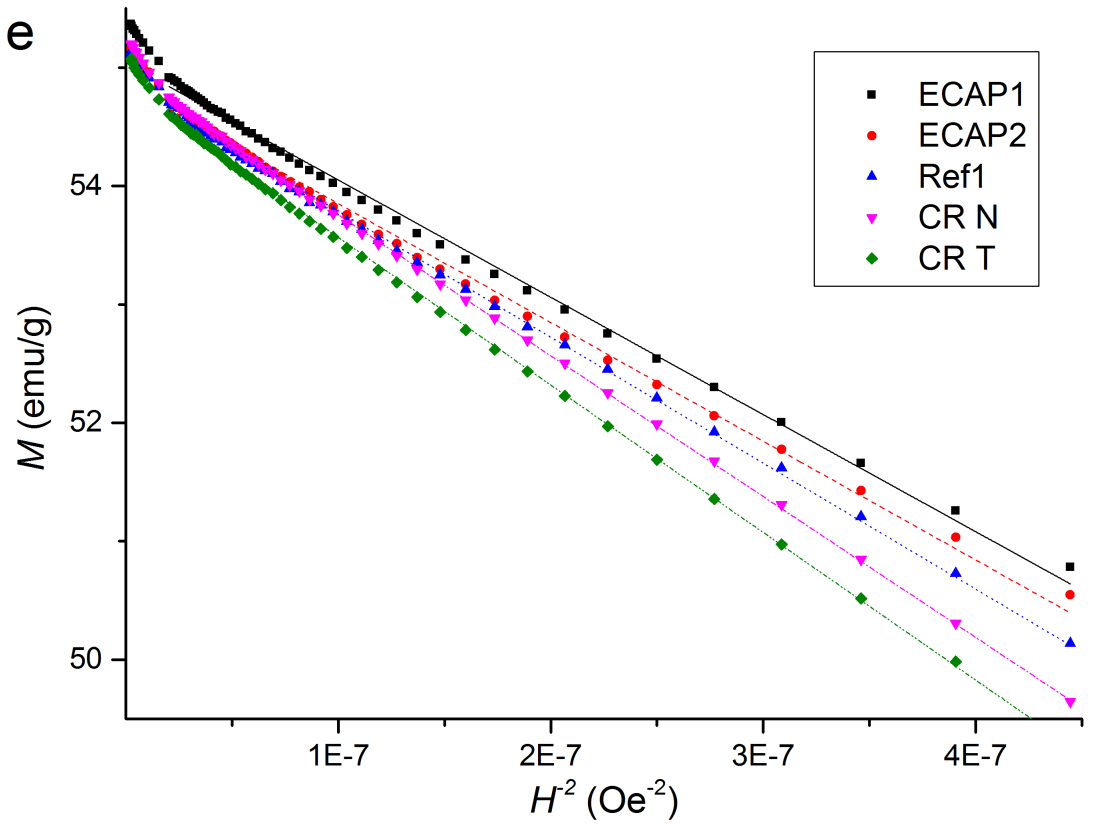
e
ECAP1
ECAP2
Ref1
CR N
CR T
M (emu/g)
54
52
50
1E-7
2E-7
3E-7
4E-7
H-2 (Oe-2)

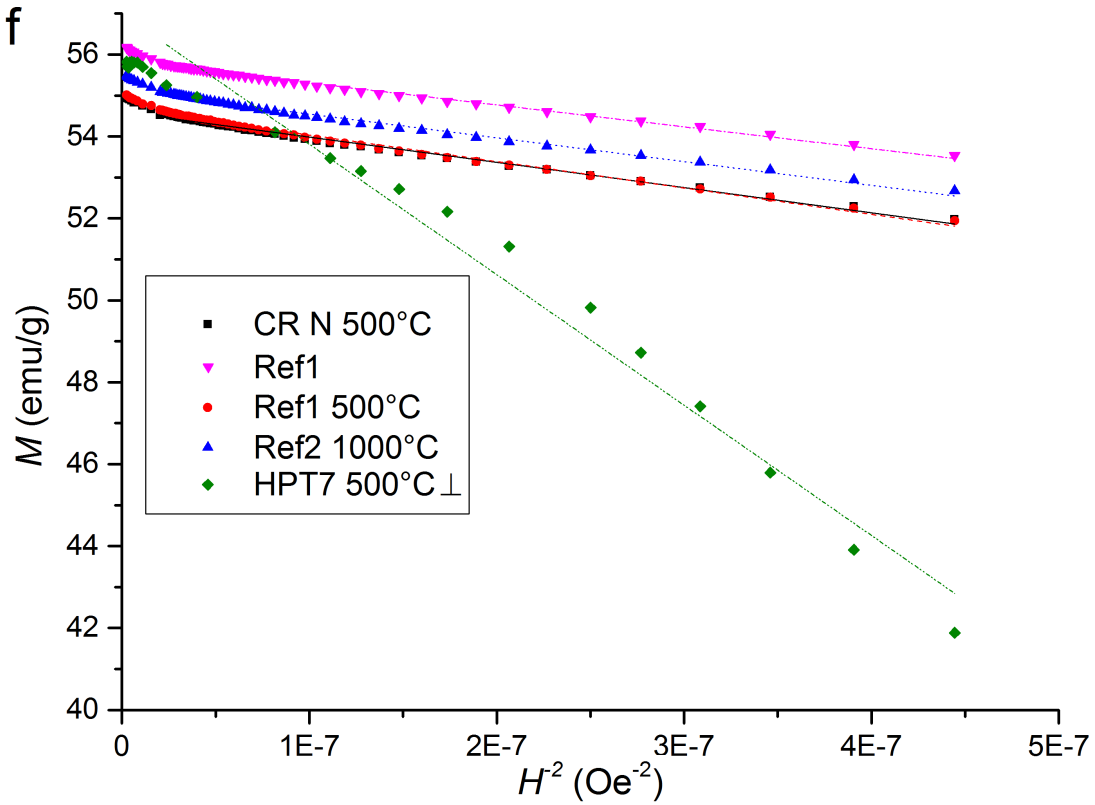
f
CR N 500°C
Ref1
Ref1 500°C
Ref2 1000°C
HPT7 500°C⊥
M (emu/g)
56
54
52
50
48
46
44
42
40
0
1E-7
2E-7
3E-7
4E-7
5E-7
H-2 (Oe-2)

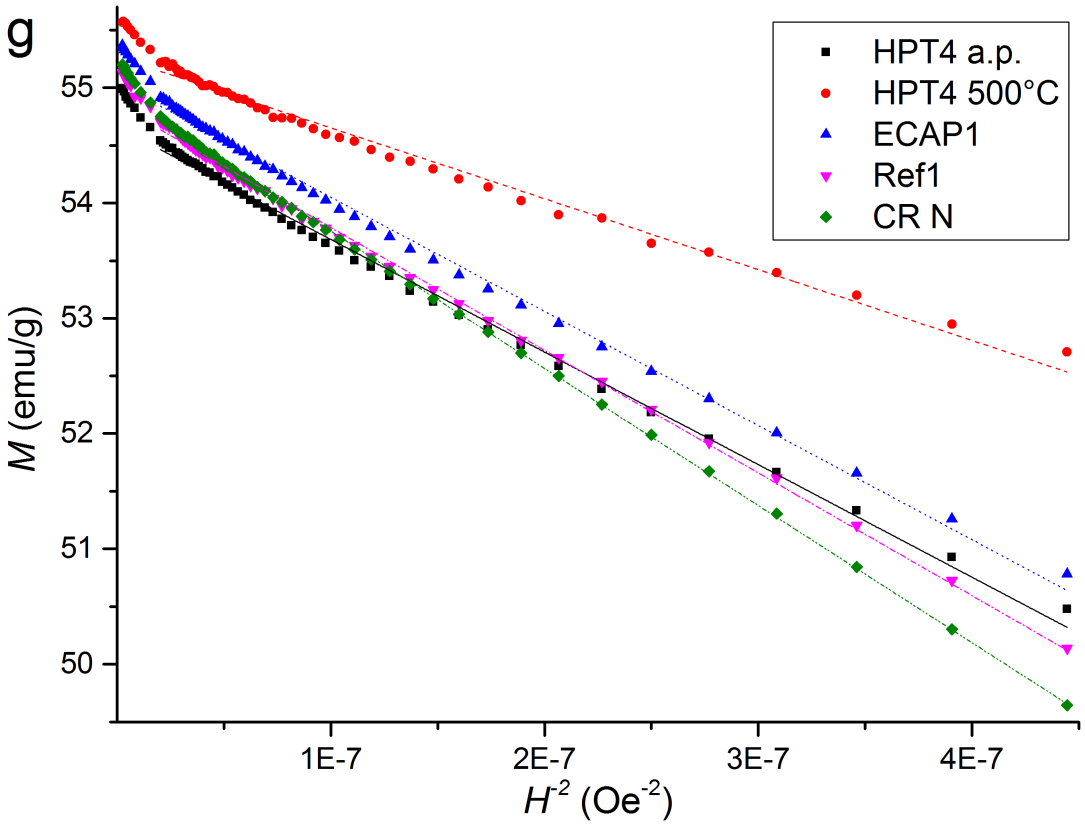

Figure A.5.: Specific magnetization M versus $1/H^2$ for the medium-field region. Linear fit as Slope*x + Intercept from table A.4 and in table A.5 for the normed figure

Table A.5.: Parameters of the fitted curves for HPT7 of all annealing stages and fits (Slope$\times x$ + Intercept)

Sample	Value	$H^{-1/2}$	H^{-1}	$H^{-3/2}$	H^{-2}
HPT7 a.p.	Intercept	1.07 ± 0.01	1.02 ± 0.00	1.01 ± 0.00	1.0020 ± 0.0002
	Slope	-5.11 ± 0.17	-142.2 ± 2.5	-5027.67 ± 20.34	-191074 ± 1789
HPT7 100°C	Intercept	1.07 ± 0.01	1.02 ± 0.00	1.01 ± 0.00	1.0017 ± 0.0001
	Slope	-5.11 ± 0.16	-142.1 ± 2.4	-5020 ± 19	-190714 ± 1931
HPT7 160°C	Intercept	1.06 ± 0.01	1.02 ± 0.00	1.01 ± 0.00	1.0020 ± 0.0002
	Slope	-4.74 ± 0.16	-131.8 ± 2.4	-4659 ± 20	-177110 ± 1604
HPT7 220°C	Intercept	1.04 ± 0.01	1.02 ± 0.00	1.01 ± 0.00	1.0012 ± 0.0001
	Slope	-3.37 ± 0.11	-93.7 ± 1.6	-3310 ± 15	-125821 ± 1206
HPT7 500°C	Intercept	1.04 ± 0.01	1.01 ± 0.00	1.01 ± 0.00	1.0008 ± 0.0000
	Slope	-2.96 ± 0.09	-82.2 ± 1.2	-2901 ± 7	-110055 ± 1380

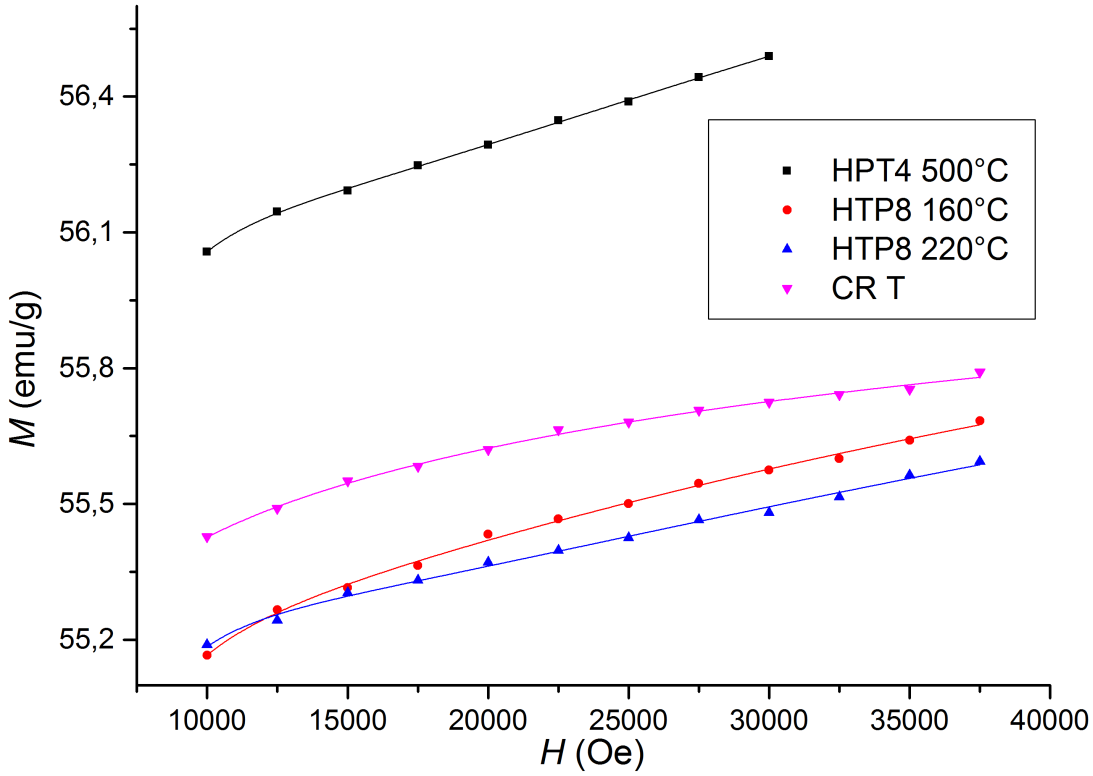

Figure A.6.: HPT4, HPT8 and CR T samples for the high-field region fitted with equation 2.3. M : specific magnetization, H : applied magnetic field.

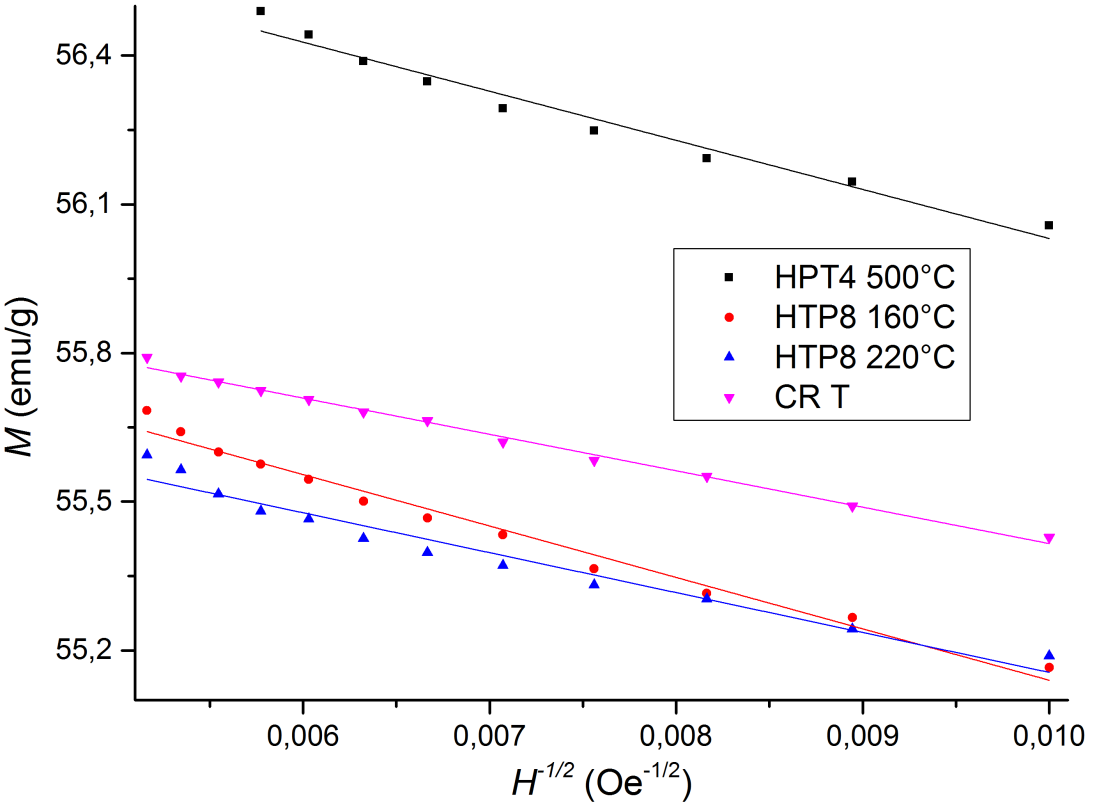

Figure A.7.: Specific magnetization M versus $1/H^{1/2}$ for HPT4, HPT8 and CR T samples in the high-field region.

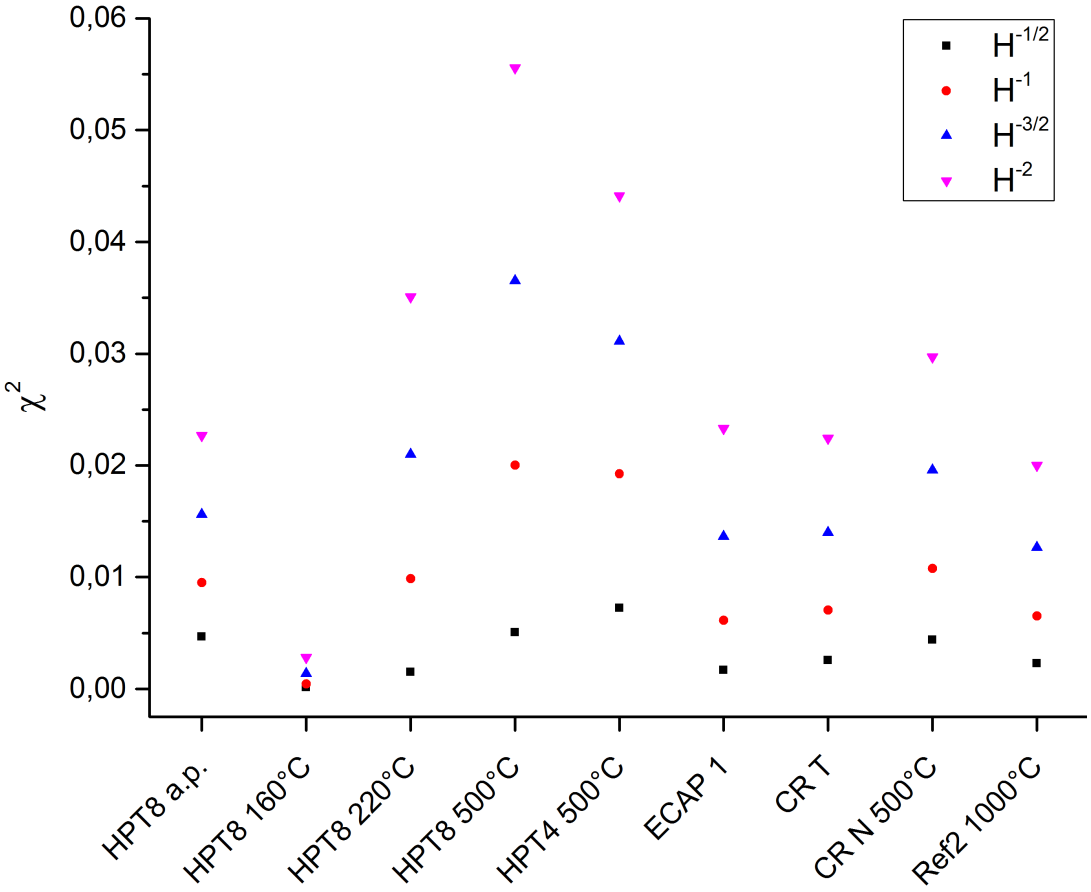

Figure A.8.: χ^2 for linear fits according to H^{-x} in high-field range.

Acknowledgments

Many people supported me during this thesis with advice, supervision and knowledge. I am indebted to:

- Univ.-Prof. Dr. Roland Würschum, Institut für Materialphysik, TU Graz for supervising this thesis, finding the time to answer my questions and his guidance
- Univ.-Prof. Dr. Heinz Krenn, Institut für Physik, Universität Graz for the possibility to use the SQUID and assisting to explain the magnetic effects which occur
- Dr. techn. Stefan Topolovec, Insitut für Materialphysik, TU Graz for helping with the interpretation of the SQUID measurements and providing advice for writing this work
- Dipl.-Ing. Gregor Klinser, Institut für Materialphysik, TU Graz for supporting me with the SQUID measurements and the discussions explaining their results
- Dipl.-Ing. Jaromir Kotzurek, Institut für Materialphysik, TU Graz for help with the preparation of the samples, sawing them from the disc and the dilatometric measurements
- Univ.-Prof. Dr. Reinhard Pippan, Erich Schmid Institute, Leoben, for providing the HPT-disks
- Dr. Maciej Krystian, AIT - Austrian Institute of Technology, Wiener Neustadt, for providing the ECAP-rod

Bibliography

[1] B. Oberdorfer. "Atomic Free Volume in Bulk Nanocrystalline Metals studied by Dilatometry and Positron Annihilation". Dissertation. TU Graz, Institut für Materialphysik, 2012.

[2] Helmut Kronmüller and Manfred Fähnle. *Micromagnetism and the Microstructure of Ferromagnetic Solids*. Cambridge University Press, 2003.

[3] Alexander P. Zhilyaev and Terence G. Langdon. "Using high-pressure torsion for metal processing: Fundamentals and applications". *Progress in Materials Science* 53 (2008), pp. 893–979. DOI: 10.1016/j.pmatsci.2008.03.002.

[4] M. Cabibbo. "Grain refinement and hardness saturation in pure Nickel subjected to a sequence of ECAP and HPT". *La Metallurgia Italiana - n.9 2015 S.37-48* (2015).

[5] Ruslan Z. Valiev and Terence G. Langdon. "Principles of equal-channel angular pressing as a processing tool for grain refinement". *Progress in Materials Science* 51 (2006), pp. 881–981. DOI: 10.1016/j.pmatsci.2006.02.003.

[6] Roland Würschum. *Nanostructures and Nanotechnology*. 2015, p. 118.

[7] Gandhi Institute of Technology and Management. *Hard Ferromagnetic*. 2015. URL: http://www.gitam.edu/eresource/Engg_Phys/semester_2/magnetic/hard.htm.

[8] Mike Mcelfresh. *Fundamentals of magnetism and magnetic measurements featuring quantum design's magnetic property measurement system*. 1992.

[9] T. Holstein and H. Primakoff. "Field Dependence of the Intrinsic Domain Magnetization of a Ferromagnet". *Phys. Rev.* 58 (Dec. 1940), pp. 1098–1113. DOI: 10.1103/PhysRev.58.1098.

[10] Holger Kisker. "Magnetische Eigenschaften und Mikrostruktur von nanokristallinem Nickel". PhD thesis. Fakultät Physik der Universität Stuttgart, 1995.

[11] Helmut Kronmüller. "Mikromagnetische Berechnung der Magnetisierung in der Umgebung unmagnetischer Einschlüsse in Ferromagnetika". *Zeitschrift für Physik* 168 (1962), pp. 478–494. DOI: 10.1007/BF01378144.

[12] H. Kronmüller, N. Lenge, and H.-U. Habermeier. "Investigation of the approach to ferromagnetic saturation in sputtered amorphous Fe $_{80-x}$Ni $_{x}$B $_{20}$ films". *Physics Letters A* 101 (1984), pp. 439–442. DOI: 10.1016/0375-9601(84)90623-6.

[13] HP Chang, R Herz, and H Kronmüller. "High-field susceptibility of EuS single crystals". *Applied physics* 22 (1980), pp. 155–160.

[14] M Fähnle and H Kronmüller. "The influence of spatially random magnetostatic, magnetocrystalline, magnetostrictive and exchange fluctuations on the law of approach to ferromagnetic saturation of amorphous ferromagnets". *Journal of Magnetism and Magnetic Materials* 8 (1978), pp. 149–156.

[15] Arabi Sahar. "Magnetic Characterization of Electrodeposited Nanocrystalline Ni and Ni-Fe alloys". MA thesis. McMaster University for Materials Engineering in Hamilton, Ontario, 2011.

[16] C. Kittel. *Einführung in die Festkörperphysik*. Oldenbourg, 2006, p. 383. ISBN: 9783486577235.

[17] Terry C. Lowe and Ruslan Z. Valiev. *Investigations and applications of severe plastic deformation*. 2000, S.351.

[18] LOT-Oriel Group Europe. *MPMS XL - SQUID Technology*. LOT-Oriel Group Europe. 2015. URL: http://www.lot-oriel.com/site/site_down/qd_mpmsxl_deen04.pdf.

[19] J. Crangle and G. M. Goodman. "The Magnetization of Pure Iron and Nickel". *Proceedings of the Royal Society of London A: Mathematical, Physical and Engineering Sciences* 321 (1971), pp. 477–491. DOI: 10.1098/rspa.1971.0044.

[20] University of Cambridge. *Ferromagnetic Materials*. Ed. by Claide Hopwood and David Brook. 2016. URL: http://www.doitpoms.ac.uk/tlplib/ferromagnetic/printall.php%2024.2.2016.

[21] Jörg F. Löffler et al. "Random and exchange anisotropy in consolidated nanostructured Fe and Ni: Role of grain size and trace oxides on the magnetic properties". *Physical Review B* 57 (Feb. 1998), pp. 2915–2924. DOI: 10.1103/PhysRevB.57.2915.

[22] Jin Hanmin et al. “Inverted hysteresis loops: Experimental artifacts arising from inappropriate or asymmetric sample positioning and the misinterpretation of experimental data”. *Journal of Magnetism and Magnetic Materials* 308 (2007), pp. 56–60. DOI: 10.1016/j.jmmm.2006.05.002.

[23] Maclej Sawicki, Wiktor Stefanowicz, and Andreas Ney. “Sensitive SQUID magnetometry for studying nanomagnetism”. *Semiconductor science and technology* 26 (2011), pp. 1–16. DOI: 10.1088/0268-1242/26/6/064006.

[24] Kwiatkowska C.J. Mucha J.M. Szytula A. “Magnetic properties of nickel-vanadium alloys”. *J. Magn. Magn. Mater.* 42 (1984), pp. 53–58.